



IMPERIAL COLLEGE LONDON

DEPARTMENT OF AERONAUTICS

AERO60002 AEROSPACE VEHICLE DESIGN

---

## Preliminary and Detailed Design Report AVD Group 6

---

*Author:*

Brice Appenzeller (02358071)  
Ayooluwa Babalola (01715192)  
Benjamin Frisch (02356928)  
Edward Granthman (01848149)  
Antoine Pigamo (02355011)  
Fabienne Rosenblatt (02358188)

*Supervisor:*  
Dr. Daqing Yang

03/03/2023

## **Abstract**

This report outlines the preliminary design stage for an aircraft as described in the AVD brief. Based on the results from the conceptual design stage, a structural analysis was conducted for the fuselage, the wings and the selected tailplane in consideration of the different load cases and configurations described in the brief. The aircraft designed is a jet aircraft with aft-mounted engines with a capacity for 90 passengers. The structural analyses for each part of the aircraft contain systematic calculations and reasonable assumptions in order to determine the loads, select the materials and size the structural elements such as ribs, stringers and spars. Furthermore, the secondary structure design as well as the detailed design concept are discussed in this report, where the detailed design concept includes Finite Element Analysis.

# Contents

<b>1</b>	<b>Introduction</b>	<b>1</b>
1.1	V-n Diagram and Load Cases . . . . .	1
1.2	Similar Aircraft . . . . .	2
1.2.1	Fuselage . . . . .	2
1.2.2	Wing . . . . .	3
1.2.3	Empennage . . . . .	4
1.2.4	Composites . . . . .	4
1.2.5	Secondary Structures . . . . .	4
<b>2</b>	<b>Material selection</b>	<b>5</b>
2.1	Wings and vertical stabiliser . . . . .	5
2.1.1	Upper skin . . . . .	6
2.1.2	Lower skin . . . . .	6
2.1.3	Spar web . . . . .	6
2.1.4	Vertical Stabiliser . . . . .	6
2.2	Fuselage . . . . .	7
2.2.1	Upper skin . . . . .	7
2.2.2	Lower skin . . . . .	7
2.2.3	Other fuselage components . . . . .	8
2.3	Summary of Material Selection . . . . .	8
<b>3</b>	<b>Fuselage</b>	<b>9</b>
3.1	Load Modeling . . . . .	9
3.2	Load cases . . . . .	10
3.3	Skin thickness . . . . .	10
3.3.1	Cabin Pressure Load . . . . .	10
3.3.2	Shear Load . . . . .	11
3.3.3	Fuselage Stringer Design . . . . .	11
3.3.4	Skin Bay Buckling . . . . .	12
3.4	Fuselage Frames Design . . . . .	13
3.4.1	Light Frames Design . . . . .	13
3.4.2	Heavy Frames Design . . . . .	14
<b>4</b>	<b>Wing Design</b>	<b>16</b>

---

4.1	Loads . . . . .	16
4.2	Stringer-Panel Design . . . . .	17
4.3	Spar Design . . . . .	19
4.3.1	Spar Web Design . . . . .	19
4.3.2	Spar Cross-Section Design . . . . .	20
4.4	Rib Design . . . . .	21
4.5	Summary . . . . .	23
4.5.1	Wing Layout . . . . .	23
4.5.2	Weight of Components . . . . .	23
<b>5</b>	<b>Vertical Stabilizer Design</b>	<b>25</b>
5.1	Loads . . . . .	25
5.2	Spar Design . . . . .	26
5.2.1	Spar Web Design . . . . .	26
5.2.2	Spar Cross Section Design . . . . .	27
5.3	Stringer-Panel Design . . . . .	28
5.3.1	Sizing Methodology . . . . .	28
5.4	Rib Design . . . . .	29
5.5	Weight and Cost optimisation . . . . .	29
5.5.1	Results . . . . .	30
5.6	D-Cell Design . . . . .	31
5.7	Summary . . . . .	32
5.7.1	Vertical Tail Layout . . . . .	32
<b>6</b>	<b>Composite Horizontal Stabiliser Design</b>	<b>33</b>
6.1	Loads . . . . .	33
6.2	Composite Material Selection . . . . .	33
6.3	Wingbox and Laminate Design . . . . .	36
6.4	Buckling and Sandwich Structures . . . . .	37
6.5	Stringer, Rib and Spar Cap Design . . . . .	39
6.6	D Cell Design . . . . .	40
6.7	Horizontal Tail Layout . . . . .	41
<b>7</b>	<b>Secondary Structure Design</b>	<b>42</b>
7.1	Cutouts . . . . .	42
7.2	Joints and fittings . . . . .	43
7.3	Engine Mounts . . . . .	44
<b>8</b>	<b>Detailed Design Concept</b>	<b>45</b>
8.1	Mission . . . . .	45
8.2	Assumptions and Method . . . . .	45
8.3	Results of Iterations . . . . .	46
8.4	Topology Optimization . . . . .	47

---

8.5	Final Design . . . . .	48
8.5.1	Use of both methodologies . . . . .	48
8.5.2	Buckling analysis . . . . .	48
<b>9</b>	<b>Conclusion</b>	<b>49</b>
9.1	Mass Estimations . . . . .	49
9.2	Discussion of the fuselage . . . . .	49
9.3	Discussion of the wings . . . . .	49
9.4	Discussion of the empennage . . . . .	50
9.5	Overall Conclusion . . . . .	50
<b>A</b>	<b>Graphs Stringer Panel</b>	<b>2</b>
<b>B</b>	<b>Curved Plate</b>	<b>4</b>
<b>C</b>	<b>Shear Buckling Coefficient</b>	<b>6</b>
<b>D</b>	<b>Starting Plate Dimensions</b>	<b>7</b>
<b>E</b>	<b>Topology Optimisation Designs</b>	<b>8</b>
<b>F</b>	<b>Final Design</b>	<b>11</b>
<b>G</b>	<b>Final Design Buckling Analysis</b>	<b>13</b>
<b>H</b>	<b>Final Design Dimensions</b>	<b>15</b>
<b>I</b>	<b>Fuselage</b>	<b>17</b>
<b>J</b>	<b>Engine Mounts+ Sizing Forces</b>	<b>23</b>
<b>K</b>	<b>Composite K Graphs</b>	<b>25</b>
<b>L</b>	<b>Secondary Structures K Graphs</b>	<b>26</b>
<b>M</b>	<b>Secondary Structures</b>	<b>28</b>
<b>N</b>	<b>Skin Layup</b>	<b>30</b>
<b>O</b>	<b>Spar Ply Numbers along span</b>	<b>31</b>

# List of Figures

1.1	V-n Diagram . . . . .	1
1.2	Spar configurations . . . . .	3
2.1	$M_{compression}$ vs $M_{stiffness}$ . . . . .	6
2.2	$M_{tension}$ vs $M_{fatigue}$ . . . . .	6
2.3	$M_{torsion}$ vs $M_{fatigue}$ . . . . .	7
2.4	$M_{compression}$ vs $M_{fatigue}$ . . . . .	8
2.5	$M_{yield}$ vs $M_{stiffness}$ . . . . .	8
3.1	Inertia load distribution along the fuselage. Load factor of 1. . . . .	9
3.2	Shear force distribution along the fuselage. Load factor of 3.75 at MTOW. . . . .	10
3.3	Bending moment distribution along the fuselage. Load factor of 3.75 at MTOW. . . . .	10
3.4	A Graph Showing the Scaled Shear Flow Around Fuselage Skin at Max Shear = 687751.2N . . . . .	11
3.5	A Graph Showing the variation of required skin thickness with number of stringers . . . . .	12
3.6	CAD Model of Fuselage Stringers . . . . .	13
3.7	Detailed View of Stringer Dimensions . . . . .	13
3.8	Evolution of optimal height with required thickness. . . . .	14
3.9	Evolution of optimal width with required thickness. . . . .	14
3.10	Evolution of minimal area with required thickness. . . . .	14
3.11	Loads distribution on wings heavy frames. . . . .	15
3.12	Loads distribution on T-Tail heavy frames. . . . .	15
3.13	Loads distribution on engines heavy frames. . . . .	15
4.1	Loads, shear forces, bending moments and torques experienced by wing along span. . . . .	18
4.2	Skin thickness along the wing . . . . .	19
4.3	Front and Rear Spar Web Thickness . . . . .	20
4.4	Flange Thickness of front spar . . . . .	21
4.5	Flange Breath of front spar . . . . .	21
4.6	Flange Thickness of rear spar . . . . .	21
4.7	Flange Breath of rear spar . . . . .	21
4.8	Ribs Thickness . . . . .	22
4.9	Wing Layout . . . . .	23
5.1	Load case 2 assumed flight condition and moment balance . . . . .	25

5.2	Loads, shear forces, bending moments and torques experienced by Vertical tail along span. . . . .	26
5.3	Ideal front and rear spar thickness . . . . .	27
5.4	Real front and rear spar thickness . . . . .	27
5.5	Flange Thickness of front spar . . . . .	27
5.6	Flange Breath of front spar . . . . .	27
5.7	Flange Thickness of rear spar . . . . .	28
5.8	Flange Breath of rear spar . . . . .	28
5.9	Skin thickness distribution . . . . .	29
5.10	Rib thickness distribution . . . . .	29
5.11	Weight Optimisation . . . . .	30
5.12	Cost Optimisation . . . . .	30
5.13	D-cell thickness vs Number of pseudo-ribs . . . . .	31
5.14	Weight optimisation . . . . .	32
5.15	Cost optimisation . . . . .	32
5.16	Vertical Tail Layout . . . . .	32
6.1	Lift Distribution from Asymmetric Pressure in OEI case . . . . .	34
6.2	Loads, shear forces, bending moments and torques experienced by Horizontal tail. . . . .	34
6.3	One symmetric half of front spar showing interleaved dropped plies for the original and buckling layup. . . . .	37
6.4	Minimum mass/thickness basic layup . . . . .	39
6.5	Graph of the thickness of all ribs along the semi-span. . . . .	40
6.6	Composite spar cap diagram [28] . . . . .	40
6.7	HT D-Cell Mass Optimisation . . . . .	41
6.8	Horizontal Tail Layout . . . . .	41
7.1	Graph showing change in axial load of stringers after one is cut . . . . .	42
8.1	Evolution of geometry : V1, V2, V3, V7 . . . . .	46
8.2	V7 : Stress and Strain   Limit Load . . . . .	46
8.3	V7 : Stress and Strain   Ultimate Load . . . . .	47
8.4	Geometry for V>15% and V>20% . . . . .	47
8.5	Final Design . . . . .	48
A.1	Farrar Efficiency . . . . .	2
A.2	Initial Buckling Stress of flat panels with Z Section stringers . . . . .	3
B.1	Buckling stress Coefficient for curved plates in shear . . . . .	4
B.2	Buckling stress Coefficient for curved plates in shear . . . . .	5
C.1	Shear Buckling Coefficeint . . . . .	6
D.1	Starting plate dimensions . . . . .	7
E.1	Part Build from previous geometries for V>15% and V>20% . . . . .	8
E.2	V>20% : Stress (UL case) and Strain (LL case) . . . . .	9

E.3	V>15% : Stress (UL case) and Strain (LL case)	10
F.1	Final Design : Stress and Strain   Limit Load	11
F.2	Final Design : Stress and Strain   Ultimate Load	12
G.1	Buckling Mode 1 and 2	13
G.2	Buckling Mode 3 and 4	14
G.3	Buckling Mode 5	14
H.1	Final Design External Dimensions	15
H.2	Final Design Internal Angles	16
H.3	Final Design Internal Lengths	16
I.1	Drawing of all heavy frames location.	17
I.2	Evolution of optimal height with required thickness for engines heavy frames.	17
I.3	Evolution of optimal width with required thickness for engines heavy frames.	18
I.4	Evolution of minimal area with required thickness for engines heavy frames.	19
I.5	Evolution of minimal area with required thickness for wings heavy frames.	19
I.6	Evolution of minimal area with required thickness for wings heavy frames.	20
I.7	Evolution of minimal area with required thickness for wings heavy frames.	20
I.8	Evolution of minimal area with required thickness for tail heavy frames.	21
I.9	Evolution of minimal area with required thickness for tail heavy frames.	21
I.10	Evolution of minimal area with required thickness for tail heavy frames.	22
J.1	Diagram of the planned engine mounting for a fuselage mounted engine. [32]	23
J.2	Engine mount sizing forces during regular operation	24
J.3	Engine mount sizing forces during emergency landing	24
K.1	Composite K Graph	25
K.2	Composite K Graph	25
L.1	Structure K graph	26
L.2	Structure K Graph	27
M.1	Diagram showing shear flow in panels surrounding supported cutout	28
M.2	Dimensions of one window panel and its required doubler	28
M.3	Diagram showing most common aeroplane joints and fittings alternatives[14]	29
N.1	Skin Layup	30
O.1	How number of plies changes along spar semi span	31

# List of Tables

1.1	Similar Aircraft . . . . .	2
1.2	Mean ribs spacing for similar aircraft . . . . .	3
2.1	Material Indices for the fuselage . . . . .	7
2.2	Summary of the material selection . . . . .	8
3.1	Summary of the position of important components. . . . .	9
3.2	Summary of maximum shear force, bending moment and torque in all cases. . . . .	10
3.3	Summary of required thickness. . . . .	11
3.4	Summary of fuselage stringers parameters. . . . .	13
3.5	Summary of loads applied on heavy frames. . . . .	15
3.6	Summary of heavy frames dimensions. . . . .	15
4.1	Geometry of the stringer-skin of the wing . . . . .	19
4.2	Front and Rear Spar Web Thickness . . . . .	20
4.3	Spar Cap design for the wing . . . . .	21
4.4	Summary of rib design . . . . .	22
4.5	Weight summary of each component of the wing . . . . .	24
5.1	wing boxes geometry for the vertical stabiliser . . . . .	27
5.2	Spar Cap design for the Vertical Tail . . . . .	27
5.3	Summary of the guidelines . . . . .	28
5.4	Geometry of the stringer-skin of the vertical stabiliser . . . . .	30
5.5	Summary of rib design . . . . .	31
5.6	Summary of D-cell design . . . . .	32
6.1	Normalised merit indices . . . . .	35
6.2	Ply selection . . . . .	35
6.3	Ply properties . . . . .	36
6.4	Number of skin plies in each orientation . . . . .	36
7.1	Table of new skin thicknesses surrounding door cutout. . . . .	43
8.1	Properties of Aluminium 6082-T6 [33] . . . . .	45
8.2	Results of iterations . . . . .	46

8.3	Results of iterations . . . . .	47
8.4	Final Design characteristics . . . . .	48
8.5	Summary of buckling modes . . . . .	48
8.6	Summary of each methodology best results . . . . .	48
9.1	Mass Table . . . . .	49
I.1	A Table Showing the initial Stringer and Skin Bending Geometries . . . . .	17

## List of Symbols

$A_s$	Stringer Cross Sectional Area
$a$	Rib/Frame Spacing
$b$	Span/Stringer Spacing/Spar Height
BM	Bending Moment
$c$	Box width
$C_l$	Lift Coefficient
$C_m$	Moment Coefficient
$D$	Diameter
$D_x$	Moment of Area for a thin walled section
$E$	Young's Modulus
$F$	Farrar Efficiency/Crush Load
$I$	Second Moment Of Inertia
$k$	Various Constants
$K_s$	Shear Buckling Coefficient
$L$	Lift/Rib Spacing
$L_e$	Effective Stringer Buckling Length
$M_0$	Pitching Moment
$M_{ult}$	Bending Moment applied to fuselage
$M_Q$	Moment generated by a Radial Force
$M_P$	Moment generated by a Tangential Force
$M_T$	Moment generated by an other Moment
MTOW	Maximum Take-Off Weight
MZFW	maximum Zero fuel weight
$n$	Number of Plies
$N$	Load per unit width
$N_F$	Scatter Factor
$N_Q$	Axial Force generated by a Radial Force
$N_P$	Axial Force generated by a Tangential Force
$N_T$	Axial Force generated by a Moment
OEI	One Engine Inoperative
$P$	Pressure
$P$	Tangential Shear Force
$P_{crit}$	Critical Buckling Load
$p$	Adjusted Stringer Pitch
$Q$	Radial Shear Force
$q$	Dynamic Pressure/ Shear Flow
$q_r$	Shear flow around fuselage
$R_c, R_s$	Compressive and Shear stress ratios
$R_{cs}$	Combined Compressive and Shear stress ratios
$R$	Reaction Force
$S$	Area
$S_Q$	Shear Force generated by a Radial Force
$S_P$	Shear Force generated by a Tangential Force
$S_T$	Shear Force generated by a Moment
$T$	Thrust/Moment/Torque
$t$	Thickness
$t_1$	Cylinder Skin Thickness
$t_2$	Sphere Skin Thickness
$t_s$	Stringer Thickness
$V$	Shear
$V_a$	Manoeuvring Speed
$V_d$	Dive Speed
$w$	Width
$W$	Weight
$\gamma$	Taper Ratio
$\phi$	Angle around fuselage
$\sigma_H$	Stress/Hoop Stress
$\tau$	Torque
$\nu$	Poisson Ratio

# Chapter 1

## Introduction

### 1.1 V-n Diagram and Load Cases

This report deals with the Preliminary and Detailed Design of the aircraft previously detailed in the Conceptual Design report. During all the phases of its cycle the aircraft will undergo different stresses. All the efforts are concentrated from the next envelope depending on the speed. Two loads come to limit this envelope.

- **Limit Load :**  $n = +2.5 / -1$

This limit represents the largest load the aircraft is expected to encounter.

- **Ultimate Load :**  $n = 1.5 * (+2.5 / -1) = +3.75 / -1.5$

This limit represents the previous limit time a security factor. The design of each components must take into account this security factor. It is therefore a design load.

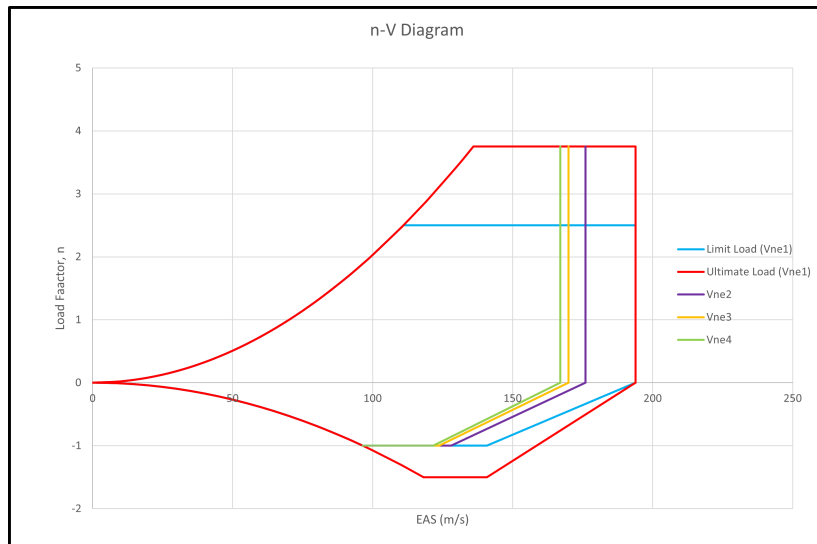


Figure 1.1: V-n Diagram

The right speed limit refers to the dive speed. This is the speed the aircraft cannot exceed. This speed depends on the cruising MAC. [1] But the mission profile of the plane specifies that there are four different cruises. This is why there are four different dive speed limit. The most restrictive is the highest (cruise 1) so it was she who was chosen to make the V-n diagram.

Throughout this study, different load cases will be taken into account.

- **Load case 1 :** Symmetric flight at the ultimate load factor evaluated at  $V_A$  and  $V_D$ .

- **Load case 2 :** One Engine Inoperative.
- **Load case 3 :** Landing with front-nose case. The full aircraft is supported by the main undercarriage only.

## 1.2 Similar Aircraft

With regards to composites, similar aircraft having been incorporating more and more composites. This is due to their lighter weight, as well as better fatigue and corrosive properties among other benefits. Composites are commonly used on similar aircraft. Specifically carbon and glass fibre composites are widely used on aircraft. Sandwich structures are commonly used either in the wing skin or spar. For airliners, the most common use is honey comb structures in the skin [2]. The most technologically advanced similar aircraft such as the Boeing 787 incorporate composites in the fuselage, wings, empennage, nacelles and many other places. This is however not appropriate for this design of a regional aircraft as the high costs likely out weight the fuel savings for a small regional airliner. It is also beyond the scope of this preliminary report to design all such components. Therefore it is decided to design one component, the horizontal tail plane out of composites.

	<b>Similar aircraft</b>	
CRJ1000	ERJ145XR	B717

**Table 1.1:** Similar Aircraft

### 1.2.1 Fuselage

#### Skin

Concerning the fuselage skin, popular skin materials in the aerospace industry are materials with high fracture toughness, good fatigue life and high tensile strength. One example is the aluminium alloy 2024-T3 [3].

The thickness of the skin is usually between 1 and 2 mm. Such a small thickness together with a structure made up of stringers and light frames makes it possible to obtain a lighter structure than would be obtained with a greater thickness [4].

#### Stringers

The stringers have been present since the earliest aircraft sometime longerons are used instead in cases where larger loads are carried. Stringers are attached to the skin and span the length of the fuselage. Stringers carry the bending load on the aircraft in addition they act as stiffeners increasing the skin resistance to buckling. Z,I and hat stiffeners have been used as stringer cross sections as seen in Niu [5] with similar passenger aircraft having between 50-110 stringers.

#### Light Frames

The light frames are present all along the fuselage and serve mainly to prevent the skin of the aircraft from buckling. All commercial aircraft tend to have 0.5m spacing between each light frame. [6]

#### Heavy Frames

Heavy frames address a different issue. They are there to support heavier loads applied to specific locations in the fuselage. Typically, they are placed near the wings, engines and tail. Given their role, they are larger and much heavier than light frames. [6]

### 1.2.2 Wing

#### Stringer-Skin Panel

There are many configurations for the stringer-skin panel. The parameters that often change are the number of stringers and their size. The size of the skin is a direct consequence of these parameters. From [Airframe structural design, Niu], information has been found about successful stringer designs. For example, it is explained that stringers should have a height of between 60 and 70mm. For this reason, the height of the stringers was later chosen to be 60mm.

Most of the design have a Z shape for the stringer because in practice it is more robust. [5]

About the number of stringer and the stringer spacing, the average stringer spacing is between 100 and 125mm [7]. For the project, the stringer spacing will be higher (around 300mm) because there was a need to get a low  $\sigma_0$  to not yield.

#### Spars

The number of spars in all similar aircraft is always two for the wings and tail. This will also be the case for the project. Moreover, figure 1.2 illustrates various constructions of spar beams, which can be classified into two types: truss and shear web. For commercial aircraft subjected to relatively mild loads, the industry standard is to use a built-up web design for the spar. And it is also the choice made for this project.

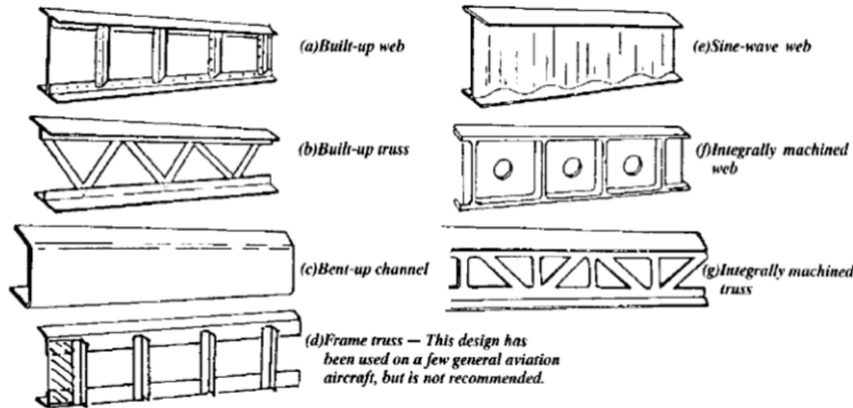


Figure 1.2: Spar configurations

#### Ribs

For ribs the two important parameters are the arrangement of the ribs and their spacing. The following table shows the average rib spacing for similar aircraft.[8][9].

CRJ1000	ERJ145XR	B717
0.43 m	0.40 m	/

Table 1.2: Mean ribs spacing for similar aircraft

This value will therefore be used as a reference to check that the rib spacing found in the study is of the right order of magnitude.

Then the arrangement of the ribs must be chosen. The ribs can either be perpendicular to the leading edge or parallel to the fuselage axis. Although having ribs parallel to the fuselage axis results in an aerodynamically precise shape, the structural downsides of this configuration are more significant. Therefore, aircraft manufacturers generally design the ribs to be parallel to the fuselage near the root and then move to perpendicular to the leading edge ribs near the tip of the wing (CRJ1000 [9]).

### 1.2.3 Empennage

Constructions employed in the stabiliser and the fixed control surfaces are similar to the methods of wing construction mentioned earlier.

Similar regional airliners have often skin-stringer types of construction with the use of Aluminium 7075, 2024 and 2014 for the skin and the stringers. Usually, the vertical stabiliser of a T-tail has a shorter span than conventional tail, however this type of configuration requires high structural stiffness. Consequently, skin-stringers panels are suitable for this requirement and this type of construction is adopted [10]. For the same reason as 1.2.2, Z-stringers are used for the vertical stabiliser.

Other structural assumptions follows the justification of section 1.2.2 and the guidelines of chapter 5.

Empennage structures also tend to have more ribs with the A320 for example having 24 ribs in the semi span of its horizontal tail plane over a similar span to this design's [11].

### 1.2.4 Composites

Composites components are becoming more and more common in similar commercial aircraft. Aircraft such as the Boeing 787 Dreamliner or the Airbus A350 have parts of the fuselage, wings and empennage made of composites. The most common types of laminate composite materials used in commercial aircraft are carbon and glass fibre [12]. Sandwich structures are also often used in wing skins to improve buckling performance. For commercial aircraft, the most common sandwich cores are aluminium and aramid (NOMEX) honey comb structures as well as some technical foams [13]. Sandwich structures are often used in spars of general aviation applications but not in commercial aircraft. Some aircraft with either composite wings or empennage have the leading edge made of metal instead of composites to protect them against impacts and erosion.

### 1.2.5 Secondary Structures

A study of similar aircraft shows that the most common cutouts are the doors, windows and holes. Among the doors especially the main doors, emergency doors and cargo doors were considered. Inspection holes and lightening holes in the spars and ribs in both the wings and the empennage were examined [14].

From similar commercial aircraft the most common types of wing root joints are splice plates, tension bolts and lugs. Splice plates are usually used for commercial aircraft while tension bolts and lug wing roots are usually used for thin wing aircraft such as fighters. Bolts, rivets and adhesive bonding are the most common forms of aircraft joiners used on these aircraft.

# Chapter 2

## Material selection

This chapter of the report outlines the methodology for the material selection of the wings, the fuselage and the empennage.

Aluminium alloys are widely used on aircraft structures, especially on the fuselage and wing because they offer a good weight reduction, low cost and effective mechanical properties [3]. Furthermore, they are nowadays easy to manufacture and have a significant corrosion resistance which is extremely useful in the geographical context of New Zealand because the country provides challenges for building material durability with its long coastline and geothermal areas [15].

As a matter of fact, aluminium alloys will be adopted for the structure of the wings, the fuselage and the vertical stabiliser.

The selection is made based on a list of 11 aluminium alloys frequently used in the aerospace industry [5].

Moreover, materials were picked by plotting Ashby charts on the software Ansys Granta EduPack and its large database for aerospace applications [16].

### 2.1 Wings and vertical stabiliser

The choice of materials for the wing components focuses on upper and lower surfaces and on the spar web. The upper skin of the wing is under cyclic compression and requires high stiffness. The lower skin is under cyclic tension loading and is particularly prone to fatigue through application and relaxation of tension stresses [10]. Finally, the spars need to be sized based on the tensile and compressive strength to minimise  $I_{xx}$  and thus allow weight reduction (see 4.3) .

Consequently, the involved mechanical properties for the upper surface are **high stiffness E** and **compressive strength  $\sigma_c$** , while the lower surface requires high **fracture toughness  $K_{IC}$**  and **tensile strength  $\sigma_t$** . Finally, the spar web design requires a **high compressive strength  $\sigma_c$**  and **tensile strength  $\sigma_t$**  .

Furthermore, the material selected should be lightweight (low  $\rho$ ) and cost-effective (low cost  $c$ ). To meet these requirements, an analysis based on the maximisation of the following material indices is led for the upper and lower skin and for the spars [6]:

$$M_{compression} = \frac{\sigma_c^{\frac{2}{3}}}{\rho c} \quad (2.1)$$

$$M_{stiffness} = \frac{E^{\frac{1}{2}}}{\rho c} \quad (2.2)$$

$$M_{tension} = \frac{\sigma_t^{\frac{2}{3}}}{\rho c} \quad (2.3)$$

$$M_{fatigue} = \frac{K_{IC}}{\rho c} \quad (2.4)$$

$$M_{shear} = \frac{\sigma_s^{\frac{2}{3}}}{\rho c} \quad (2.5)$$

### 2.1.1 Upper skin

The selection for the upper skin of the wing is thus made by plotting  $M_{compression}$  vs  $M_{stiffness}$  and looking for the material in the top right corner of the chart. The Aluminium 2014-T6 is thus selected for the upper wing:

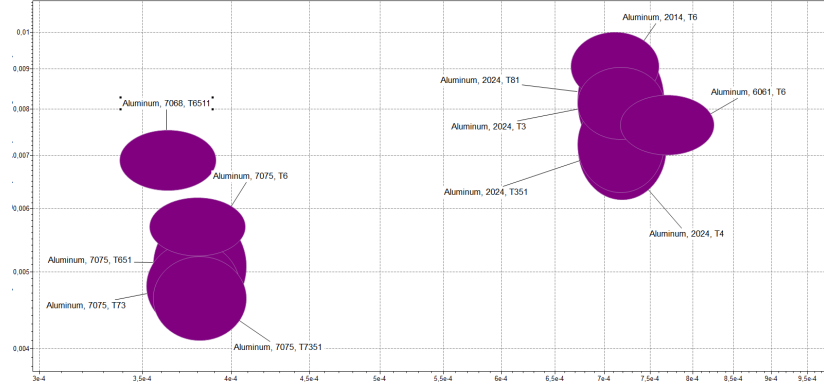


**Figure 2.1:**  $M_{compression}$  vs  $M_{stiffness}$

### 2.1.2 Lower skin

The selection for the lower skin of the wing is made by plotting  $M_{tension}$  vs  $M_{fatigue}$ . Because the Aluminium 2024-T3 and the Aluminium 2024-T81 have both adequate properties on the chart, a further comparison is made on MatWeb. Since the Aluminium 2024-T81 has a much higher tensile strength than the Aluminium 2024-T3 [17], it is chosen for the design of the lower skin:



**Figure 2.2:**  $M_{tension}$  vs  $M_{fatigue}$

### 2.1.3 Spar web

The selection for the spar material is made by plotting  $M_{compression}$  vs  $M_{tension}$ . The same method results in the selection of the Aluminium 2014-T6 based on its values of  $\sigma_c$  and  $\sigma_t$  [17].

### 2.1.4 Vertical Stabiliser

Since the requirements for the vertical stabiliser are similar to the wings, it has been decided to choose the same materials for the vertical stabiliser.

## 2.2 Fuselage

Concerning the fuselage, other considerations such as torsion, yield have to be considered on top of the previous section mechanical properties. Consequently two more material indices are defined:

$$M_{torsion} = \frac{G}{\rho c} \quad (2.6)$$

$$M_{yield} = \frac{\sigma_y^{\frac{2}{3}}}{\rho c} \quad (2.7)$$

The different material indices to consider for each component of the fuselage are the following [6] :

Fuselage Components	Indices to maximize
Upper skin	$M_{tension}$ $M_{fatigue}$ $M_{torsion}$
Lower skin	$M_{compression}$ $M_{fatigue}$ $M_{torsion}$
Stringer	$M_{stiffness}$ $M_{yield}$
Light frames	$M_{stiffness}$ $M_{yield}$
Heavy frames	$M_{stiffness}$ $M_{yield}$

Table 2.1: Material Indices for the fuselage

### 2.2.1 Upper skin

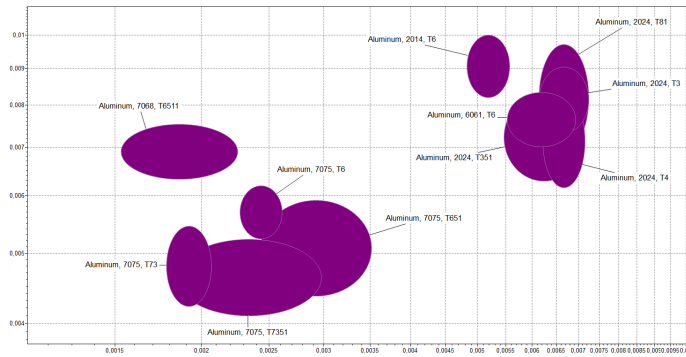
The following chart of  $M_{torsion}$  vs  $M_{fatigue}$  and checks on MatWeb states that the Aluminium 2024-T81 and the Aluminium 2024 T3 are the most interesting and have both the same value for  $M_{torsion}$  and  $M_{fatigue}$ . Ultimately, the choice came down to  $M_{tension}$  vs  $M_{fatigue}$ , and thus the Aluminium 2024 T81 is chosen for the same reason as 2.1.2:



Figure 2.3:  $M_{torsion}$  vs  $M_{fatigue}$

### 2.2.2 Lower skin

The plot of  $M_{compression}$  vs  $M_{fatigue}$  shows again that the Aluminium 2024-T81 and the Aluminium 2024-T3 are the most appropriate materials for the lower skin of the fuselage. A further analysis on MatWeb indicates that the  $M_{compression}$  of the Aluminium 2024-T81 is slightly greater than the  $M_{compression}$  of the Aluminium 2024-T3. Moreover, the 2024-T81 is slightly susceptible to corrosion whereas the 2024-T3 is highly susceptible to corrosion [16]. As a matter of fact the Aluminium 2024-T81 is selected:

Figure 2.4:  $M_{compression}$  vs  $M_{fatigue}$ 

### 2.2.3 Other fuselage components

For fuselage components such as stringer, light frames and heavy frames, the selection is made by plotting  $M_{yield}$  vs  $M_{stiffness}$ . As the chart highlights, the Aluminium 2024-T81 and the Aluminium 2014-T6 are well suited for these components. It is then decided to choose the Aluminium 2024-T81 because of the previous decisions and consistency over the fuselage structure:

Figure 2.5:  $M_{yield}$  vs  $M_{stiffness}$ 

## 2.3 Summary of Material Selection

The materials selected for the aircraft structure and some of their properties are summarised in the following table:

Location	Material	$\rho$ ( $kg.m^{-3}$ )	E (GPa)	Price (£/kg)
Upper Wing and VT skin	Alu 2014-T6	2800	73.1	2
Lower Wing and VT skin	Alu 2024-T81	2780	72.4	2
Wing and VT spar web	Alu 2014-T6	2800	73.1	2
Fuselage	Alu 2024-T81	2780	72.4	2

Table 2.2: Summary of the material selection

# Chapter 3

## Fuselage

The objective of this part is to size the fuselage skin, stringers, light frames and heavy frames. This involves determining their number, location and dimensions. These are constrained by the loads applied to the fuselage.

### 3.1 Load Modeling

The weights determined in the conceptual design report were distributed along the fuselage. This was done in a way that the centre of gravity for each component is coherent with the Weight and Balance table [18].

An exception was made for the wings since the centre of gravity of the wings along the fuselage axis is not directly associated with the frame at this position because the wings are swept. Therefore, the wings weight was loaded on the frames where the front and rear spar of the wings are connected. The same methodolgy was used for components located on the wings such as main landing gear, flight controls or hydraulic system. The final inertia load distribution is presented in the form of a graph (see Figure 3.1). The location of important positions on the fuselage are summarised in Table 3.1 below.

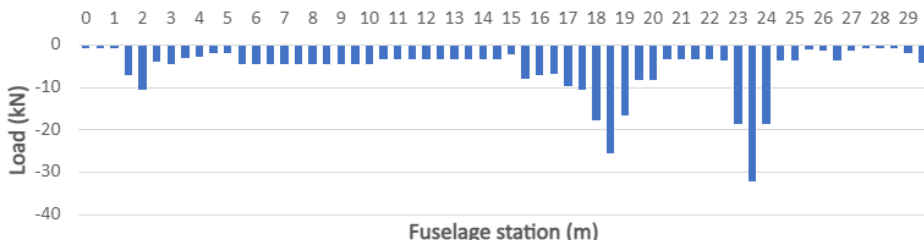


Figure 3.1: Inertia load distribution along the fuselage. Load factor of 1.

Component	x-coordinate [m]
Engines	23.45
Main Landing Gear	18.44
Front Spar	15.5
Rear Spar	18
Horizontal Tailplane	29.99
Vertical Tailplane	28.37

Table 3.1: Summary of the position of important components.

## 3.2 Load cases

All load cases have been determined in the MTOW case as this is the most constraining in terms of shear, bending moment and torque. For each load case, a trim load is applied either on the horizontal or on the vertical tailplane to ensure the balance of the aircraft (i.e. zero bending moment at the extremities). For the symmetric flight and the OEI condition, a load factor of 3.75 has been chosen accordingly to the n-V diagram determined Section 1.1. In the landing case, it was assumed that the aircraft has just touched down and therefore produces zero lift and that all the weight is supported by the main landing gears. It is important to notice that the OEI case is the only asymmetric load so it is the only which produces a torque to the fuselage. Shear force and bending moment distributions can be found in Figures 3.2 and 3.3. For the sake of clarity, only the case of symmetrical flight is presented as it is the most constraining. A summary of maximum shear force, bending moment and torque independently of the load case is presented Table 3.2. The fuselage torque only appears in the asymmetric case during OEI, it is equal to the lift produced by the empennage multiplied by the distance between the empennage and the fuselage axis.

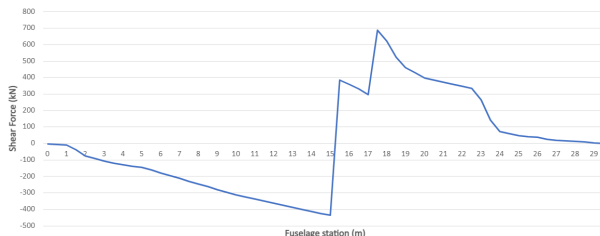


**Figure 3.2:** Shear force distribution along the fuselage.  
Load factor of 3.75 at MTOW.

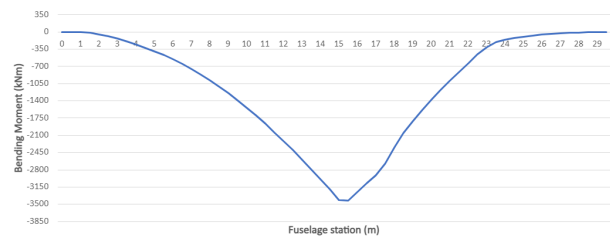


**Figure 3.3:** Bending moment distribution along the fuselage.  
Load factor of 3.75 at MTOW.

Maximum Shear Force (kN)	Maximum Bending Moment (kNm)	Maximum Torque (kNm)
687	3,431	55

**Table 3.2:** Summary of maximum shear force, bending moment and torque in all cases.

## 3.3 Skin thickness

### 3.3.1 Cabin Pressure Load

Because of the pressure difference between the outside and inside of the aircraft, the aircraft is subject to a pressure load. The load is maximum when the pressure difference is maximum, i.e. when the aircraft is at its ceiling altitude which was determined to be 36,200 ft [18]. At this altitude, the outside pressure is 0.22 bar against 0.7 bar inside which corresponds to the altitude at 8,000 ft in accordance with the FAR25 [19]. To determine the required skin thickness, the problem is simplified by considering the aircraft as a cylinder with two spheres at its extremities. The required skin thickness  $t_1$  for the cylinder can then be calculated by using the following equation:

$$\frac{\sigma_H}{P} = \frac{D}{2t} \quad (3.1)$$

Where  $\sigma_H$  is the hoop stress which is 450 MPa for the material used (see Section 2.2) and  $D$  is the diameter of the fuselage. This gives a value of 0.173 mm for  $t_1$ . The required thickness for the spheres  $t_2$  can be easily done using the matched strains dome thickness ratio described by this equation:

$$\frac{t_1}{t_2} = \frac{2 - \nu}{1 - \nu} \quad (3.2)$$

Where  $\nu$  is the poisson ratio which is equals to  $\frac{1}{3}$  for the material chosen. A summary of the required thickness found is presented below: As the required thickness values are extremely low, the subsequent structural load analysis of shear, bending and buckling will determine the final skin thickness.

$t_1$ [mm]	$t_2$ [mm]
0.173	0.069

**Table 3.3:** Summary of required thickness.

### 3.3.2 Shear Load

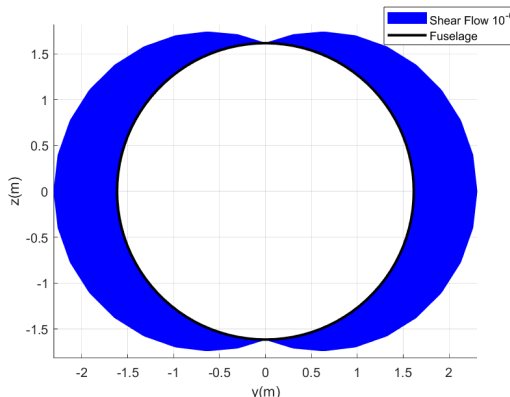
The shear load and torque the fuselage experiences along and around its cross section is carried by the fuselage skin. This requires that the aircraft have a certain minimum skin thickness in order to carry the shear and torque load.

The constraining shear load was the radial shear on the fuselage seen in table 3.3 and was therefore used to determine the skin thickness. The load on the skin can be calculated as a shear flow which is the shear load per unit distance at each point in the skin. The equation 3.3 for the shear flow around a thin walled section becomes equation 3.4[20] when applied to a thin fuselage. The shear flow around the fuselage ring could then be determined and is shown in figure ??

$$q = \frac{Q}{I_x} D_x \quad (3.3)$$

$$q_r = \frac{Q \sin(\Phi - \alpha)}{\pi r} \quad (3.4)$$

The resulting shear flow is shown in figure 3.4

**Figure 3.4:** A Graph Showing the Scaled Shear Flow Around Fuselage Skin at Max Shear = 687751.2N

The thickness can be determined by dividing the shear flow by the yield of the material. This produces the minimum thickness needed to produce this stress at the most constraining case. A minimum skin thickness of 0.459mm was determined and rounded up to the final value of 0.5mm. This value was thicker than the required skin thickness to sustain the pressure load and was the skin thickness used in the following analyses.

### 3.3.3 Fuselage Stringer Design

The fuselage stringers are the main structural components sustaining the bending load along the aircraft body. The stringers were sized using the maximum bending moment of  $3432.10^3$ Nm. The fuselage was idealised as a beam, the stringers acting as booms with point areas. An initial number of stringers had to be chosen, using examples in Bruhn [21] as a reference 57 stringers were chosen. A section of the skin contributes to the bending stiffness taken to be a length 15 times the skin thickness across each stringer. As the stringers and skin have been idealised as point areas the second moment of area calculation becomes equation 3.5 [20]

$$I_y = \sum A z^2 \quad (3.5)$$

$$\sigma = \frac{M}{I_y} z \quad (3.6)$$

Equation 3.6 is the typical bending stress equation. By replacing stress with the compressive yield stress of the material in equation 3.6. The  $I_y$  value of the stringers and skin can be calculated and hence the stringer area can be determined.

The calculated values are presented in table I.1

### 3.3.4 Skin Bay Buckling

Once the initial area of the stringers required to sustain the bending load had been calculated, the buckling stress of the bay area between the stringers was analysed. As seen in Niu [StressniuNiu] buckling load is often a more constraining failure mode than the material yield or failure stress. As the skin will experience a direct compression due to bending but also a significant shear force a combined loading case was analysed.

$$\sigma_{crit} = KE\left(\frac{t}{b}\right)^2 \quad (3.7)$$

$$\sigma_{crit} = \frac{k_c \pi^2 E}{12(1 - \nu^2)} \left(\frac{t}{b}\right)^2 \quad (3.8)$$

Equation 3.7 shows the typical equation for buckling as seen in the ESDU [22] for a curved plate subjected to shear. The more complex equation 3.8 from Niu computes the critical buckling load for a curved plate under compression where  $K$  and  $k_c$  are buckling stress coefficients that can be obtained from graphs in Niu and the ESDU.

The buckling analysis separates the skin into panels lengths  $a$  and  $p$ .  $a$  is the axial length equal to the frame spacing,  $p$  is the curved length of the panel equal to the stringer pitch adjusted by minus  $15t$  to account for the stiffening effect of the stringers. The individual buckling loads in shear and compression are calculated and used to find the stress ratios  $R_c$  and  $R_s$  the ratio between the stress acting on the panel over the critical stress  $\frac{\sigma_{actual}}{\sigma_{crit}}$ . These ratios are then combined by adding  $R_s^2$  and  $R_c$  to obtain  $R_{cs}$  which must be less than one.

As the critical buckling stress and subsequently  $R_{cs}$  depends on stringer pitch and skin thickness these values were adjusted in a Matlab script producing figure 3.5 showing the variation of skin thickness to stringer pitch that produce  $R_{cs} < 1$  roughly equal to 0.99. A stringer pitch of 87 was selected as it produced a suitably thin skin while the manufacturing requirements and cost are still reasonable. This number of stringers mean the stringer pitch equals 0.117m and requires a skin thickness of 0.0031m for  $R_{cs} < 1$  where the frame spacing is 0.5m. The buckling of the

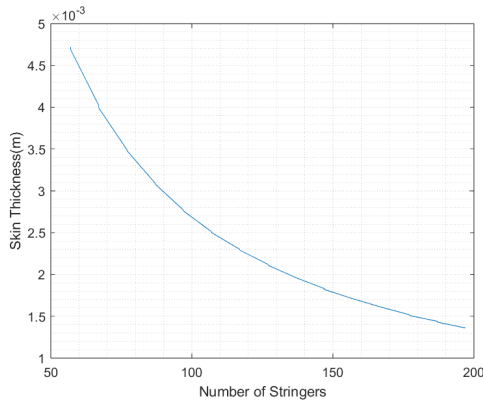


Figure 3.5: A Graph Showing the variation of required skin thickness with number of stringers

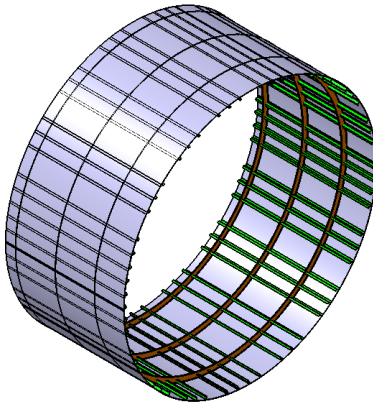
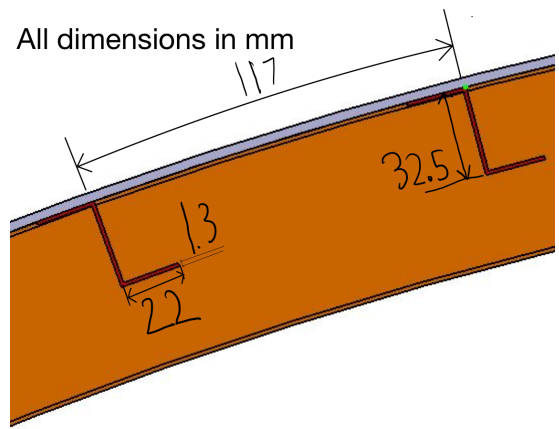
individual stringers could then be analysed to complete the sizing of the stringer - skin panels. The stringer failure mode is assumed to be Euler buckling for which the critical load and stress can be calculated with equations 3.9 and 3.10.

$$P_{crit} = \frac{\pi^2 EI}{L_e} \quad (3.9)$$

$$\sigma_{crit} = \frac{P_{crit}}{A_s} \quad (3.10)$$

With equations 3.9 and 3.10 the dimensions of the stringers were determined. The z stringers had a limiting dimension of half the fuselage light frame height which had been determined by this time, seen in section 3.4 of 32.5mm. Using a Matlab script the parameters flange length  $F_L$  and stringer thickness  $t_s$  were varied between 10mm to 25 mm and 1mm - 5mm which were reasonable values from examples in Bruhn. The stringer geometries that had a critical failure equal to the critical compressive buckling stress of the bay were then selected. The selection of the final geometry was a balance between stringers with a larger Farrar efficiency around 0.7 factor and a low stringer area to reduce weight. The dimensions and farrar efficiency of the chose stringer are shown in the summary table 3.4.

Parameter	Value	Symbol
Number of Stringers	87	N/A
Stringer Pitch (mm)	117	$b$
Stringer Area ( $\text{mm}^2$ )	96.07	$A_s$
Stringer Height (mm)	32.5	$t_h$
Stringer Thickness (mm)	1.3	$t_s$
Flange Length (mm)	22	$L_f$
Skin Thickness (mm)	3.1	$t$
$A_s/bt$	0.2655	N/A
$t_s/t$	0.419355	N/A
Farrar Efficiency	0.65	N/A

**Table 3.4:** Summary of fuselage stringers parameters.**Figure 3.6:** CAD Model of Fuselage Stringers**Figure 3.7:** Detailed View of Stringer Dimensions

## 3.4 Fuselage Frames Design

The goal of this part is to size the light and heavy frames in order to minimize their area to have the less useless weight while be able to handle the load applied on it.

### 3.4.1 Light Frames Design

Being in a conceptual design approach, the C cross-section shape has been chosen as it is common for commercial aircraft [6].

The dimensions to be sized for the light frames are height  $h$ , width  $b$  and thickness  $t$ . The first dimensioning parameter is the second moment of inertia which can be determined using the following equation:

$$EI = \frac{C_f M_{ult} D^2}{L} \quad (3.11)$$

Where  $C_f = \frac{1}{16000}$  is an empirical constant and  $M_{ult}$  is the bending moment applied by the wing on the fuselage. The second moment of inertia is also calculated geometrically according to the chosen cross-section shape:

$$I = \frac{th^3}{12} + \frac{bth^2}{2} \quad (3.12)$$

The methodology was as follows: for a multitude of values of height and width, the thickness needed to support the load is calculated and the associated area  $A = (2b + h)t$  too. Physically and to be machined, a minimum thickness is required. Given a minimum required thickness, if the thickness calculated with the value of height and width is too small to support the load, the possibility of choosing these dimensions is ruled out. The process is iterated over the

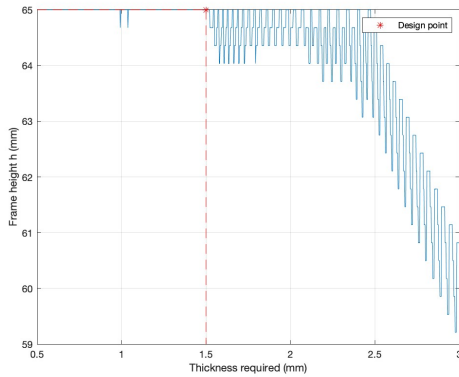


**Figure 3.8:** Evolution of optimal height with required thickness.

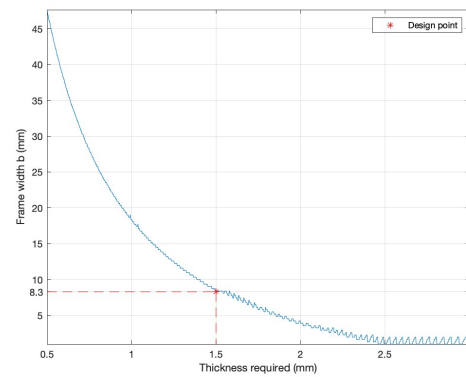


**Figure 3.9:** Evolution of optimal width with required thickness.

minimum required thickness, the results obtained are presented in Figures 3.8, 3.9 and 3.10. By researching the minimum thicknesses machinable [4], a minimum thickness value was chosen to be 1.5mm.

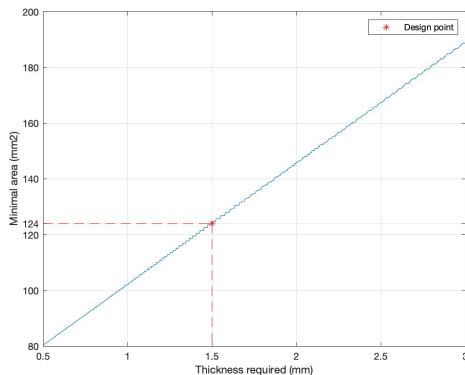


**Figure 3.10:** Evolution of minimal area with required thickness.

As final values, the light frames parameters are:

- **Height  $h$**  : 65mm
- **Width  $b$**  : 8.3mm
- **Thickness  $t$**  : 1.5mm
- **All frames weight** : 186 kg

### 3.4.2 Heavy Frames Design

The fuselage is subjected to much higher loads in the wings, t-tail and engines location. These loads cannot be supported by the light frames, which is why the aircraft has 3 heavy frames at the level of the wing spars, 2 heavy frames close to the engines and 2 others close to the t-tail. A drawing of all heavy frames location is available in Appendix I (Figure I.1).

The loads applied to the frames can be determined using the WISE curves. For a radial force  $Q$ , a tangential force  $P$  and a moment  $T$  applied at a point on the frame, the forces are distributed along the frame. Each component itself creates an axial force  $N$ , a shear force  $S$  and a moment  $M$  (indicated by the creating component  $Q$ ,  $P$  or  $T$ ). The radial force is distributed according to the equations:

$$N_Q = \frac{Q}{2\pi} \left( \frac{3 \cos \phi}{2} + (\pi - \phi) \sin \phi \right) \quad (3.13) \quad S_Q = \frac{Q}{2\pi} \left( (\pi - \phi) \cos \phi - \frac{\sin \phi}{2} \right) \quad (3.14)$$

$$M_Q = \frac{QR}{2\pi} \left( \frac{\cos \phi}{2} - (\pi - \phi) \sin \phi + 1 \right) \quad (3.15)$$

Similarly, the tangential force propagates as follows:

$$N_P = \frac{P}{2\pi} \left( \frac{\sin \phi}{2} - (\pi - \phi) \cos \phi \right) \quad (3.16)$$

$$S_P = \frac{P}{2\pi} \left( (\pi - \phi) \sin \phi - 1 - \frac{\cos \phi}{2} \right) \quad (3.17)$$

$$M_P = \frac{PR}{2\pi} \left( \frac{3 \sin \phi}{2} + (\pi - \phi)(\cos \phi - 1) \right) \quad (3.18)$$

Finally the moment generates 3 components:

$$N_T = \frac{T}{2\pi R} \left( \frac{3 \cos \phi}{2} + (\pi - \phi) \sin \phi \right) \quad (3.19)$$

$$S_T = \frac{T}{2\pi R} (1 + 2 \cos \phi) \quad (3.20)$$

$$M_T = \frac{T}{2\pi} (\pi - 2 \sin \phi - \phi) \quad (3.21)$$

The loads applied for each group of heavy frames is presented in the Table 3.5. It has been assumed that the loads are distributed equally between the different heavy frames. The load of the wings are the shear force and the bending moment at the root of the wings while the load of the engines heavy frames is the weight of the nacelle and engines. Since the aircraft has a t-tail, the load applied is the sum of the load of the horizontal tailplane and vertical tailplane.

Location	$Q$ [kN]	$P$ [kN]	$T$ [kNm]	Angular Position of Load [°]
Wings	482	333	3,147	141 & 219
T-Tail	16.1	12.0	33.9	0
Engines	7.8	24.8	40.0	72 & 287

Table 3.5: Summary of loads applied on heavy frames.

The previous equations allow us to obtain the Figures 3.11, 3.12 and 3.13. The angle 0 corresponds to the upper part of the fuselage and rotates counter-clockwise. The discontinuities appear naturally in the equations.

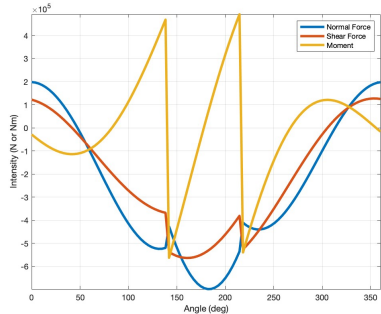


Figure 3.11: Loads distribution on wings heavy frames.

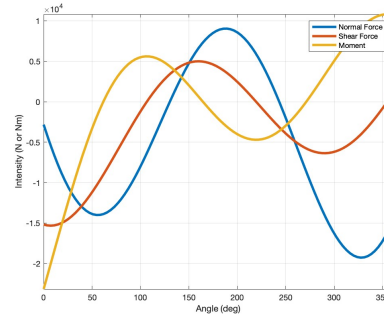


Figure 3.12: Loads distribution on T-Tail heavy frames.

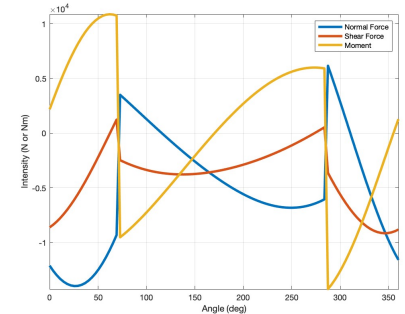


Figure 3.13: Loads distribution on engines heavy frames.

Using the same methodology as for the light frames, the final values of the heavy frames could be determined and are presented in the Table 3.6. The width should not exceed the height in order to be consistent with the C cross-section chosen. All graphs of the results are available in Appendix I.

Heavy Frames	Frames number	Height $h$ [mm]	Width $b$ [mm]	Thickness $t$ [mm]	Total Weight [kg]
Wings	3	420	79	20	977
T-Tail	2	65	65	10.4	115
Engines	2	65	65	6.4	71

Table 3.6: Summary of heavy frames dimensions.

# Chapter 4

## Wing Design

### 4.1 Loads

The three major forces acting on the wings are the inertial, aerodynamic and reaction loads. All loads were calculated for the three load cases and any of their significant variations specifically combinations of both MTOW/MZFW with  $V_a/V_d$ .

The inertial load is given as the product of the wings various masses multiplied by gravity and the load factor of the load case ( $W = -ngm$ ).

The mass of the wing and fuel in the MTOW configuration were distributed along their lengths. As the wing and therefore fuel tanks were tapered, equation 4.1 gives mass function along the span. The magnitude of  $m_{0W}$  for the wing is the value needed such that the integral of the mass function equals to the weight of one wing as shown in equation 4.2. The value of  $m_{0f}$  is calculated in the same way but the mass function must equal to the mass of fuel in the wing. The function is also integrated from the start to end of the fuel tanks as given from the conceptual design. The mass function for the fuel tanks was made equal to zero outside of the fuel tank span.

$$m = m_0 \left(1 - \frac{1-\lambda}{\frac{b_W}{2}} y\right) \quad (4.1)$$

$$\int_0^{\frac{b_W}{2}} m_{0W} \left(1 - \frac{1-\lambda}{\frac{b_W}{2}} y\right) dy = \frac{m_W}{2} \quad (4.2)$$

$$\int_{2.2}^{12.8} m_{0f} \left(1 - \frac{1-\lambda}{\frac{b_W}{2}} y\right) dy = \frac{m_f}{2} \quad (4.3)$$

The masses and therefore inertial forces from the weight of the winglets and undercarriage were added as point masses at the nearest span station. The load distribution along the semi span can be seen in figure 4.1.

The aerodynamic loads were assumed to be elliptical and therefore given by equation 4.4.

$$L = L_0 \sqrt{1 - \left(\frac{y}{\frac{b_W}{2}}\right)^2} \quad (4.4)$$

$L_0$  was determined by equating the integral of the lift distribution to half of the lift generated by the wings. The total lift generated by the wings is given by equation 4.5 as a fraction of total weight as given in equation (!!). Total weight is the relevant total mass (MTOW or MZFW) multiplied by load factor and the gravitational constant ( $L_T = ngm_T$ ). The fraction of total lift generated by the wing was calculated from the ratio of the wing lift coefficient and the total lift coefficient. These values are a result of the horizontal tail plane producing a small proportion of total lift for stability reasons. This resulted in a 99.33% of lift being generated by the wing and 0.67% by the horizontal stabiliser.

$$\int_0^{\frac{b_W}{2}} L_0 \sqrt{1 - \left(\frac{y}{\frac{b_H}{2}}\right)^2} dy = \frac{L_T}{2} \cdot \frac{C_{l,W}}{C_{l,T}} \quad (4.5)$$

In the case of landing a load factor of  $n=1$  as well as zero aerodynamic forces were assumed. This based on the assumption of a non-crash landing as well as the deployment of spoilers resulting in zero aerodynamic loads. When the plane lands there will be a reaction force given by equation 4.6. The reaction load on each equals the total aircraft weight plus the trim force needed to counter the moment generated due to the front nose-off landing case. This reaction force is halved as it is spread by the two undercarriages. The reaction force is assumed to act entirely through the span station closest to the undercarriage joint.

$$R = \frac{(m_T \cdot g + R_{trim})}{2} \quad (4.6)$$

Loads experienced along the span of the wing were then summed to give the combined loads. The shear force at each span station can then be calculated by integrating the combined loads from each span station to the end of the semi span which can be seen in figure 4.1. Bending moment was then found by integrating the shear force distribution which can be seen in figure 4.1.

Torque was calculated using equation 4.7 according to figure 4.1. The values of  $b_1, b_2, b_3, b_4$  and  $a$  are the distances from the shear centre to the centre of masses of the wing box, fuel tank, undercarriage, winglets and the distance to the aerodynamic centre respectively. These distance change as the chord changes but remain at constant chord% and are given as follows. Torque was calculated relative to the shear centre which was assumed to be in the middle of the wing box at 39.5%. Lift force acts at the aerofoil's aerodynamic centre, which was taken to be 26.5% from experimental data. The wing box was assumed to act through the centroid of the wing box which was calculated by integrating the aerofoil shape between the spars and was found to be at 52%. The weights of fuel, winglets and undercarriage were taken at 40%, 50% and 78% respectively all according to the conceptual design.

$$\tau = La + W_W b_1 + W_f b_2 + W_{UC} b_3 + W_{wl} b_4 - M_0 \quad (4.7) \qquad M_0 = \frac{1}{2} C_M \rho v^2 S_{ref} c \quad (4.8)$$

$M_0$  is the moment generated as a result of the aerofoil generating lift and is given by equation 4.8.  $C_M$  is a function of angle of attack (as calculated from  $V_a$  and  $V_d$  using coefficient of lift equation) and is found using XFOIL. XFOIL is appropriate to calculate  $C_M$  as it is a mainly inviscid phenomena [23] and is more precise than the available experimental data.  $M_0$  at each station was multiplied by the corresponding value of lift in order for  $M_0$  to also vary elliptically [6].  $M_0$  was then scaled such that its integral still equalled  $M_0$  after applying the distribution shape.

The highest magnitude at each station for each quantity as seen in figure 4.1 gives the most constraining case each span section of the wing will be subject to. These values are therefore the basis of all future sizing.

Therefore it can be seen that load cases 1 and 3 are the most constraining. The highest shear forces and bending moments occur at symmetric flight with MTOW evaluated at  $V_a$  and  $V_d$ , while the most constraining torques occur mostly in the MZFW configuration. Thereby the torque at the root and at the tip or the wing is constrained by the landing load case with MTOW but from span station 0.89m to span station 12.8m it is constrained by the flight at  $V_a$  and  $V_d$  with MZFW.

## 4.2 Stringer-Panel Design

In this part the methodology used to design the stringer-panel will be explained and results of this methodology will be presented. For this part, the aim is to find the dimensions of the skin-stringer panel. This represents the sizing of the skin thickness and the cross section area of the stringers to fight against the bending moment. To carry out the calculation, assumptions were made. The number of stringers  $n$  remains the same along the wing box. The dimensions of the stringers (height  $h$  and thickness  $t_s$ ) are also kept constant along the wing for ease of machining. The methodology will be detailed step by step and the results will be presented at the end.

1. From the position along the wing, the dimensions of the wingbox can be calculated and one can know what bending moment the wing feels.
2. Then, with the values chosen for the shape of the stringer, the cross-sectional area of the stringers can be calculated. The compressive load of unit length  $N$  can also be computed using eq.4.9.

$$N = \frac{M}{Height_{box} Width_{box}} \quad (4.9)$$

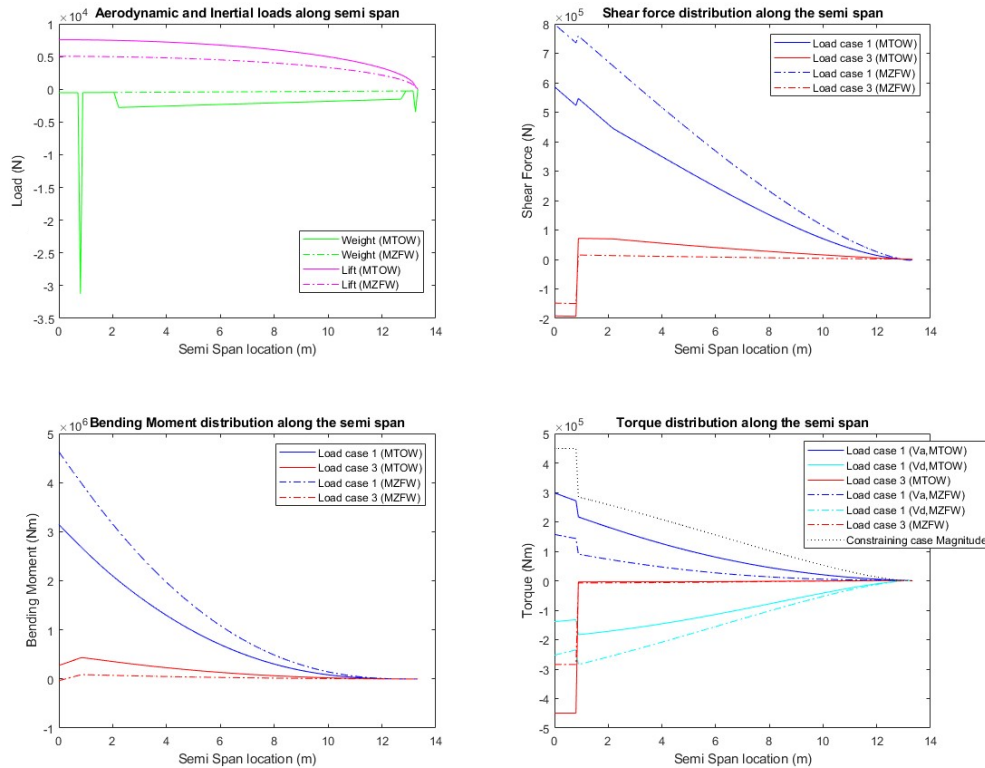


**Figure 4.1:** Loads, shear forces, bending moments and torques experienced by wing along span.

Where  $M$  is the bending moment.

- With the above values it is possible to calculate the thickness of the skin ( $t$ ) using eq.4.10 [6].

$$t_{skin} = \left( \frac{Nb^2}{3.65E} \right)^{1/3} \quad (4.10)$$

Where  $b$  is the stringer pitch or the panel width.

- Now that the skin is known it is possible to calculate  $\sigma_0$ ,  $As/bt$  and  $ts/t$ .  $As$  refers to the cross-section area of the stringer.

$$\sigma = \frac{N}{t} \quad (4.11)$$

- With  $ts/t$  and  $As/bt$  it is possible to find  $\sigma_{Cr}/\sigma_0$  and the Farrar efficiency using graph in A.
- Finally, it is possible to compute  $\sigma_{Cr}$ . At this stage it is important to have a sigma lower than the yield stress of the material. Moreover, the condition in shear and compression:

$$R_c + R_s^2 < 1 \quad (4.12)$$

Where  $R_c = \frac{\sigma_0}{\sigma_{Cr}}$  and  $R_s = \frac{\tau_0}{\tau_{Cr}}$  with  $\tau_0$  the shear stress in the skin and  $\tau_{cr}$  the Tresca shear yielding stress.

is another constraint on  $\sigma_{Cr}$  and prevents from having a too low  $\sigma_{Cr}$ . These two conditions have constrained the stringer spacing to the chosen value and explains the fairly low number of panels chosen.

- The technique for finding the rib spacing is to equalize the intial buckling stress to the mean stress. And The mean stress can be calculated using the equation 4.13.

$$\sigma_f = F \sqrt{\frac{NE}{L}} \quad (4.13)$$

It is then possible to get the ribs spacing L .

Once the rib spacing is obtained, the methodology is repeated at the position of the new ribs. This operation is repeated until the wing tip is reached. At each new position, the thickness of the skin changes. It is therefore possible to know the number of ribs required in the wing. Thus, several stringer geometries have been tested with this method.

In this iterative process there are several constraints to respect: the height of the stringer should not exceed the height of the wingbox, the  $\sigma_{Cr}/\sigma_0$  ratio needed to be higher than 1 to respect condition 4.12 and the Farrar efficiency had to be on average as high as possible. The final design was chosen because it met all the constraints and had the highest average Farrar efficiency. Its characteristics are presented in the following table:

<b>Number of stringer</b>	7
<b>Stringer Thickness (mm)</b>	7
<b>Stringer Height(mm)</b>	60
<b>Skin thickness (root) (mm)</b>	11.7
<b>Skin thickness (tip) (mm)</b>	1

**Table 4.1:** Geometry of the stringer-skin of the wing

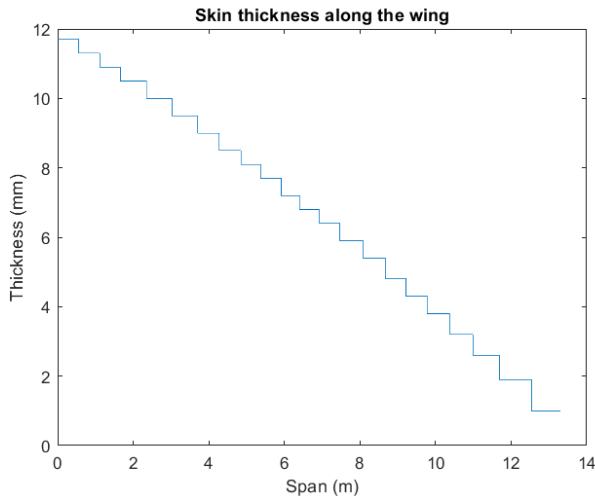


**Figure 4.2:** Skin thickness along the wing

## 4.3 Spar Design

### 4.3.1 Spar Web Design

This section will explain how the thickness of the spar web is designed along the wing.

What will dimension the spars are the torque and shear loads. Therefore, the shear flow induced by the torque  $q_0$  and the shear load  $q_2$  along the wing need to be found.

$$q_0 = \frac{T}{\frac{2}{cb}} \quad (4.14)$$

$$q_2 = \frac{V}{\frac{2}{b}} \quad (4.15)$$

where  $T$  is torque load at specific station,  $V$  is the shear load at specific station,  $c$  is the distance between spars,  $b$  is the web height.

It is now possible to compute the shear flow in the front and the rear spar.

$$q_{rear} = q_2 + q_0 \quad (4.16)$$

$$q_{front} = q_2 - q_0 \quad (4.17)$$

Furthermore, given the geometry of the wing box, the shear buckling coefficient is always equal to 8.1 according to the graph in appendix C. Indeed, the ratio  $a/b$  (where  $a$  is the distance between two web panels (1 panel in this

case) and  $b$  is the wingbox height) is still very high. At the root, where the ratio is smallest, it is already 34. It will only increase along the wing. Thus, the asymptote is reached for the clamped edge case: 8.1.

It is therefore possible to compute the thickness of the rear and the front spar by equalizing panel clamped shear stress with panel buckling stress 4.18. Thicknesses have been rounded up to the nearest millimetre.

$$t = \left( \frac{qb}{K_s E} \right)^{\frac{1}{3}} \quad (4.18)$$

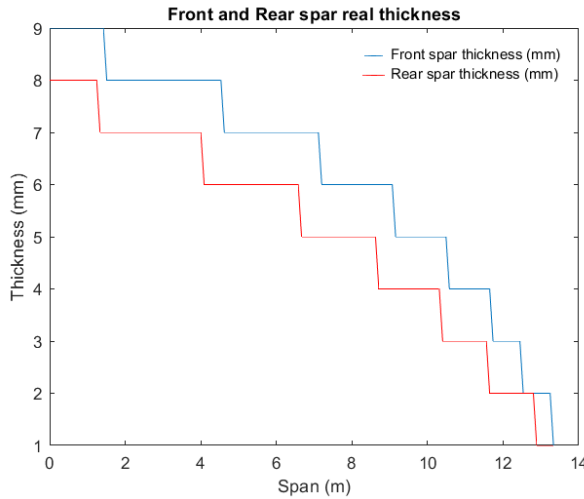


Figure 4.3: Front and Rear Spar Web Thickness

Spar Web thickness	Root	Tip
Rear Spar (mm)	8	1
Front Spar (mm)	9	2

Table 4.2: Front and Rear Spar Web Thickness

### 4.3.2 Spar Cross-Section Design

Now that the thickness of the spar web has been designed, the cross section of the spar and more precisely the spar cap can be designed. As previously explained, 98% of the bending moments are accounted for by the skin while 2% are accounted for by the spar caps. From a study of previous aircraft spars were found to be made most commonly of aluminium. From this the optimal material was found to be Aluminium 2014. Its most constraining yield strength is a tensile yield strength of 414 MPa. This then gives the spar  $I_{xx}$  required to take 2% of the bending moment as given by equation 4.19 where  $\sigma$  is the most constraining yield strength.

$$\sigma = \frac{Mc}{I_{xx}} \quad (4.19)$$

The spar heights and web thicknesses are already given from the spar sizing therefore only the spar cap breath  $b$  and spar cap thickness  $t_1$  can be varied. There is an infinite number of combinations of these variables that would satisfy the required  $I_{xx}$ . Therefore a optimisation study was conducted to minimise volume as it results in the minimum mass and price of material. For this optimisation, equation 4.20 was solved for  $b$  and values for  $b$  were systematically determined for each  $t_1$  in a large range of combinations which satisfied the necessary  $I_{xx}$ . This minimum mass combination was then calculated at the same intervals at which the spar web thickness was discretized. This yields the spar cap heights and thicknesses along the spar spans for the front spar which can be seen in figures 4.4 and 4.5 and the rear spar as seen in figures 4.6 and 4.7. The determined spar cap thicknesses were rounded to the nearest millimetre for manufacturing reasons and the corresponding  $b$  was chosen.

$$I_{xx} = \frac{1}{6}bt_1^3 + \frac{1}{2}bt_1(D - t_1)^2 + \frac{1}{12}t_2(D - 2t_1)^3 \quad (4.20)$$

From table 4.3 it can be seen that none of the dimensions are unreasonably large or small in a way that would be physically impossible or prohibitively expensive to manufacture.

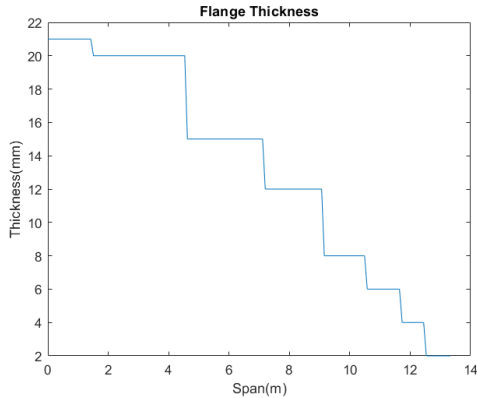


Figure 4.4: Flange Thickness of front spar

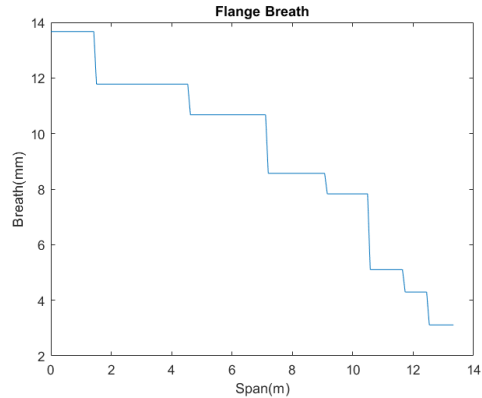


Figure 4.5: Flange Breath of front spar

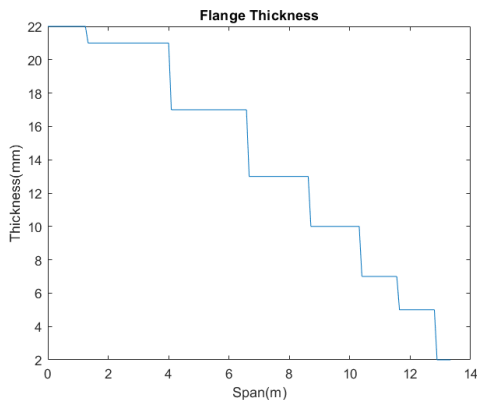


Figure 4.6: Flange Thickness of rear spar

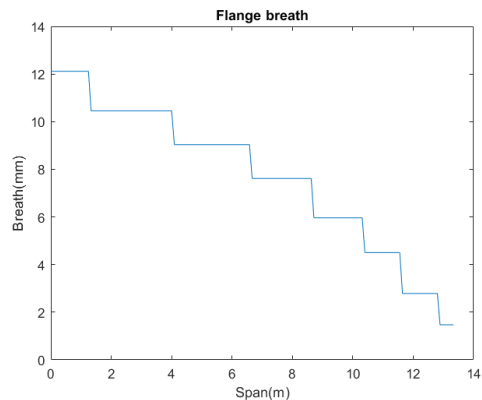


Figure 4.7: Flange Breath of rear spar

Dimensions (mm)	Root (Front Spar)	Root (Rear Spar)	Tip (Front Spar)	Tip (Rear Spar)
Flange Thickness	21	22	2	2
Flange Breath	13.7	12	3	2

Table 4.3: Spar Cap design for the wing

## 4.4 Rib Design

In this section, the design of the ribs will be explained. From the stringer panel section, the numbers of ribs has been determined : 22 ribs are present in the wing.

The objective is to find the thickness of all the ribs that make up the wing. To do this, the Effective Panel Thickness at each ribs position need to be computed. This thickness can be calculated using the equation 4.21

$$t_e = t_{skin} + \frac{As}{b} \quad (4.21)$$

Then, assuming that the ribs at a given station have the wing box values as their dimensions, the second moment of

inertia  $I$  can be determined. With this value, the crush load which will allow to find the thickness of the ribs can be computed. The equation to compute this crush load is eq 4.22.

$$F = \frac{M^2 s h_c t_e c}{2 E I^2} \quad (4.22)$$

Finally, to find the thickness of the ribs the technique consists in equalizing the first buckling stress to the rib crush stress.

$$\sigma_{rib} = \frac{F}{t_r c} \quad (4.23)$$

$$\sigma_{cr,buckling} = 3.62E \left( \frac{t_r}{h_c} \right)^2 \quad (4.24)$$

Therefore the thickness of the ribs is accessible at each ribs station:

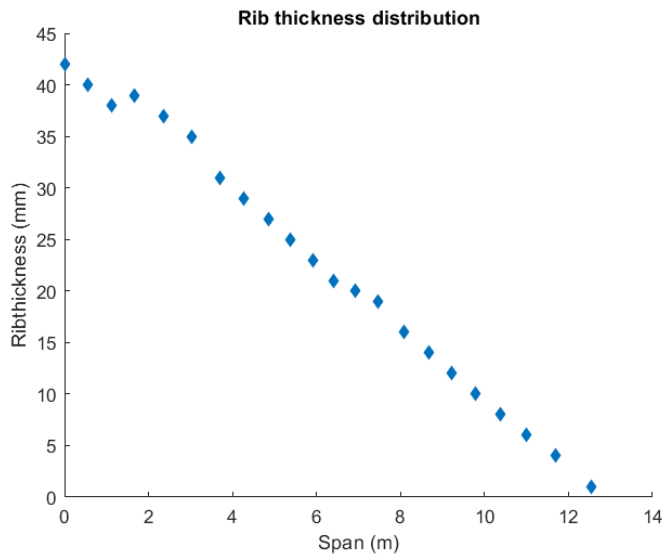


Figure 4.8: Ribs Thickness

Number of ribs	Last Rib location	Rib thickness (root)	Rib thickness (tip)
22	80 cm from the tip	42 mm	1 mm

Table 4.4: Summary of rib design

By calculating the stress in each rib, it was found that the stress was too high in the ribs near the root. In a next iteration it would be important to increase the thickness of the ribs and to change the material for the first ribs.

## 4.5 Summary

### 4.5.1 Wing Layout

The following figure shows the arrangement of the different elements described earlier in this report. The ribs were placed parallel to the fuselage. As said in 1.2.2, this may result in a higher weight but it allows the aerodynamic shape of the wing to be maintained in a better way. It seemed at first that keeping the aerodynamic shape was more important. In a future iteration it would be interesting to see the impact of ribs perpendicular to the leading edge.



Figure 4.9: Wing Layout

### 4.5.2 Weight of Components

This section provides a summary of all the masses of all the elements presented above.

- Stringer panel mass calculation: First, the volume of the stringer panel must be determined between each ribs station. To do so the effective thickness will be used.

$$V_{\text{Stringer panel}} = t_e n_s b_s L \quad (4.25)$$

where  $t_e$  is the effective thickness,  $n_s$  the number of panel,  $b_s$  the stringer spacing and  $L$  the rib spacing. And then to get the mass, the volume must be multiply by the density. The density of the upper wing material is 2.8 and the density for the lower wing material is 2.78. By adding the mass of the lower and the upper wing, the final mass of the skin can be obtained.

- Spars mass calculation : First, the volume of the spar web will be determined and then the volume of the spar cap will be calculated. Thus the total volume of the spar is given by the equation 4.26

$$V_{\text{spar}} = h_{\text{spar}} t_{\text{web}} l_{\text{station}} + 2(b_{\text{flange}} - t_{\text{web}})t_{\text{flange}} l_{\text{station}} \quad (4.26)$$

where  $h_{\text{spar}}$  is the height of the spar at a given station,  $t_{\text{web}}$  is the thickness of the web at a given station,  $l_{\text{station}}$  is the distance between two stations,  $b_{\text{flange}}$  is the width of the spar cap at a given station,  $t_{\text{flange}}$  is the thickness of the flange at a given station. This calculation has to be done for the front and the rear spar. Then using the density of the Aluminium 2014-T6 (2.8) the mass can be found.

- Ribs mass calculation : The volume of each ribs must be determined following 4.27

$$V_{\text{ribs}} = c_{\text{box}} h_{\text{box}} t_{\text{ribs}} \quad (4.27)$$

So using the density of the material chosen for the ribs it is possible to get access to the mass of the ensemble of the ribs.

Elements	Mass [kg]
Skin-Stringer Panel	1464
Spars	144
Ribs	1068
Total	2676

**Table 4.5:** Weight summary of each component of the wing

So the total weight of a single wing is about 2676 kg. In the conceptual design the weight found was about 1595 kg.

# Chapter 5

## Vertical Stabilizer Design

### 5.1 Loads

The most constraining loading of the vertical tail plane is the case of one engine inoperative (Load case 2). In this case the rudder must produce a sideways forces which creates a moment equal in magnitude to the asymmetric force of the still operating engine as shown in figure 5.1 .

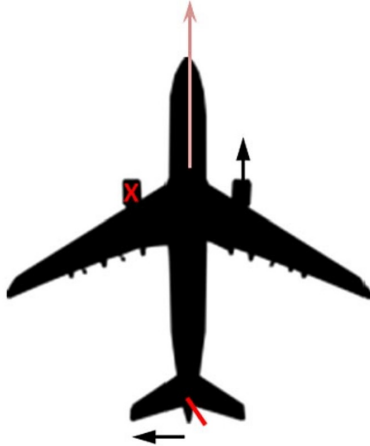


**Figure 5.1:** Load case 2 assumed flight condition and moment balance

$$L = -\frac{T}{2} \cdot \frac{y_{cg} - y_1}{x_{cg} - x_2} \quad (5.1)$$

The required sideways lift force is given by equation 5.1 and depends on the coordinates of the plane's centre of gravity ( $x_{cg}, y_{cg}$ ), vertical tail-plane ( $x_2$ ) and the still operating engine ( $y_1$ ). The planes centre of gravity changes however, depending on the amount of fuel in the aircraft, therefore loads on the vertical tail were considered for both MTOW and MZFW. As this design's empennage is a T-tail, lift is assumed to follow a rectangular distribution due to the end cap affect of the horizontal stabiliser [23]. Load case 2 also assumes that the rudder is deflected such that there is no side slip angle. The sideways lift force was therefore distributed only over the tail span which the rudder covers which can be seen in figure 5.2. Shear force and the bending moment along the span were calculated in the same way as for the wing previously. Torque was also calculated in a similar way but with the only contribution being from the lift force as their are no other forces considered and as the symmetric aerofoil was assumed to have a zero  $M_0$  as the angle of attack required to generate the necessary sideways lift was very small (0.68 degree). The torque distribution can also be seen in figure 5.2.

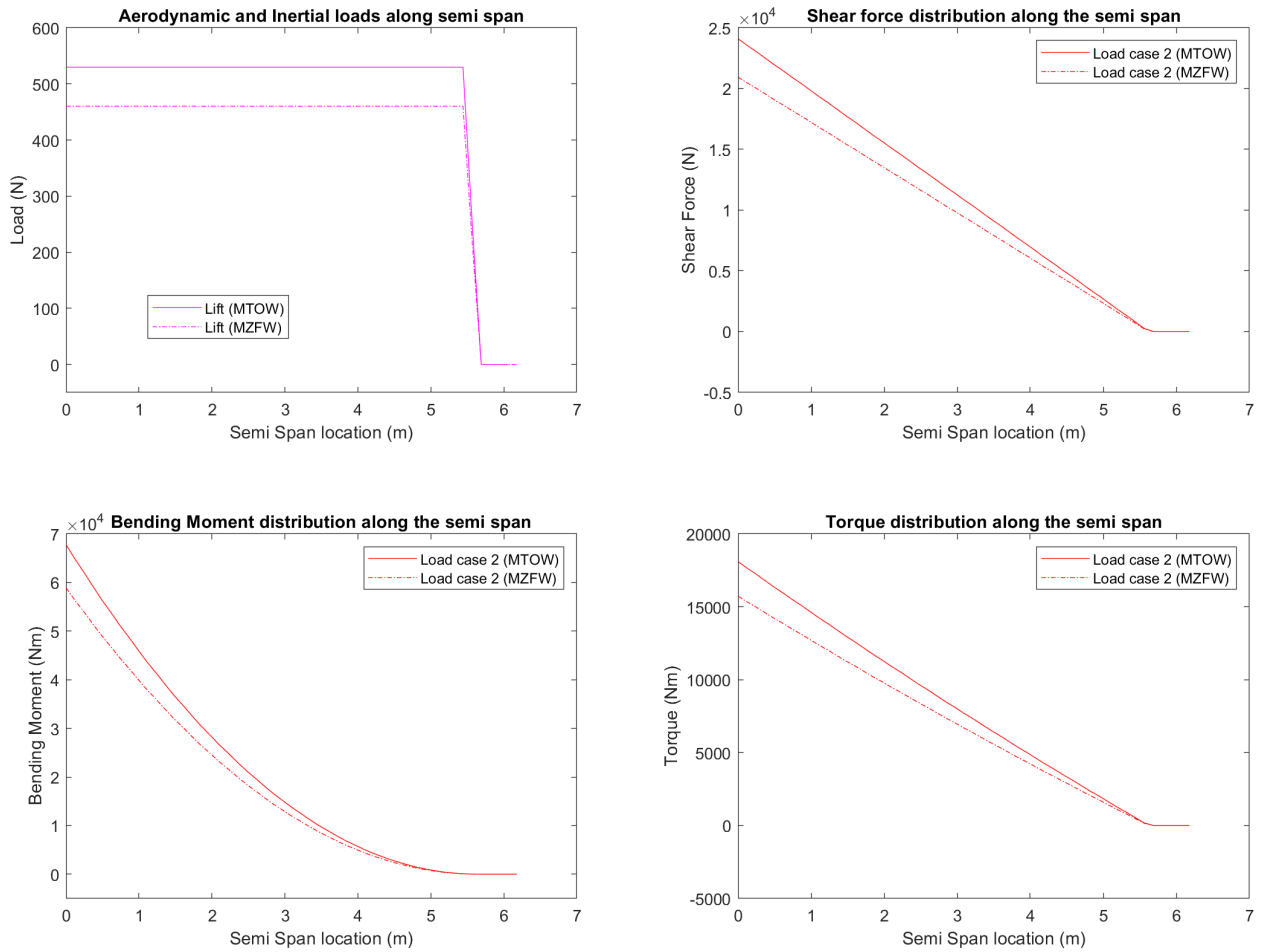


**Figure 5.2:** Loads, shear forces, bending moments and torques experienced by Vertical tail along span.

As can be seen in figure 5.2, the most constraining case for shear force, bending moment and torque is the MTOW case as a greater smaller moment arm requires a greater sideways lift. Overall the shear force, bending moment and torque are likely less than other aircraft, as this design's rear fuselage mounted engines reduces the moment arm of the still operating engine. This will reduce the weight of the vertical tail which will reduce the weight penalty typical of T-tails compared to conventional empennages.

## 5.2 Spar Design

### 5.2.1 Spar Web Design

The same methodology as section 4.3 is applied for the vertical stabiliser spar web design and the following plots represent the ideal and real front and rear spar thickness distribution (real thicknesses have been rounded up to the nearest millimetre because of manufacture constraints):

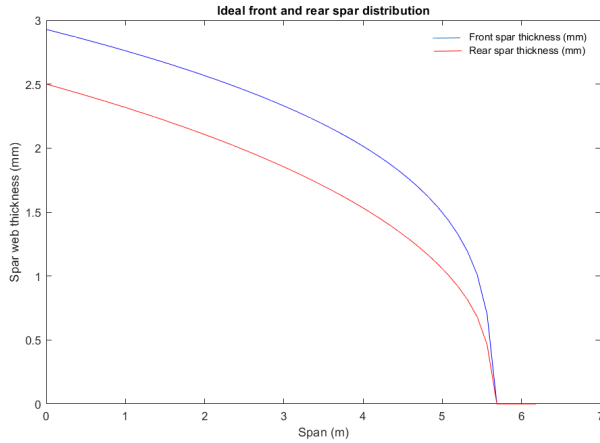


Figure 5.3: Ideal front and rear spar thickness

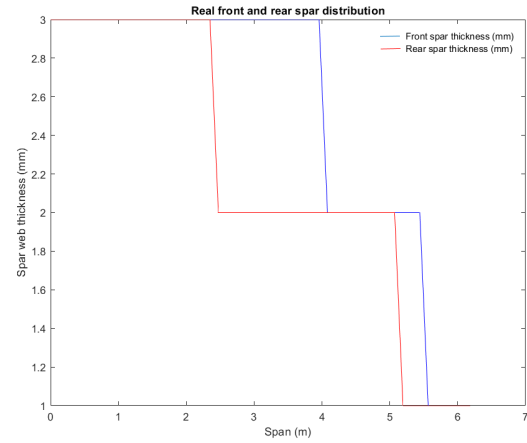


Figure 5.4: Real front and rear spar thickness

The following table summarises the geometry of the root and tip wing boxes of the vertical stabiliser:

Section	Width	Mean Spar Height	Front Spar thickness	Rear Spar thickness
Root	3.2 m	0.89 m	3 mm	1 mm
Tip	1.1 m	0.28 m	3 mm	1 mm

Table 5.1: wing boxes geometry for the vertical stabiliser

## 5.2.2 Spar Cross Section Design

By following the methodology explained in 4.3.2 and by assuming the same assumption : 98% of the bending moment is taken by the wing whereas the 2% left are taken by the spar cap, it is possible to compute the flange thickness and the flange breath along the wing. The results are shown in the next figures.

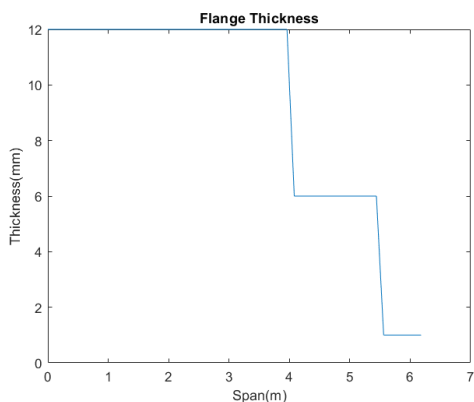


Figure 5.5: Flange Thickness of front spar

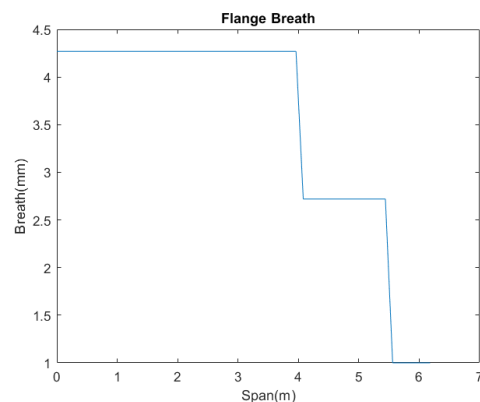


Figure 5.6: Flange Breath of front spar

Dimensions (mm)	Root (Front Spar)	Root (Rear Spar)	Tip (Front Spar)	Tip (Rear Spar)
Flange Thickness	12	1	12	4
Flange Breath	4.3	1	4.6	1.5

Table 5.2: Spar Cap design for the Vertical Tail

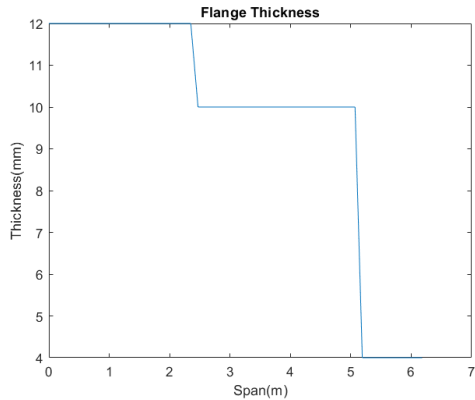


Figure 5.7: Flange Thickness of rear spar

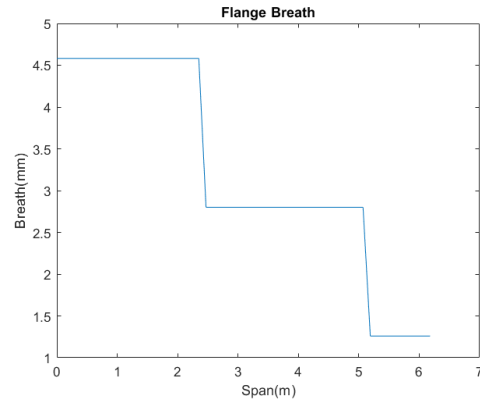


Figure 5.8: Flange Breath of rear spar

## 5.3 Stringer-Panel Design

The design of the stringer panel of the vertical stabiliser is very similar to the stringer-panel design of the wing. However, since the ratio of compression  $R_c$  (coming from condition 4.12) is less constraining for the vertical stabiliser than for the wing, the design of the stringer-panel and the ribs layout will now consider testing different number of panels. Finally, the selection of the optimal number of panels will be led using a weight and cost optimisation.

### 5.3.1 Sizing Methodology

For each number of stringer-panels the following guidelines have been applied in order to select suitable values of stringer height  $h_s$  and stringer thickness  $t_s$  and therefore find the rib spacing using graphs in A:

- The stringer height  $h_s$  is kept constant along the span and is restricted by the height of the front spar at the tip (the most constraining one)
- the stringer thickness  $t_s$  is kept constant along the span for the same reason as section 4.2. Moreover, Z-stringers are used because of section 1.2.2
- The ratio  $\frac{h_s}{t_s}$  should stay in a certain range of values [10]
- A stiffening ratio  $\frac{A_s}{bt}$  less than 0.5 should not be used because of panel damage tolerance considerations [10]
- The stringer flange width to stringer height ratio  $\frac{d_s}{h_s}$  should stay constant for graphic reading
- The condition in shear and compression of section 4.2 on the ratios  $R_c$  and  $R_s$

Some of these assumptions are summarised in the following table:

$h_s$	$\frac{h_s}{t_s}$	$\frac{A_s}{bt}$	$\frac{d_s}{h_s}$	$R_c + R_s^2$
Lower than 100 mm	Between 16 and 22	Greater than 0.5	0.3	Lower than 1

Table 5.3: Summary of the guidelines

After selecting suitable values for  $h_s$  and  $t_s$ , the same methodology as section 4.2 is followed to compute the skin thickness  $t$  and the ribs spacing along the whole tail span.

The following plot shows an example of skin thickness computing with a number of 17 panels:

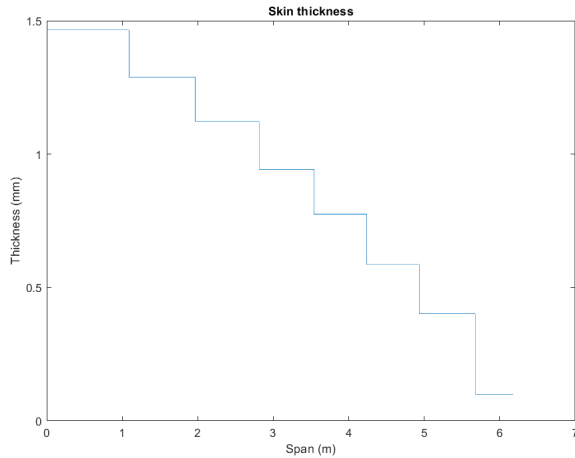


Figure 5.9: Skin thickness distribution

The optimal number of panels and thus number of stringers will be selected after a weight and cost analysis in section 5.5.

## 5.4 Rib Design

Once the ribs layout along the span is known for each number of panels tested, the rib thickness is found at each rib station using the method of section 4.4.

The following plot shows an example of rib thickness computing with a number of 17 panels:

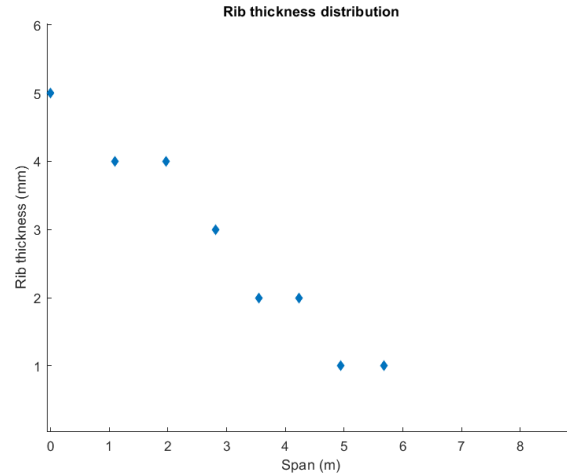


Figure 5.10: Rib thickness distribution

The next section will compare the weight and cost of the ribs structure depending on the number of stringers. After this analysis, the ribs spacing and the rib thickness distribution will be known throughout the span for the optimal number of panels

## 5.5 Weight and Cost optimisation

This section will present the results of a weight and cost comparison of the tail structure between different number of panels. For each number of panels, the methodology consists to:

- Find the total volume of material used for the stringer+skin structure:

$$V_s = N_p * b * t_e * L \quad (5.2)$$

Where  $N_p = n + 1$  is the number of panels and  $t_e = t + \frac{A_s}{b}$

- Find the weight of each material used for the stringer+skin structure using the density.
- Find the total volume of material used for the rib structure for each number of panels :

$$V_r = C_{box} * H_{box} * t_{ribs} \quad (5.3)$$

- Find the weight of each material used for the rib structure using the density.
- Plot the total weight of the whole structure as a function of  $N_p$
- Find the cost of each material used for the whole structure using the Cost/kg
- Plot the total cost for the structure as a function of  $N_p$

The results of this procedure are the following :

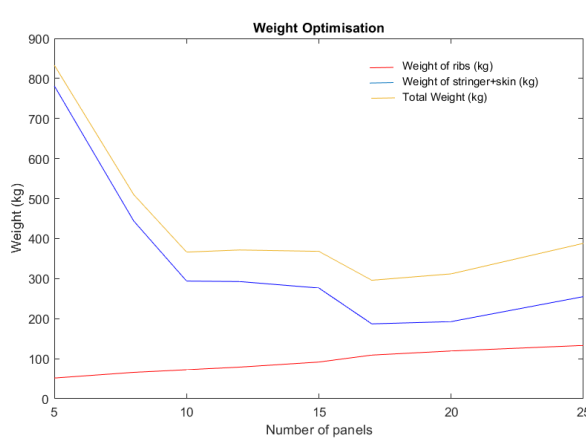


**Figure 5.11:** Weight Optimisation

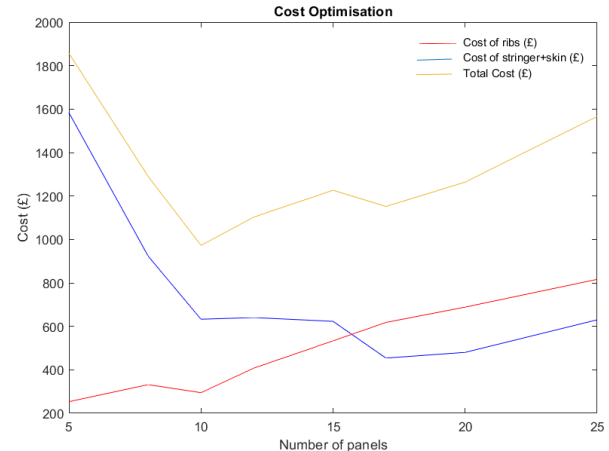


**Figure 5.12:** Cost Optimisation

The first plot highlights a clear optimum for the total weight for 17 panels, thus 16 stringers. Moreover, the second plot highlights 2 local minima for 10 and 17 panels with a global minimum at 10 panels. However, the weight optimisation prevails on the cost optimisation, thus **the design selected is 17 panels**.

### 5.5.1 Results

The following tables summarise these two designs:

<b>Number of stringer</b>	17
<b>Stringer Thickness (mm)</b>	2
<b>Stringer Height(mm)</b>	44
<b>Skin thickness (root) (mm)</b>	1.5
<b>Skin thickness (tip) (mm)</b>	1

**Table 5.4:** Geometry of the stringer-skin of the vertical stabiliser

Number of ribs	Last Rib location	Rib thickness (root)	Rib thickness (tip)
8	51 cm from the tip	5 mm	1 mm

**Table 5.5:** Summary of rib design

## 5.6 D-Cell Design

Now that the rib and stringer-panel design is done by the selection of an optimal number of stringers, the D-cell of the vertical stabiliser can be sized.

The D-Cell plays a crucial role in withstanding shear loads as it serves as the leading edge section of the stabiliser. Its design is determined by the buckling behaviour of the D-Cell when subjected to shear loads. The equation provided below defines the shear buckling stress of a curved panel, which guides the D-Cell design for the vertical stabiliser:

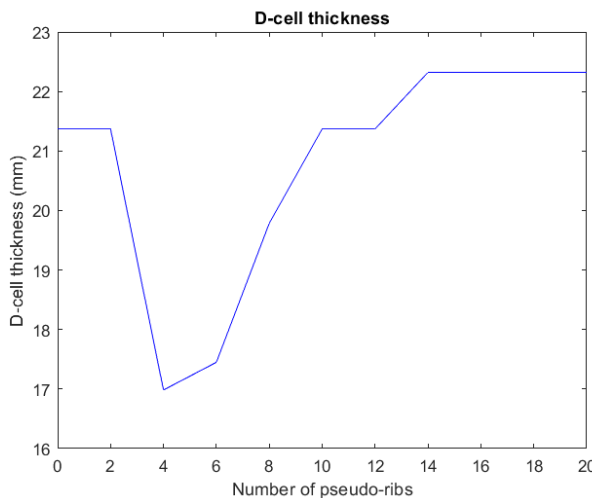
$$\tau_{Cr} = K_s E \left( \frac{t_D}{b_D} \right)^2 \quad (5.4)$$

In this equation,  $t_D$  is the D-cell skin thickness,  $b_D$  the curved panel length and  $K_s$  the curved panel buckling coefficient in shear which can be found using graphics in Appendix B.

Using equation 5.4 and graphics in Appendix B, the following iteration will be considered to size the D-cell for a given number of pseudo-ribs:

- For the first iteration,  $t_d$  is equal to the skin thickness at the root
- For this value of  $t_d$ ,  $K_s$  is found on the graphics and thus  $\tau_{Cr}$  can be computed using equation 5.4
- Since the optimal sizing is obtained for  $\tau_{Cr}$  equal to the Tresca shear yielding stress of the material chosen [24], the value of  $t_d$  is then adjusted to satisfy this condition
- Consequently, the value of  $K_s$  found on graphics in Appendix has changed by this adjustment
- Repeat the process until the value of the D-cell thickness has converged.

This operation has been repeated for multiple number of pseudo-ribs between 0 and 20 to compute the D-cell thickness:

**Figure 5.13:** D-cell thickness vs Number of pseudo-ribs

In the same way as 5.5, the weight and cost of each number of pseudo ribs configuration is computed and the following plots allow to find the optimal number of pseudo-ribs which minimise weight and cost:

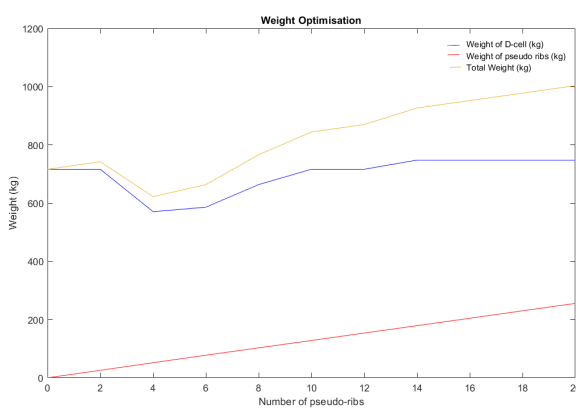


Figure 5.14: Weight optimisation

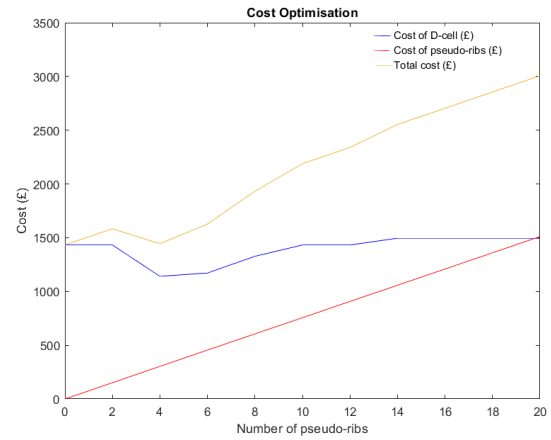


Figure 5.15: Cost optimisation

The following table summarise the results of the D-cell design:

Number of pseudo-ribs	D-cell thickness	$\tau_{Cr}$
4	17 mm	172.5 Mpa

Table 5.6: Summary of D-cell design

## 5.7 Summary

### 5.7.1 Vertical Tail Layout

The following figure shows the arrangement of the different elements described earlier in this report. As said in 1.2.2, this may result in a higher weight but it allows the aerodynamic shape of the wing to be maintained in a better way. It seemed at first that keeping the aerodynamic shape was more important. In a future iteration it would be interesting to see the impact of ribs perpendicular to the leading edge.

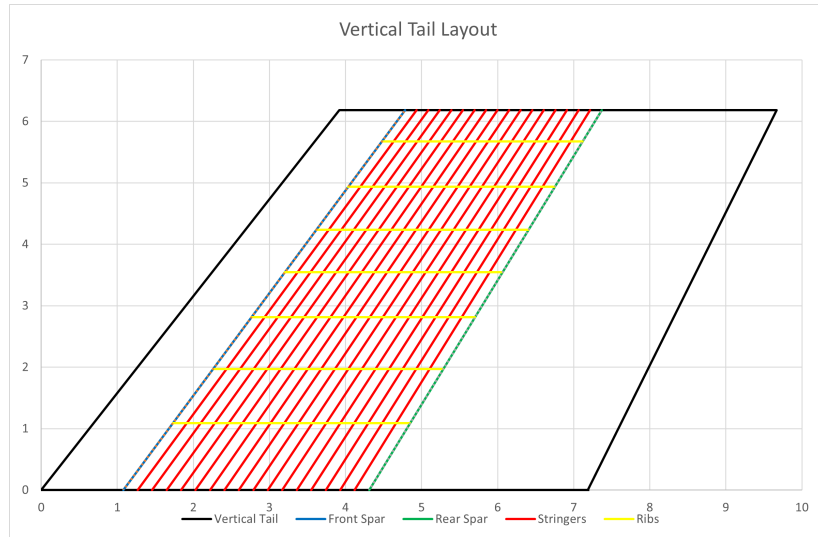


Figure 5.16: Vertical Tail Layout

# Chapter 6

## Composite Horizontal Stabiliser Design

### 6.1 Loads

Similar to the wing, the main loads which apply to the horizontal stabiliser are aerodynamic and inertial loads. The inertial loads consist only of the distributed weight of the tapering tail: This is calculated using the same equation 4.2 as the wing but with a different taper ratio. The aerodynamic loads are again assumed to be elliptical as given by equation 4.4.  $L_0$  is given by equation 6.1 which accounts for the percentage of lift generated by the horizontal tail plane.

$$\int_0^{b_{1/2,H}} L_0 \sqrt{1 - (\frac{y}{b_{1/2,H}})^2} dy = \frac{L_T}{2} \cdot \frac{C_{l,H}}{C_{l,T}} \cdot \frac{S_H}{S_W} \quad (6.1)$$

Once again load case 1 considered for the horizontal tail at combinations of  $V_a/V_d$  and MTOW/MZFW. load case 2 is also significant when sizing the horizontal tail plane. As mentioned previously, in load case 2 the rudder is deflected to produce a sideways force to counter the one inoperative engine. Producing such a sideways force creates a difference in pressure between the "top" and the "bottom" of the rudder as seen in figure 6.1 which causes positive and negative lift forces (in red) on either side of the horizontal tail plane. The dynamic pressure difference on the top and bottom surfaces are given by equation 6.2 where the values of  $C_l$  correspond to the integral of pressure coefficient data on just the top or bottom surfaces, taken at the appropriate angle of attack needed to generate the required sideways lift.

$$q = \frac{L}{C_L S} \quad (6.2)$$

The dynamic pressure was then multiplied by half the horizontal tail area to calculate the overall load. This force was then assumed to decay exponentially with distance from the vertical tail plane as seen in figure 6.1. The values were then scaled such that their integral totalled the overall load.

This load created by asymmetric pressure is different for MTOW and MZFW as they require different sideways lift values and therefore angle of attacks. The loads, shear force, bending moments and torque are then calculated in this combined (1+2) load case. Specifically in the most constraining case of a negative lift at MZFW as seen in figure 6.2.

### 6.2 Composite Material Selection

One of the empennage structures was decided to be made of composite materials according to the design brief. It was chosen to make the horizontal stabiliser of composites for the following reasons: The main reason is that the weight reduction of a composite horizontal stabiliser also reduces the weight acting on the vertical stabiliser of a T-tail configuration such as this design. Making the horizontal tail-plane of composites aims to reduce the weight penalty typical of a T-tail empennage versus a conventional configuration. Secondly, due to this design's rear mounted engine, the vertical tail may experience high temperatures due to its vicinity to the engines jet wash. This is significant as the performance/properties of composites can vary significantly with temperature. The horizontal tail plane however is sufficiently above the engines and therefore is assumed to be unaffected by it.

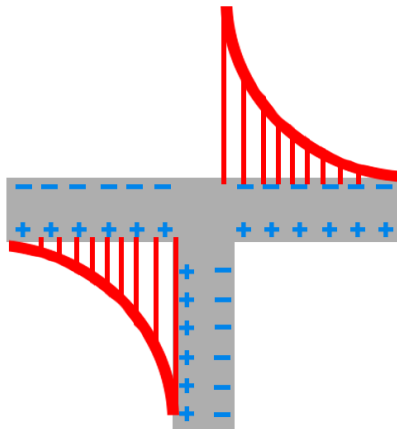


**Figure 6.1:** Lift Distribution from Asymmetric Pressure in OEI case

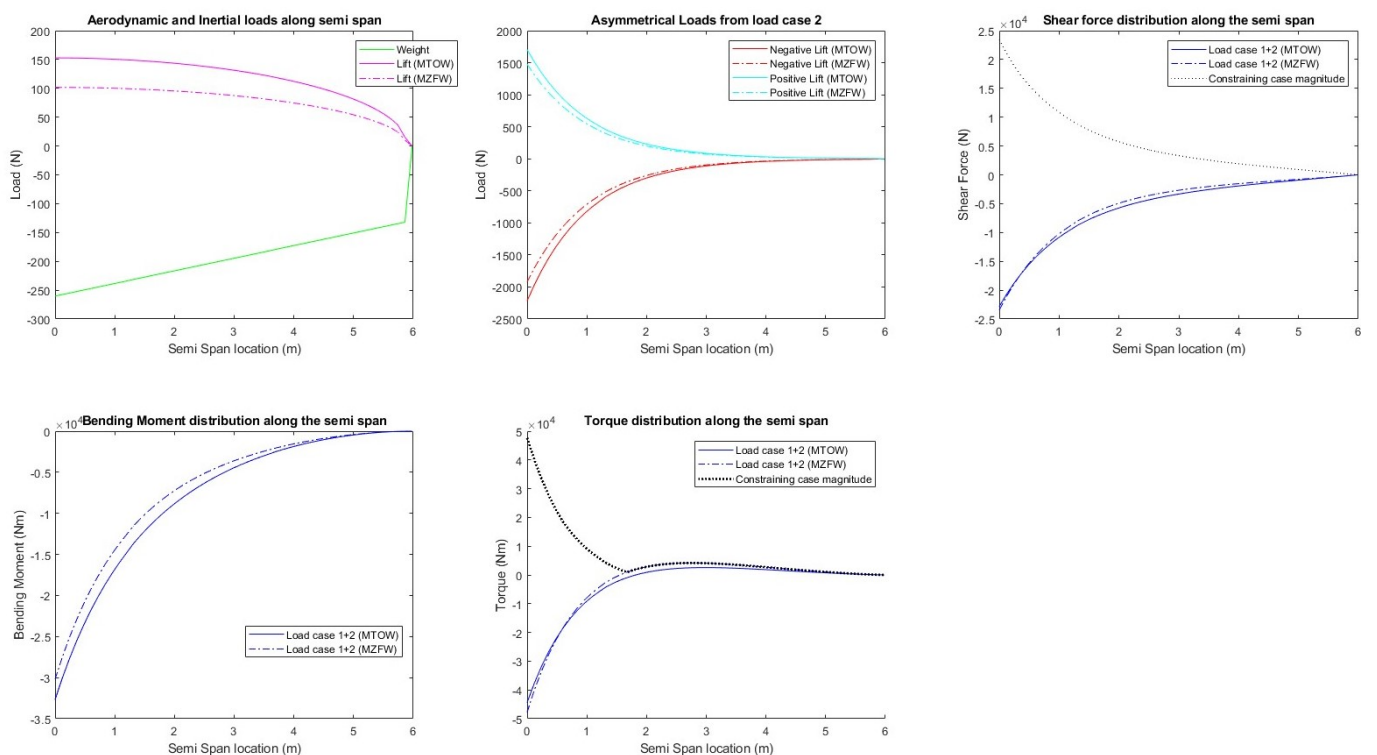


**Figure 6.2:** Loads, shear forces, bending moments and torques experienced by Horizontal tail.

As discussed previously in similar aircraft, carbon and glass fibre are the most common choices for composite components on an aircraft [12]. To choose between these two alternatives, initially a coarse combined merit index was used. The coarse merit index is the average of merit indices given by equations 2.2, 2.4, 2.5 and the overall direct yield strength merit index  $M_\sigma$  as explained later and was calculated with data from the software Granta.

The first constituent merit index  $M_f$  is to evaluate the materials fatigue properties as the horizontal tail-plane will be under constant loading due to small changes in lift produced similar to the wing. A merit index that is particularly important for the horizontal tail-plane is the stiffness merit index  $M_E$  as a horizontal tail-plane as well as its elevators requires rigidity to maintain its shape in order to provide stabilising and control forces.

Similar to the design of the wings, the skin of the horizontal tail was assumed to take the force resultant of the bending moment. Unlike the wing design, a overall direct yield strength merit index  $M_\sigma$  was chosen rather than two separate tensile (equation 2.3) and compressive (equation 2.1) strength indices. Therefore  $M_\sigma$  is the lowest of both strength indices. This is because the most constraining loads on the horizontal tail-plane are caused by a one engine inoperative condition which could happen for either engine. Forces caused by bending moments can therefore act in either tension or compression in both the top and bottom skin. Therefore it was decided to have one material for both

the top and bottom material and also to choose a material based on overall direct yield strength. Having one material also reduces manufacturing complexity. The horizontal tail plane's spars are sized based on its ability to take shear loads, therefore a shear load yield strength merit index ( $M_\tau$ ) was also included.

The merit indices for carbon and glass fibre composites with an epoxy matrix were the only two considered as they are the only combinations with sufficient data from the composite materials handbook needed for future sizing. Specifically only unidirectional plies will be considered due to the laminate construction method used. The normalised results for the different merit indices can be seen in table 6.1.

Material	$M_f$	$M_E$	$M_\sigma$	$M_\tau$	$M_{Overall}$
Epoxy S Glass Fibre	1	0.920	0.478	1	0.849
Epoxy, Carbon Fibre	0.822	1	1	0.936	0.939

Table 6.1: Normalised merit indices

An Epoxy, carbon fibre UD tape can be seen to perform best in the overall material index and was therefore chosen. This lines up with the trend from similar aircraft as discussed previously.

This selection is however coarse as there are many different specific types of carbon fibre epoxy plies. Plies which fit the previously mentioned criterion of a unidirectional epoxy, carbon fibre tape from the composite materials handbook can be seen in table 6.2. As the skin and spars are responsible for carrying different (direct and shear loads respectively), it was decided to make them out of different composites. The overall and relevant constituent merit indices for the spar ad skin are shown in table 6.2 where  $M_{Skin}$  is the average of  $M_E$  and  $M_\sigma$  while  $M_{Spar}$  is the average of  $M_E$  and  $M_\tau$ . As previously mentioned, the skin material will be selected based on the overall yield strength, therefore the most constraining of the tensile or compressive strength was taken for evaluation. The performance of composites is also dependent on temperature, therefore the most constraining results of the following temperatures was taken for evaluation. Firstly, at a temperature of 24C (75F) which is the closest available data to standard atmospheric conditions and the highest temperature the material will experience. The second temperature considered was -54C (-65F) which is the closest data to lowest temperature of this design's mission profile which occurs during the cruise at 34000ft. The composite material handbook does not contain direct data on price and was therefore constant for all plies (taken at values given by Granta). Fatigue performance is explored in a later section [25].

Material	$M_E$	$M_\sigma$	$M_\tau$	$M_{Skin}$	$M_{Spar}$
HITEX 33 6k/E7K8 unidirectional tape	0.923	0.972	0.938	0.947	0.931
AS4 12k/E7K8 unidirectional tape .	0.929	0.987	1.000	0.958	0.964
Celion 12k/E7K8 unidirectional tape	1.000	1.000	0.711	1.000	0.856
AS4 12k/938 unidirectional tape	0.967	0.988	0.848	0.977	0.908
Celion 12k/938 unidirectional tape	0.969	0.962	0.905	0.965	0.937
T-300 15k/976 unidirectional tape	0.960	0.932	0.754	0.946	0.857

Table 6.2: Ply selection

From results in table 6.2, AS4 12k/E7K8 unidirectional tape was chosen for the spar and Celion 12k/E7K8 unidirectional tape for the skin as they had the highest value for their respective merit indices.

Due to the variability in the performance of composites, two knockdown factors were applied to values of mean strength. The first factor accounts for the greater variability in yield strength of composites from the mean compared to metals. A knockdown factor of 20% was taken to account for this [6]. The second knockdown factor is to account for fatigue known as a scatter factor. The scatter factor is a divisor which reduces assumed yield strength to account for fatigue instead of a decrease in the assumed lifetime as is the case for other materials. The scatter factor is given by equation 6.3 with the scale ( $\alpha$ ) and shape factor( $\beta$ ) coming from the materials experimental data weibull distribution. The following values were assumed for a reliability of R=0.9: Chi squared distribution  $\chi^2_{\gamma,2n_0} = 5.991$ , number of degrees of freedom n=1 . These constants represent a reliability of 90% with a confidence level of 95% in accordance with a B-basis reliability standard. Parameter  $\gamma$  represents the gamma function. The scatter factor divisor was calculated to be  $N_{F,sk} = 1.29$  and  $N_{F,sk} = 1.22$  for the skin and spar respectively [26].

$$N_F = \frac{\Gamma(\frac{(\beta_L+1)}{\beta_L})}{\left(\frac{-\ln(R)}{\chi^2_{\gamma,2n_0}}\right)^{\frac{1}{\beta_L}}} \quad (6.3)$$

The relevant shear and direct yield strengths of both plies can be calculated with these corrections and are given with the plies other properties in table 6.3.

Material	$\Sigma_{xx}$	$\Sigma_{xy}$	Thickness (m)	Density ( $kg/m^3$ )
AS4 12k/E7K8 unidirectional tape .	/	7.47E+07	0.000137	1590.000
Celion 12k/E7K8 unidirectional tape	9.08E+08	/	0.000279	1590.000

Table 6.3: Ply properties

## 6.3 Wingbox and Laminate Design

In order to handle the required loads, composite laminates are made up of unidirectional plies oriented in angles of 0, 90, 45 and -45°. Plies at an angle of 0 degrees handle the principle tensile and compressive forces acting on a composite structure while 90° plies carry transverse loads while reducing the poissons affect. Plies with a +45/-45 carry shear stress.

For this design, the skin is assumed to handle all the force resultant from bending moments. The resulting load per unit width ( $N_{xx}$ ) is given in equation 6.4 where  $h_{spar}$  is the larger of the two spar heights (front spar) and  $c$  is the wing box width. To the number of 0° plies was then calculated using equation 6.5 which was rounded up to the nearest whole number due to the discrete thickness of the plies and doubled to maintain symmetry.

$$N_{xx} = \frac{BM \cdot h_{spar}}{2c} \quad (6.4) \qquad n_0 = \frac{N_{xx}}{t\sigma_{xx}} \quad (6.5)$$

Even though the skin is not assumed to take any other loads, the 70/10% rule was used to size the number of plies for the other angles. The 70/10% rule involves adding 10% of the number of 0° plies for 90, 45 and -45° ply angles. These numbers are similarly rounded up but also doubled to maintain symmetrical plies. Due to the relatively small bending moments, the number of plies remains constant throughout the span due to rounding. This therefore gives the number of each angle ply as given in table 6.4.

$n_0$	$n_{90}$	$n_{+45}$	$n_{-45}$
2	2	2	2

Table 6.4: Number of skin plies in each orientation

The spars are assumed to take all of the shear force and therefore sized primarily by the number of 45 and -45 degree plies. Both the number of 45 and -45 plies were calculated with equation 6.6. Once again the 70/10% rule was applied for the 0 and 90 degree plies again rounding up and multiplying by two for symmetry.

$$n_{\pm 45} = \frac{N_{xy}}{\sigma_{xy} t} \quad (6.6)$$

The number of +45°/-45° as well as 0° and 90° plies required did change along the span. According to the initial strength calculations, plies are dropped in two pairs of two or four pairs of two due to the 70/10% rule and symmetry. It is, however, not optimal to drop many plies at the same time. Therefore plies will be dropped in two pairs of two and when there is a recommended drop of four plies it will be spread out into two drops of two pairs. The reason two pairs are dropped instead of just one pair is due to symmetry but also to maintain an orthotropic layup. An orthotropic layup is one which is symmetrical and is balanced meaning it has the same number of +45° as -45° plies. The orthotropic condition is required for future buckling analysis and must therefore be maintained. This therefore gives the number of plies for all spar sections as seen in Appendix O.

The properties of a laminate are dependent on the sequence in which the plies are positioned, known as its layup. Many combinations of layups are possible. From the following principles the initial skin layups were determined which can be seen in Appendix N.

- Layups should be symmetrical with any asymmetries placed as close to the axis of symmetry as possible.

- No more than two 0° or 90° plies should be placed next to each other as it results in delamination between the 0° ply and the 90° ply.
  - Plies should be dropped gradually while being interleaved with continuous plies.
  - Dropped plies near the end should not be near the edge of the laminate.
  - Should have the same number of +45° and -45° plies.

As the number of plies in the front and rear spars reduces along its length, considerations on how plies would be dropped were therefore made according to the previously stated rules. Figure 6.3 shows how plies were dropped for the front spar along their span. It can be seen that no more than two pairs of plies are dropped at a time, no plies are dropped next to each other but instead interleaved within other plies and the plies dropped near the edge are close to the centre line.

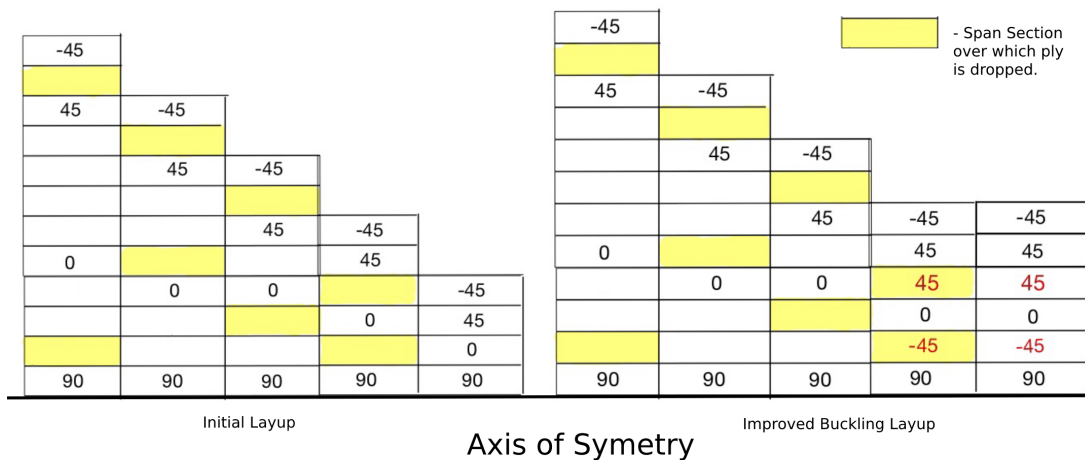


**Figure 6.3:** One symmetric half of front spar showing interleaved dropped plies for the original and buckling layup.

## 6.4 Buckling and Sandwich Structures

The next stage of laminate composite design is to design against buckling. As skin panels are assumed to take the loads resultant of bending moment the main buckling concern is compressive buckling given by equation 6.7. The skin also experiences shear flow due to torque and therefore must satisfy shear buckling condition given by equation 6.8 where  $k_s$  is given by graphs in Appendix K. The interaction of these buckling conditions yields the interaction curve which is the most constraining buckling condition and therefore the parameter sized for.

$$N_{x,cl}^{cr} = \frac{2\pi^2}{b^2} [(D_{11}D_{22})^{\frac{1}{2}})D_{12} + 2D_{66}] \quad (6.7)$$

$$N_{xy} = \frac{k_s \pi^2 \sqrt[4]{D_{11} D_{22}^3}}{b^2} \quad (6.8)$$

$$R_s^2 + R_c \leq 0.99, R_c = \frac{\sigma_c}{\sigma_{c,cr}}, R_s = \frac{\sigma_s}{\sigma_{s,cr}} \quad (6.9)$$

Equations 6.7 and 6.8 depend on  $D_{ij}$  values. These are values from the D twisting sub matrix of the laminates ABD matrix. The D matrix can be calculated using equation 6.10, where  $(\bar{Q}_{ij})_k$  is the stiffness matrix in global coordinates,  $t_k$  is the thickness of lamina k and  $\bar{z}_k$  the mid-plane coordinate of the lamina. The ABD matrix relates applied forces and moments to the strains and curvatures and is a function of the plies used and the layup. For efficiency, the ABD matrix of the skin as well as spars was calculated using the Laminate analysis program (LAP).

$$D_{ij} = \sum_{k=1}^n (\overline{Q_{ij}})_k t_k (\overline{z_k}^2 + \frac{1}{12} t_k^2) \quad (6.10)$$

From a research of similar aircraft it was found that sandwich structures are often used to improve the buckling properties of wing skin. Sandwich structures are composed of a light core material sandwiched between the already sized carbon fibre plies. These structures improve buckling properties according to equation 6.11 by increasing the thickness of the material  $t$  in a lighter way than adding extra carbon fibre plies. The parameter  $K$  is given by the graph in Appendix K. The use of sand which structures also improves the rigidity of a component. This is especially important for the horizontal tail-plane and elevators as it allows them to maintain their shape. This allows them to produce forces required for stability and control.

The study of similar aircraft shows that honeycomb structures made of aluminium and aramid (NOMEX) as well as some technical foams are used in commercial aircraft. The buckling stress of foams however is significantly affected by environmental conditions such as temperature changing. Foams were therefore not considered as this application involves large temperature variation and the buckling properties of foams will not be fully understood without experimental results. Aluminium and aramid honey comb structures were therefore evaluated for a stiffness merit index as given by equation 2.2. Stiffness is important to maximise buckling improvement as it allows for a larger core thickness before the core material buckles locally as given by equation 6.12. This greater thickness then allows for the core to better improve the sandwich structures buckling properties by increasing the  $D_{11}$  term in equation 6.11.

$$N_{cr} = K \frac{\pi^2}{b^2} D_{11} \quad (6.11)$$

$$\sigma_{cr} = \left( \frac{2}{3} E_f E_c \frac{t}{h} \right)^{1/2} \quad (6.12)$$

The honeycomb structure with the highest merit index was found to be Aluminium 3003 honeycomb (0.083) which was therefore chosen. With a material chosen, the maximum thickness of the core before buckling was calculated using equation 6.12 to be 9.4mm.

The overall skin buckling condition (interaction curve) can be met with unlimited combinations of the following changes: increasing Sandwich core height  $h_c$ , increasing number of stringers therefore reducing stringer pitch  $b$ , increasing number of ribs therefore reducing rib spacing  $a$  (influences  $k_s$ ) and the adding of extra carbon fibre plies. To optimise for mass, an estimation of the mass was made for the following quantities: mass of two stringers  $m_s$  (one for each skin, design of which is explored in later sections), mass of adding an extra ply to the entire skin  $m_p$  and the mass of adding a unit thickness of the honey comb structure  $m_{HC}$ . The ratio of the stringer mass to both the extra ply mass and the mass of a unit thickness honeycomb was found to be  $\frac{m_s}{m_p} = 0.0107$  and  $\frac{m_s}{m_{HC}} = 0.000307$  respectively. These values imply that if one stringer is removed and the buckling condition can still be met by adding either 0.0107 plies or 0.307mm of honey comb thickness, then there is a weight saving. The ratio  $\frac{m_s}{m_p}$  is less than two therefore the solution is impossible as the thickness of plies is constant. The number of plies was therefore kept constant. The rib spacing  $a$  was also kept constant as shear buckling is the less constraining condition and changing rib spacing within reasonable values had little to no effect on the overall buckling conditions. A value four times the stringer spacing was therefore taken initially as it is the minimum ratio required by the equation. Honeycomb thickness  $t_H$  was therefore the only parameter adjusted in the following methodology in order to minimise mass.

- The number of stringers and therefore stringer pitch  $b$  was changed to (9 stringers,  $b = 0.151$ ) such that interaction curve buckling condition was met with the original layup with no sandwich structure.
- One by one, a stringer was removed and the thickness of foam needed to satisfy the buckling condition was found.
- If the increase in thickness of the foam was less than 0.307mm then there was a weight saving and the process was continued.
- If the thickness increase required was greater than 0.307mm or if the total honeycomb thickness was greater than the local buckling thickness 9.4mm, the previous solution which passed the buckling condition was taken.
- The thickness of the honey comb structure was then reduced until the interaction curve equalled to 0.99 to minimise mass.

This process resulted in a minimum mass solution of decrease in one stringer and a honey comb thickness of 0.000918m. This solution was reached because a stringer-less solution required a honeycomb thickness greater than the local buckling thickness.

Buckling of the spars is defined purely by shear buckling as given in equation 6.8 (In the context of the spars  $b$  represents the the spar height). As previously discussed, sandwich structures are not common in commercial aircraft spars. Therefore plies were added to the spars such that buckling condition stress is equal to the ultimate load stress

experienced at the most constraining spar section. To satisfy buckling constraints, two plies were added to the front spar while one was added to the rear spar. As the end of each spar was the most constraining section, plies were "added" by simply extending ply pairs which were previously dropped in strength calculations to the most constraining spar section. This results in a lesser weight than adding a ply throughout the entire span. It has the additional benefit of having plies dropped near end, be further away from the edge of the laminate. The final layup of the most constraining spar section can be seen in figure (6.3).

## 6.5 Stringer, Rib and Spar Cap Design

As previously mentioned, the skin of the wing box is assumed to carry all forces resultant of the bending moment with the number of plies sized accordingly. The stringers therefore do not need to be sized for any particular load. They however were assumed to act as a boundary condition for buckling calculations and therefore must simply be of reasonable dimensions and layup to uphold this condition. For simplicity's sake, many of the dimensions of the vertical tail-plane stringer were therefore taken. The stringer thickness was determined by assuming a basic layup shown in figure (6.4). This layup was decided on as it is the minimal mass combination which has plies in all directions allowing the stringer to act as a boundary condition.

top	Material	Thickness	Angle
1	AS4 12K/E7K8 UNIDIRECTIONAL TAPE	0.0001372	90
2	AS4 12K/E7K8 UNIDIRECTIONAL TAPE	0.0001372	45
3	AS4 12K/E7K8 UNIDIRECTIONAL TAPE	0.0001372	0
4	AS4 12K/E7K8 UNIDIRECTIONAL TAPE	0.0001372	-45
-- MID - PLANE --			
Total Thickness : nominal 0.0010976 actual 0.0010976			

Figure 6.4: Minimum mass/thickness basic layup

An initial value for rib spacing  $a$  was used in the buckling process. The actual rib spacing required is determined by equation 4.13 and assumed to remain constant. As the stringer has already been sized the farrar efficiency was found using figure L.1 to be  $F=0.5$ . This yielded a rib spacing of  $s=0.226$  giving 26 ribs in the semi span.

The rib thickness was then sized according to the crushing force using equations 6.13 and 6.14.  $T$  represents the equivalent thickness which in this design is taken as the actual thickness as the skin. This is because the stringers are not assumed to take any loads. These equations are a function of Young's modulus which unlike metal, is a function of a composites layup. Therefore before calculating the thickness, the basic layup in figure 6.4 was chosen as it satisfies the 70/10/10% rule in the minimum thickness. This is important to minimise weight because the rib thicknesses eventually calculated are as low as 1mm which is less than even the chosen four minimum plies. AS4 12k/E7K8 unidirectional tape was chosen as the material for both the stringer and ribs as it has a lower ply thickness than Celion 12k/E7K8 therefore giving a smaller mass while still meeting the minimum ply requirement of the 70/10% rule. The rib thicknesses required were therefore calculated with equations 6.13 and 6.14 along the span and then rounded up to multiples of 0.0010976m to maintain the same Young's modulus. Ribs of the following thickness seen in figure 6.5 are therefore required.

$$F = \frac{M^2 s h_c T c}{2 E I^2} \quad (6.13)$$

$$\frac{F}{t_r c} = 3.62 E \left( \frac{t_r}{h_c} \right)^2 \quad (6.14)$$

To check the ribs designed are not susceptible to buckling, the compressive buckling equation 6.7 seen previously was used. However all four different rib thicknesses passes the buckling criterion and therefore required no adjustments. The new rib spacing was then checked against the skin and spar buckling conditions to ensure they were still met.

As the skin is assumed to take all force resulting from the bending moments, the spar cap is not required to carry any loads. It is simply used to connect the spars to the skin. Therefore the same basic minimum thickness layup in Figure 6.3 will join the spar and skins as seen in Figure 6.6. As explored later in joints and fittings, it was decided to adhesively bond composite components of the tail-plane. Therefore a double lap joint with an overlap of three times the thickness of the spar will be used. This is the minimum overlap which ensures that failure occurs in the joined materials rather than the joint [27].

Important parameters of the horizontal tail-plane are represented diagrammatically in Figure 6.8.

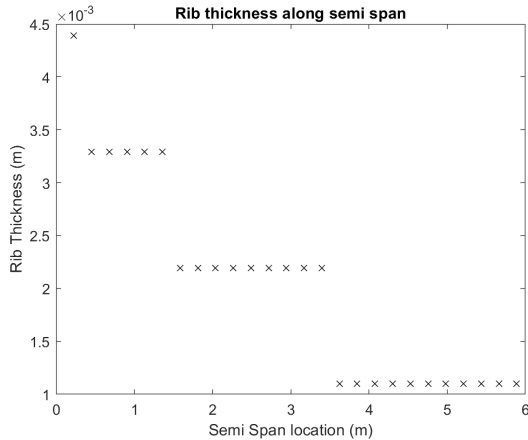


Figure 6.5: Graph of the thickness of all ribs along the semi-span.

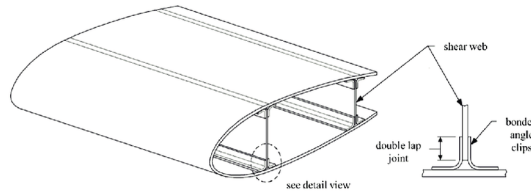


Figure 6.6: Composite spar cap diagram [28]

## 6.6 D Cell Design

From similar aircraft it was found that some aircraft have metal leading edges. The main benefit of which are the following : Leading edges are susceptible to bird strike. In a composite this would lead to micro-cracks and delamination which may not be evident on the surface. Aluminium also provides better properties against erosion from water and sand [29]. Having the entire D-cell made of metal also provides greater span to adhesive bond the horizontal tail plane to the vertical tail-plane. This is preferential to bolting the composite structure to the metal tail plane as is explored later in fittings. Preventing many of these issues also reduces the amount of inspections and part replacements required therefore making it more economic. Due to all these factors, it was decided to construct the D-cell out of aluminium.

Following the methodology explained 5.6, the thickness of the D-Cell could be calculated. To find the number of pseudo ribs and the associated thickness, an optimisation on the weight must be performed. By increasing the number of ribs, the thickness of the D-cell will decrease but the total weight of the ribs will increase. The optimisation can be seen in figure 6.7.

Following an economic logic and taking into account that it is almost the minimum of the Total Weight function, the number of pseudo-ribs chosen is 6. The thickness of the associated D-Cell is 4mm.

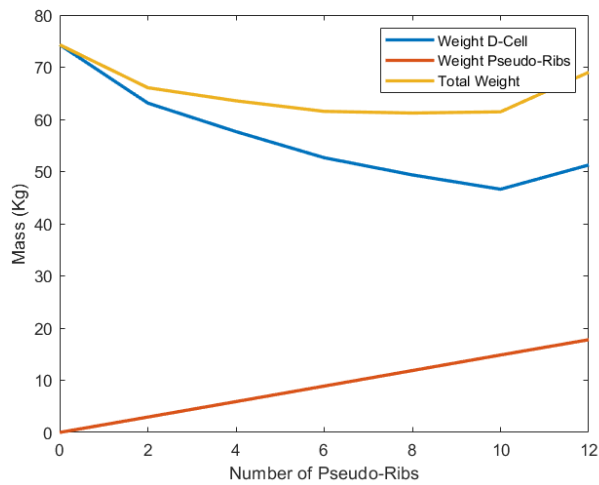


Figure 6.7: HT D-Cell Mass Optimisation

## 6.7 Horizontal Tail Layout

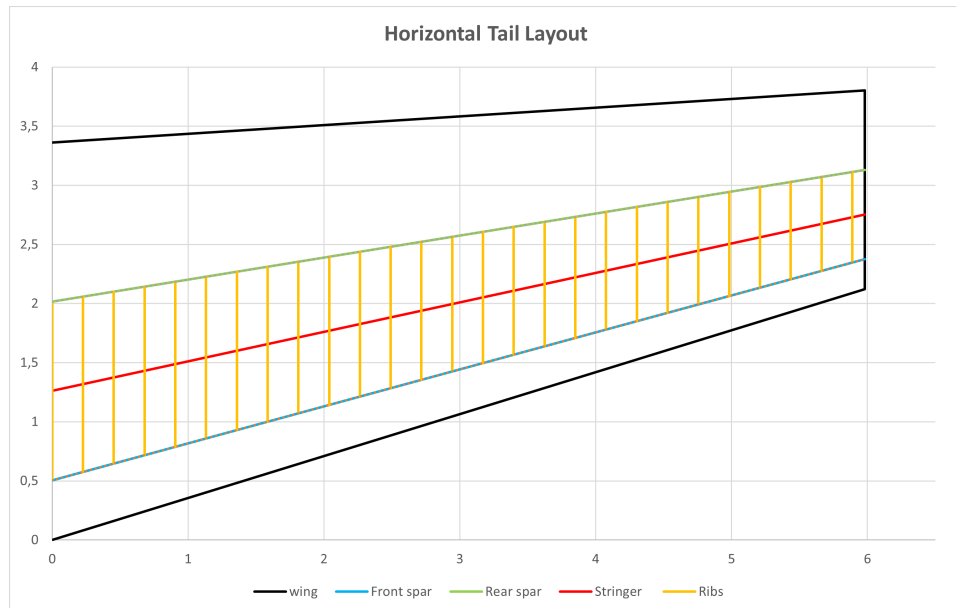


Figure 6.8: Horizontal Tail Layout

# Chapter 7

## Secondary Structure Design

### 7.1 Cutouts

A study of similar aircraft shows a variety of possible cutouts with some required for practical, lightening or comfort reasons. As this a preliminary sizing, only the main doors and windows were sized in detail as is appropriate for a first iteration.

A window is considered a small cutout as it does not cut any light frames. The size of a window is a trade off between the extra reinforcement weight and passenger enjoyment. Such a trade off is beyond the scope of this initial sizing, therefore a reasonable value informed by similar aircraft was chosen. A radius of 0.1625m was chosen which equals 65% of the light frame spacing. A circular shape was taken for simplicity of calculations even though it only found in a small proportion of similar aircraft.

While a window does not cut a light frame, it will cut nine stringers. This necessitates an increase in the skin thickness at these panels. When the stringers are cut at the frame neighbouring the window, there is a lag in the axial load carried by the stringers as seen in figure 7.1. This is most constraining at the rib where the stringer is cut. At the rib this load is instead transferred through the skin as a shear force [30] instead of being carried by the surrounding stringers. To account for this, the thickness of the skin is increased in the panels with cut stringers, to the effective skin thickness as given by equation 4.21. This yields the thickness in the window panels of  $t_e = 0.00569m$  which is linearly increased to in neighbouring skin panels also.

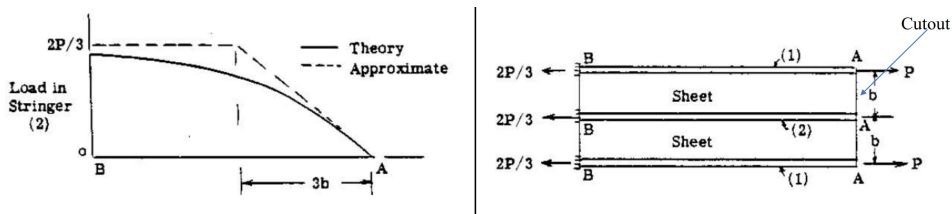


Figure 7.1: Graph showing change in axial load of stringers after one is cut

When a round cutout is made in a panel, the maximum edge stress increases to three times the stress in the panel previously [30]. This would significantly exceed the fuselage material yield strength, therefore extra material must be added to support the cutout. According to Mansfield [31], material can be added around a circular cutout according to equation 7.1 such that the stress distribution is the same as if there was no cutout. This is known as a neutral hole. Using this formula yields an reinforcement area required of  $A = 0.00138m^2$  giving a uniform minimum reinforcement width of  $w_{min} = 0.00135m$  radially around the hole. This extra material will be added in the form of a doubler due to its manufacturing simplicity compared to alternative reinforcement methods.

$$A = \frac{Rt}{1 - \nu} \quad (7.1)$$

$$\sigma_{cr} = \left(\frac{K}{K_0}\right) K_{71005} E \left(\frac{t_e}{b}\right)^2 \quad (7.2)$$

The cutout also affects the buckling properties according to equation 7.2. Parameters  $K_{71005}$  and  $(\frac{K}{K_0})$  are empirical values given by graphs in appendix (L). The parameter b is the height of the window panel which was set at  $b=0.334m$  the smallest value which both larger than the window diameter and was a multiple of stringer spacing. Additionally, the buckling performance of the panel and its doubler are also a function of the doubler width (w) and doubler height which includes the skin thickness (h). Therefore combinations of doubler width and height were found in order to find the combination which minimises mass. The following constraints were placed on the combinations of doubler width and height: Doubler width must be greater than the minimum doubler width required to counter edge stress, double thickness must not exceed the distance between the fuselage skin and cabin (0.07m) doubler width must be greater than the diameter of a typical rivet (0.003175m) (source) and the doubler width can't exceed the data available in the  $\frac{K}{K_0}$  graph in appendix (L). The fuselage skin dimensions were also rounded up to tenths of a millimetre while doubler dimensions were rounded up to whole millimetres for manufacturing and cost considerations. The minimum mass combination which followed these constraints was therefore found to be a doubler width of  $w = 0.004m$ , a doubler thickness of  $h = 0.007m$  giving the final dimensions seen in figure M.2.

A regular door is considered a large cutout as its width as a type 1 emergency exit (defined by FAR25) must be at least 0.6096m (24 in) which is larger than the light frame spacing of 0.5m. To account for the cutting of a light frame, the door will be reinforced by extra heavy frames on the boundary of the door cutout, known as a picture frame. After adding the picture frame, the shear flow in panels surrounding the cutout are shown in figure M.1. The shear flow in the panels prior to making the cutout is q while  $Q'_H$ ,  $Q'_L$  and  $Q'_{HL}$  are the given by equation 7.3

$$q_H = \frac{qH_2}{(H_1 + H_3)}, q_L = \frac{qL_2}{(L_1 + L_3)}, q_{HL} = \frac{qHL_2}{(L_1 + L_3)} \quad (7.3)$$

The panel thicknesses ( $t_H$ ,  $t_L$  and  $t_{HL}$ ) required of these new shear flows were then calculated and summarised in table 7.1. In the case of the  $t_L$  panels the thickness required is less than the normal skin thickness, the previously calculated fuselage skin thickness\* was therefore taken. Once again, skin thickness in panels surrounding the neighbouring panels, will be increased linearly from the original skin thickness to the new required thicknesses. This methodology assumes the most constraining scenario of a failure in the door meaning it carries no load. The door however will also have structural members to provide extra load paths when closed to improve the structural integrity.

$t_H$ (m)	$t_L$ (m)	$t_{HL}$ (m)
0.00426	0.00310*	0.00548

Table 7.1: Table of new skin thicknesses surrounding door cutout.

Although a detailed design for other cutouts was not completed, a qualitative description of all other cutouts was decided. The emergency doors planned in the conceptual design are compromised of two type 3 and two type 4 emergency doors. The minimum width of which are 0.508m and 0.4826m respectively. Type three doors would therefore require a picture frame designed in a similar manner to the main door as they exceed the light frame spacing. Type 4 doors however can be reinforced with just a bear strap as they are smaller than the 0.5m light frame spacing. A bear strap is a large sheet of reinforcing metal which is attached around a door. The planes cargo door will also likely cut a light frame and therefore necessitate a picture frame. Lightening holes in the ribs and spars in the wings and empennage would be sized as small cutouts to reduce weight. Other cutouts (such as inspection holes, ventral doors, etc) required for practical reasons are likely small cutouts and would be sized in future iterations.

## 7.2 Joints and fittings

Aeroplanes are made of many constituent parts which require assembly with joints and fittings. The most important joint is the wing root joint. The following are the most commonly used wing root joints.

- Tension Bolts - The main benefits of this option is its lesser manufacturing fitness requirements as well as it being easy to assemble or remove. However as bolts are less effective at carrying tension loads than shear loads ([32]), more bolts are needed therefore resulting in a weight penalty.

- Lug Fittings - This method involves joining multiple lugs on the fuselage and wings with bolts. Lug fittings are similarly easy to assemble and require less manufacturing fitness. They also require less structural wing depth and are therefore optimal for aircraft with thin wings. As the wing is only reinforced by a few lugs, heavy reinforcement of these lugs is required leading to a heavy weight penalty.
- Splice Plates- Splice plates involve loading bolts in shear, this results in fewer required bolts than other alternatives and therefore a weight saving. Splice plates are also more reliable as it is a continuous joint meaning if one bolt fails, the loads can easily be carried by other bolts. The main downsides of splice plates is that they are more expensive and require a larger wing depth than other fitting methods.

It was decided to choose the splice plate wing root joint due to its fail safe design as well as weight savings which are the two most important factors in a regional airliner. This design's wing is likely sufficiently thick as shown by the wide spread use by similar aircraft with similar wing constructions. The higher initial cost will also be outweighed by the weight savings in the long term.

Other major joints on an aircraft can be seen in figure M.3 and are as follows: Joints between sections of fuselage, attachment of fuselage skin and wing skin to their respective frames, attachment of empennage to fuselage as well as the attachment of ribs and stringers.

Bolts, rivets and adhesive bonding are the most commonly used fasteners in similar aircraft. Bolts are very effective in shear, are easily disassembled and are therefore good for maintenance reasons. Bolts are typically used in joining large scale structures. It was therefore decided to join sections of the fuselages together with bolts as well as to attach the vertical tail to the fuselage. Bolts are also used to attach the wing root joint as previously mentioned.

Rivets are lighter than bolts as well as cheaper and easier to produce. They are however permanent fastenings and are poor at joining thick materials due to poor tensile strength relative to shear strength. Rivets were therefore decided to fasten the fuselage, wing and vertical tail-plane skins to their frames. They will also be used to attach stringers to the skin of the wing and vertical tail-plane while ribs will be attached using a bracket joined by rivets. Doublers on the window panels will also be attached using rivets due to its low cost.

Adhesive bonding unlike bolts and rivets does not require making holes in the material being joined. This prevents high stress concentration around the joining area especially in continuous fibre composites [14] such as this design's. This therefore makes it the ideal solution for joining composite components as is the case in similar aircraft such as the airbus A380 and Boeing 787. It was therefore decided to attach the horizontal tail to the vertical tail with adhesive bonding. As this fitting is between a composite and a metal component, it will be joined in a stepped lap joint as it provides the highest high shear strength as seen in figure (graph from slides) without imposing a difficult and costly manufacturing requirement on the metal vertical tail. The spars and skin will be joined with adhesive bonding of the spar caps as previously explored.

In terms of regulatory airworthiness requirements, FAR 25 requires a fitting factor of at least 1.15 for the fitting itself, the means of attachment as well as the bearing on the joined members [1]. Unless the joints are made using approved practices with sufficient test data to prove a lesser fitting factor. This process would likely happen in future iterations.

## 7.3 Engine Mounts

This design has two fuselage mounted podded engines. The weight of the engines will be supported by two supports between the nacelle and two heavy frames as seen in figure J.1. To transfer the thrust of the engine to the aircraft, an additional thrust link will connect from one heavy frame support on the nacelle to the other heavy frame. During operation, the engine geometry will vary due to thermal expansion. The attachment must therefore be statically determinant, allowing for expansion or contraction of the engine. The rear attachment structure therefore will have a degree of freedom to move in the axial direction by using a roller bearing.

Engine mounts must be sized for a set of ultimate loads which are a function of the engine thrust as given in Appendix J.1. The engine mount must also be sized for the case of an emergency landing. Due to this design's fuselage mounted engines, the mounts must be sized to handle the full inertial loads associated with landing as given by FAR25 in Appendix J.1. This is in contrast to wing mounted engines which are designed to fail under emergency conditions. It is anticipated that the engine mounting mass required would therefore be heavier for this design than other similar aircraft however such sizing would be completed in future iterations.

# Chapter 8

## Detailed Design Concept

The objective of this chapter is to design a part that is subjected to stress while optimising its mass and cost. Throughout the design process, it must always be ensured that the part meets the specifications imposed on it.

### 8.1 Mission

The component is a part of the flap extension system. The component is made of an aluminium 6082-T6. The objective of the part is to withstand a vertical LIMIT force of 4.5kN and not to deform more than one millimeter in the direction of the force. Moreover A safety factor imposes an ULTIM effort.  $ULTIM\ LOAD = 1.5 * LIMIT\ LOAD = 6.75\ kN$ . The final objective is the obtain the best Load/Mass ratio  $\eta$ .

$$\eta = \frac{Load}{Mass} \quad (8.1)$$

Thus, the part must support the ultimate load without breaking and be as light as possible to obtain the best ratio. The beginning of the study begins with an aluminum plate 6.35mm thick and whose dimensions are as shown in Appendix D.

### 8.2 Assumptions and Method

The material used in the design of this part is 6082-T6 aluminium alloy. This material is widely used in aeronautics and has the following properties (only the properties of interest are listed in the following table):

Young Modulus	Possion Ratio	Density	Yield Stress
69GPa	0.33	2.7g/cm <sup>3</sup>	270MPa

**Table 8.1:** Properties of Aluminium 6082-T6 [33]

Because the stress analysis is going to be done on Abaqus to make an FEA, a coherent mesh for the part need to be found. To achieve a good mesh it was important to find a compromise in the number of elements and the speed of calculation. Thus, trying to reach the maximum number of nodes allowed by Abaqus (250,000 nodes) while obtaining acceptable computation times, 2mm elements was chosen. In addition, the mesh elements have been chosen to be 3D hexahedral not structured because there is no load normal to the plane.

As far as loads are concerned, there are two important ones: the ultimate load and the limit load described above. Both should be tested and it should be checked that in the case of the ultimate load, the stresses felt by the part are lower than the yield stress. In the case of the limit load, the displacement in the direction of the load must be less than 1mm.

To perform the analysis, boundary conditions are required. In the problem two boundary conditions are imposed

on the two holes on the left and right of the part. The central hole is used to transmit the loads. The first hole on the left has all its movements blocked as well as its rotations, except for the rotation in the plane, it is a pivot link. For the second hole on the right, it is almost the same thing except that a displacement is made free (according to h axis in the reference frame of the part, see D.1) to create a rolling support.

Now that all the elements of the analysis have been described, a method must be found to find the best possible part respecting all the constraints. To do this two strategies will take place. The first one is to perform the analysis on the unmodified part, to find the low-constraint areas and to cut the part accordingly. By iterating this strategy, the part will become less and less heavy while respecting the constraints. The second method is to use the topological optimisation offered by Abaqus. In this case the strategy is different. The constraints to be respected are described to Abaqus and the software takes care of finding the best geometry to face them. It will therefore be interesting to compare these two methods to determine which part will be the best.

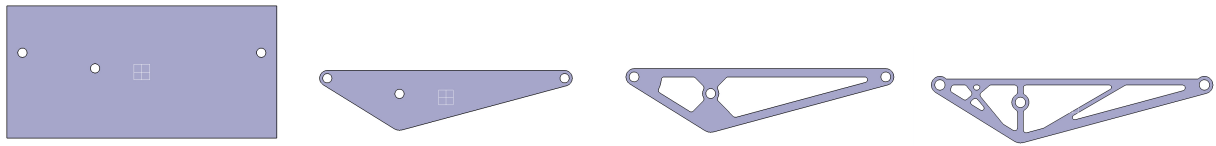


Figure 8.1: Evolution of geometry : V1, V2, V3, V7

## 8.3 Results of Iterations

First, the results of the iterative method will be studied. At the end of the 7th iteration, the resulting part was suitable because it was the part with the lowest mass that respected the deformation characteristic and had a maximum stress below the yield stress. The following table shows the evolution of stress and strain at each iteration for the different cases (UL= Ultimate Load and LL=Limit Load).

Iteration	2	3	4	5	6	7
Mass [kg]	0.583	0.319	0.303	0.243	0.268	0.271
Stress (UL case) [MPa]	126	182	194	255	263	250
Strain (LL case) [mm]	-0.387	-0.736	-0.754	-1.106	-0.991	-0.945

Table 8.2: Results of iterations

Thus, following this study, iteration 7 was chosen to be the one selected by this methodology. The following illustrations are the results of the FEA for the 7th iteration.

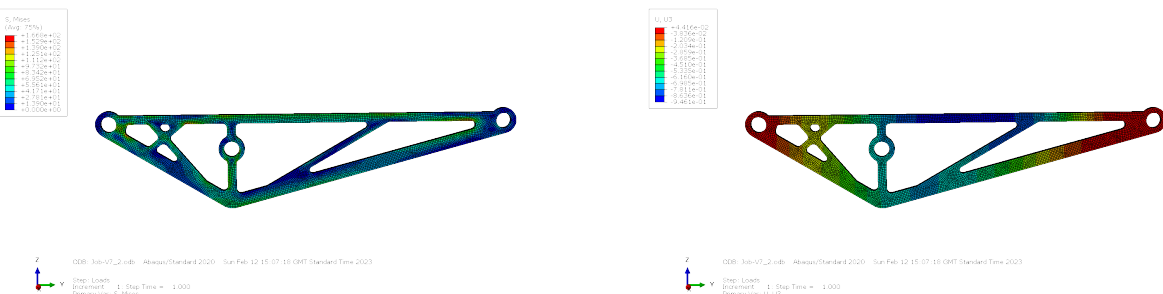


Figure 8.2: V7 : Stress and Strain | Limit Load

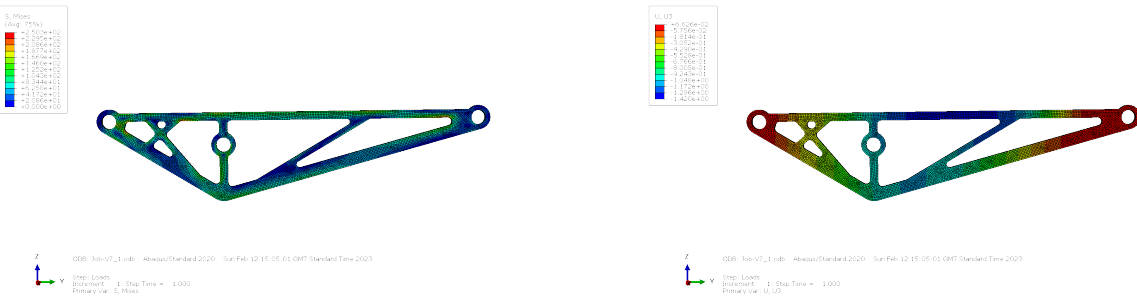


Figure 8.3: V7 : Stress and Strain | Ultimate Load

## 8.4 Topology Optimization

Topological optimization is a process which makes it possible to obtain the most adequate geometry of a part subjected to efforts and having constraints to be respected. To perform a topological optimization the basic model of the aluminum plate was given to Abaqus and the loads and boundary conditions were described to it. Then an objective function was declared, the strain energy. The goal was to minimize this energy as much as possible. The constraint that came to stop this minimization was the conservation of a certain percentage of the initial volume of the part. Following this optimization Abaqus returns geometries. Thus, two geometries gave physically correct results for Volume >15% and Volume >20%. If a too large volume was kept, then the part was far too heavy compared to its competitor in the previous methodology. If a smaller volume was decided to be reached, then the results returned by Abaqus were no longer physically true (Elements of the part were not connected, hole impossible to make in manufacturing,...). The next figure illustrates the two geometries obtained.

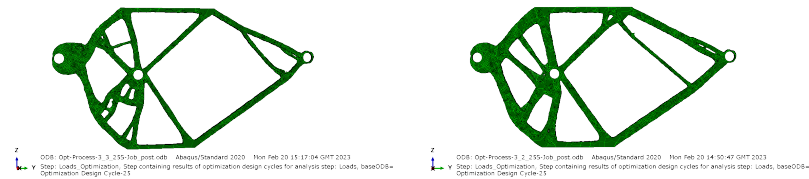


Figure 8.4: Geometry for V&gt;15% and V&gt;20%

Once the geometries have been obtained, there is a need of rebuilding real part from them. Indeed, some manufacturing constraints need to be follow. It also applies to the pieces created in the previous methodology. The constraints are the following:

- Minimum radius for each radius is 4mm
- Minimum distance of a free edge is 3.5mm
- Minimum strut width is 3.5mm
- 30mm diameter safe area around each holes

Thus two parts were obtained and can be seen in [E.1](#)

Finally, they have been tested back to be compared with the other results. Results are shown in [E.3](#) and [E.2](#). The results are summarised in the following table.

Geometry	V>20%	V>15%
Mass [kg]	0.701	0.55
Stress (UL case) [MPa]	88	109
Strain (LL case) [mm]	-0.081	-0.122

Table 8.3: Results of iterations

It can be seen that the parts given by the topological optimisation are often heavier and oversized. Indeed, the sudden maximum stresses are very far from the elastic limit of the material. However, this optimisation gave a geometry

that allowed to support the forces much better. So it will be interesting to mix the two different methodologies to find a lighter part as in the iterative method but with the geometry of the topological optimisation.

## 8.5 Final Design

### 8.5.1 Use of both methodologies

Therefore, by looking at the two previous methodologies and trying to take the best of each, a final part was designed. It takes the geometry of the topological optimization and through iterative work, the volume of the part has been reduced to make it lighter. This part is the final design. The following table and [F](#) present these characteristics.

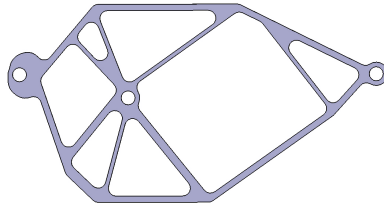


**Figure 8.5:** Final Design

Mass [kg]	Max Von Mises (UL cases) [MPa]	Max Strain (LL case) [mm]
0.32	173	-0.388

**Table 8.4:** Final Design characteristics

### 8.5.2 Buckling analysis

To be sure of the solution, a buckle analysis was also performed. To be sure of the solution, a buckle analysis was also carried out. It is important to check that the structure will not buckle at a load lower than the ultimate load. Buckling is the consequence of instability in the structure, so it is very hard to predict and that is why it is need to be avoid. The first five buckling modes can be seen in [G](#).

Mode	1	2	3	4	5
Eigenvalue	-1.132	1.498	-1.839	2.4269	-2.728

**Table 8.5:** Summary of buckling modes

Negative eigenvalues are not of interest because they correspond to loads that would be applied in the opposite direction to that imposed by the problem. Then, the smallest of the eigenvalues is taken into consideration. In this case, it is 1.342. This means that the loads experienced by the part must be multiplied by 1.342 for it to buckle. This is a good thing because if the smallest eigenvalue had been smaller than 1 it would have indicated that the part would have buckled before reaching its maximum load. This is not the case here[\[34\]](#). The buckling analysis confirms that this part is correctly designed.

Best of each Methodology	Mass [kg]	Max Von Mises (UL case) [MPa]	Max Strain (LL case) [mm]
7th iteration	0.271	250	-0.945
Optimization topology ( V>15%)	0.55	109	-0.122
Final design	0.32	173	-0.388

**Table 8.6:** Summary of each methodology best results

# Chapter 9

## Conclusion

### 9.1 Mass Estimations

In order to evaluate this preliminary sizing, the mass of all designed structural elements was calculated. These values can be seen in table 9.1 along with mass estimates from the conceptual design. These estimates from the conceptual design however also include non-structural weight.

Component	Conceptual Design Mass Estimate (kg)	Preliminary Design Mass Estimate (kg)
Fuselage	5180.1	4671.2
Wing	3192.8	5352.0
Vertical Tail	355.5	971.7
Horizontal Tail	533.6, (319.8)	272.6

Table 9.1: Mass Table

### 9.2 Discussion of the fuselage

The results obtained for the light frames and heavy frames of the engines and t-tail are rather consistent. The results for the wings are not at all consistent. The method used is surely the cause: the point of application of the loads are made only in one point and the sizing of the frames is done from the maximum of the WISE curves whereas the maximum is obtained for only one precise point. A structure that distributes the loads in several points of application like the beam structure that exists between the fuselage and the wings will distribute the loads much better and therefore obtain a lower maximum and hopefully more consistent values.

### 9.3 Discussion of the wings

The values found for the wing are for the most part in line with what was found in the similar aircraft section. For example, the ribs spacing found is almost the same as that of the similar aircraft. In addition, a number of dimensions that were taken from the similar aircraft gave consistent and satisfactory results, such as the stringer dimensions for the stringer panel. So in general the design of the wings is quite consistent with what is done in the industry. However, there are some issues that would require further iterations on the project. Among the problems encountered, the most important are :

- The stress in the ribs is too high. It is therefore necessary to change the material of the ribs or to increase their thickness.
- The total mass of the wing is twice as large as estimated in the conceptual design. Furthermore the mass found by taking into account only the structural elements is supposed to represent only 50% of the wing mass. Again a new iteration would be necessary to recalculate the centre of gravity.

To solve this mass problem, a lighter material could be considered for the wing structure. Cutting holes could also be used on the wing structure to make it lighter while maintaining its mechanical properties.

## 9.4 Discussion of the empennage

From table 9.1 it can be seen that the mass of the horizontal tail-plane is less than weight budget given in the conceptual design. Non-structural weights in the horizontal tail-plane are likely small as there are not many systems in the empennage. This design's total weight is therefore indeed below the weight budget given. The initial weight budget was however given assuming the horizontal tail was made of aluminium which accounts for the large difference. The value in brackets is an estimate of the weight of a composite tailplane based on the assumption that composite wing and empennage are approximately 40% lighter than ones made of aluminium [35]. This value is close indicating reasonable sizing.

The other most important result is the number of ribs. The values obtained were greater than expected even though from similar aircraft horizontal tail planes tend to have a smaller rib spacing. This is likely due to the poor farrar efficiency factor of the stringer. This could be improved with a more in depth design of the stringers used which in this first iteration were only sized to uphold the necessary boundary conditions.

For the vertical tail, the vast majority of the values found are consistent with what has been observed for other aircraft. The main problem is the same as for the wing, the mass is too important. It should have been lighter because the fuselage mounted engines produce less moment. A composite vertical tail could help solve this problem but further iterations will definitely be needed to solve it.

## 9.5 Overall Conclusion

Through this study it was observed that some elements were heavier than initially planned. These are the wings and the empennage. These results are probably due to the fact that the aircraft's engines are mounted on the fuselage at the rear of the aircraft. Furthermore, the equations used to calculate the masses during the conceptual design may have had their limits, particularly in the case of the vertical tail, which is significantly larger than the average. On the other hand, the fuselage is lighter than calculated. Again this is certainly a consequence of the engines mounted at the rear of the aircraft. This is because there is less weight on the wings and therefore the fuselage has to support the wings. It is therefore naturally lighter. Further iterations would be needed to converge.

# Bibliography

- [1] 'Federal Aviation Authority'. *FAR 25.335*. 1990.
- [2] *Sandwich Structures and Cores*. <https://www.addcomposites.com/post/sandwich-structures-and-cores>. 2021.
- [3] A.Haszler A.Heinz. "Recent development in aluminium alloys for aerospace applications". In: *Materials Science and Engineering* (2000).
- [4] Federal Aviation Authority. *FAR25.841 - Pressurized cabins*. 1996.
- [5] Michael Chun-Yung Niu. *Airframe Structural Design*. 1988.
- [6] D.Yang L.Iannucci. "AERO60002 Aerospace Vehicle Design Lecture Notes". In: (2023).
- [7] Houston. G Quinn. D Murphy. A Bron. F. "Wing Panel Design with Novel Skin-Buckling Containment Features". In: *Journal of Aircraft* (2016).
- [8] Embraer. "ERJ145XR Airport Planing Manual". In: (). URL: <https://www.embraercommercialaviation.com/commercial-jets/erj145xr/>.
- [9] *CRJ1000 datasheet*. Bombardier. 2020.
- [10] Michael Chun-Yung Niu. *Airframe Stress Analysis and Sizing*. 1997.
- [11] Mike Badrocke. *Airbus A320 Cutaway Drawing*. URL: <https://conceptbunny.com/airbus-a320/>.
- [12] CompositeUK. *Use of composite materials in Aerospace*. <https://compositesuk.co.uk/composite-materials/applications/aerospace/#:~:text=Carbon%2Dfibre%20reinforced%20polymer%20and,%2C%20tail%20surfaces%2C%20and%20doors.h>.
- [13] Malo Ginot Bruno Castanié Christophe Bouvet. *Review of composite sandwich structure in aeronautic applications*. 2. 2020.
- [14] Kailun Zheng Zhusheng Shi Hongwei Zhao Jiangjing Xi. "A review on solid riveting techniques in aircraft assembling". In: (2020).
- [15] N.J Marston Z.W Li. *Update of New Zealand's Atmospheric Corrosivity Map (Part 2)*. Tech. rep. BRANZ, 2015.
- [16] *Ansys Granta EduPack*. Ansys. 2023.
- [17] *MatWeb: Online Materials Information Ressource*. <https://www.matweb.com/>. 2023.
- [18] Frisch B Grantham E Pigamo A Rosenblatt F Appenzeller B Babalola A. *Conceptual Design Report*. 2022.
- [19] Lars Adriaan KRAKERS. *Parametric fuselage design*. 2009.
- [20] Daqing Yang. "Fuselage Sturctural Design". In: *AER060002 - Airframe Design*. Imperial College London, London, 2023.
- [21] E F Bruhn. *Analysis and Design of Flight Vehicle Structures*. 2nd ed. USA, Jacobs Publishing Inc, 1973.
- [22] Engineering Sciences Data Unit. "Buckling Stress Coefficients for Curved Plates in Shear". In: (1958).
- [23] E. Levis D. Yang L.Iannucci. *Preliminary Design 1.1*. Imperial College London. 2023. URL: <https://imperial.cloud.panopto.eu/Panopto/Pages/Viewer.aspx?id=c505405f-7fc8-4668-bab4-af9300c6d450>.
- [24] D.Yang L.Iannucci. "AERO60002 Aerospace Vehicle Design Lecture Notes, Chapter 3 Lifting Surface Design". In: (2023).
- [25] Departmement of Defense USA. *Composite Materials Handbook*. 2. 2022.
- [26] Dvir Elmalich Yuval Freed. "A new study on scatter factors in fatigue testing of composite materials". In: (2020).

- [27] Dan Kay. *How Much Overlap Should I Use for a Lap Joint in Brazing?* URL: <https://www.industrialheating.com/blogs/14-industrial-heating-experts-speak-blog/post/88260-how-much-overlap-should-i-use-for-a-lap-joint-in-brazing#:~:text=3T\%20to\%204T\%20is\%20perfectly,through\%20longer\%20and\%20longer\%20joints>.
- [28] *Generic-bonded wing spar construction.* URL: [https://www.researchgate.net/figure/Generic-bonded-wing-spar-construction-3\\_fig2\\_350703516](https://www.researchgate.net/figure/Generic-bonded-wing-spar-construction-3_fig2_350703516).
- [29] *Why are the leading edges on the Boeing 787 made from aluminum?* 2017. URL: <https://aviation.stackexchange.com/questions/35441/why-are-the-leading-edges-on-the-boeing-787-made-from-aluminum>.
- [30] D. Yang. *1. Secondary Structures - Cutouts.* Imperial College London. 2023.
- [31] Murat Tolga Ozkan. *Determination of theoretical stress concentration factor for circular/elliptical holes with reinforcement using analytical, finite element method and artificial neural network techniques.*
- [32] D. Yang. *1. Secondary Structure - Joints and Fitting.* Imperial College London. 2023.
- [33] *6082-T6 Aluminum ressources.* <https://www.makeitfrom.com/material-properties/6082-T6-Aluminum/>. 2020.
- [34] *Eigenvalue Buckling Analysis.* [https://www.clear.rice.edu/mech517/WB16/lectures\\_trainee/Mechanical\\_Intro\\_16\\_0\\_AppA\\_Buckling.pdf#:~:text=Eigenvalue%20or%20linear%20buckling%20analysis%20predicts%20the%20theoretical,Euler%20column%20will%20match%20the%20classical%20Euler%20solution..](https://www.clear.rice.edu/mech517/WB16/lectures_trainee/Mechanical_Intro_16_0_AppA_Buckling.pdf#:~:text=Eigenvalue%20or%20linear%20buckling%20analysis%20predicts%20the%20theoretical,Euler%20column%20will%20match%20the%20classical%20Euler%20solution..) 2015.
- [35] Joaquim R. R. A. Martins Graeme J. Kennedy. "A Comparison of Metallic and Composite Aircraft Wings Using Aerostructural Design Optimization". 2012.

## Appendix A

# Graphs Stringer Panel

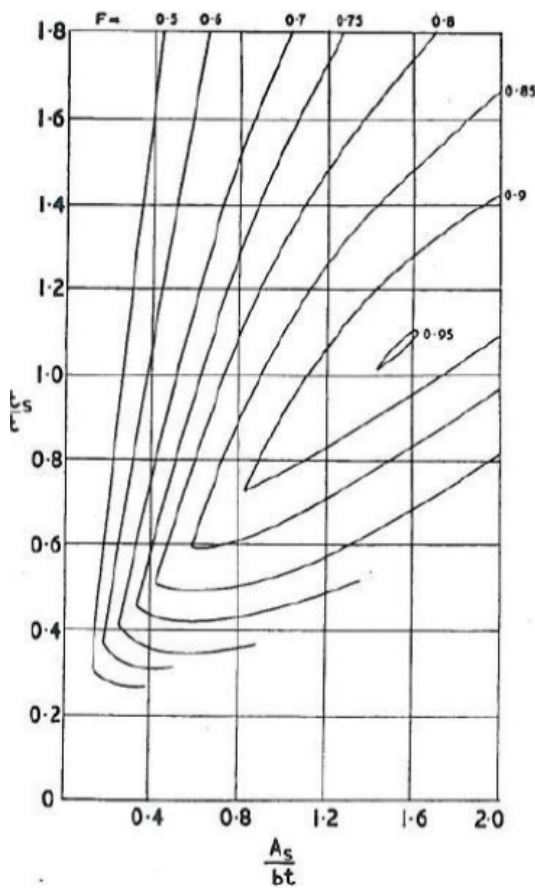


Figure A.1: Farrar Efficiency

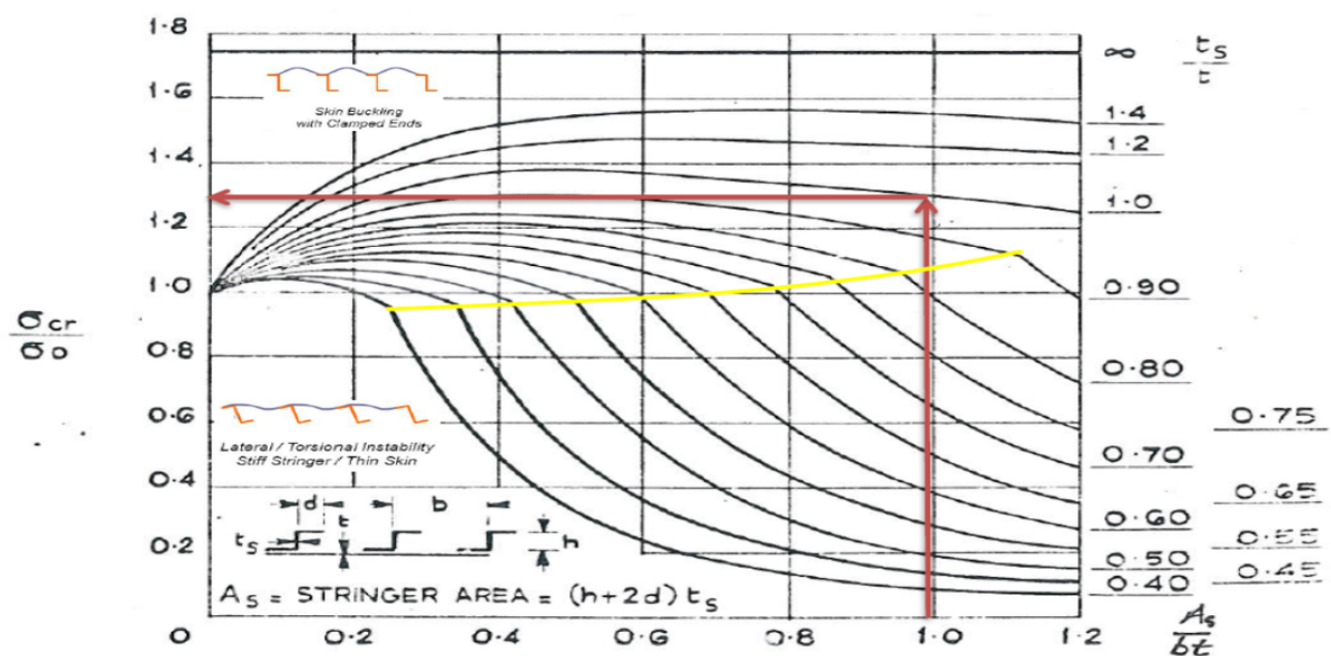


Figure A.2: Initial Buckling Stress of flat panels with Z Section stringers

## Appendix B

# Curved Plate

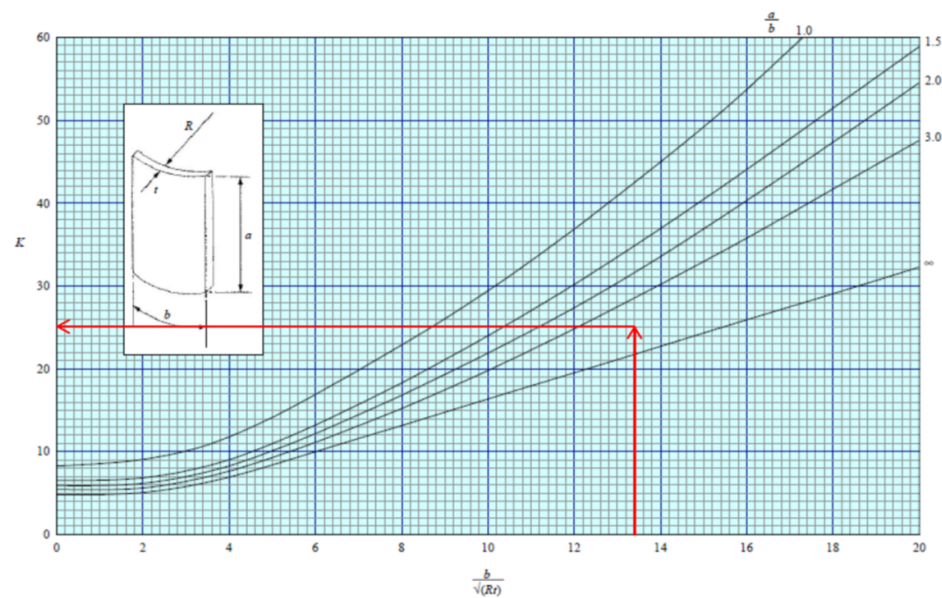


FIGURE 1 BUCKLING STRESS COEFFICIENTS FOR CURVED PLATES IN SHEAR ( $a/b \geq 1$ )

**Figure B.1:** Buckling stress Coefficient for curved plates in shear

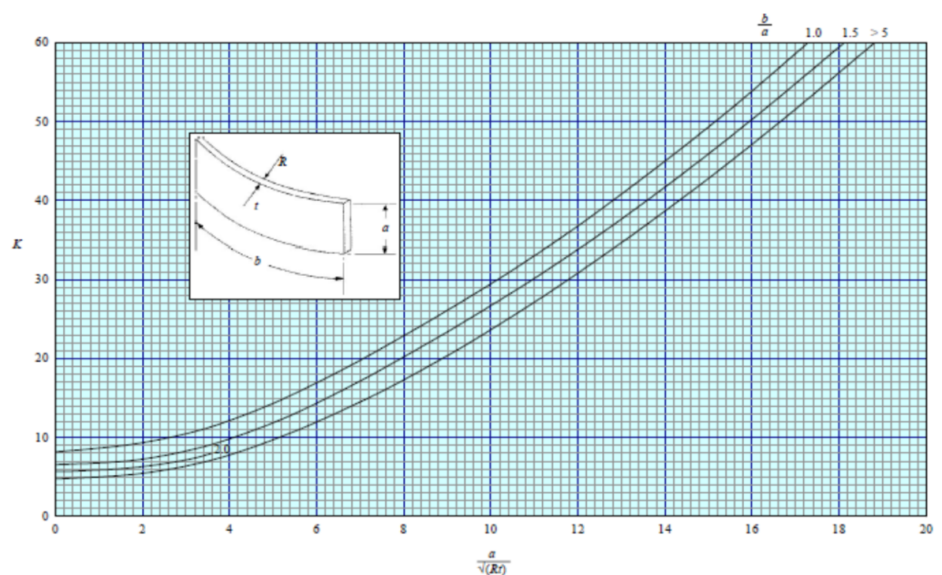
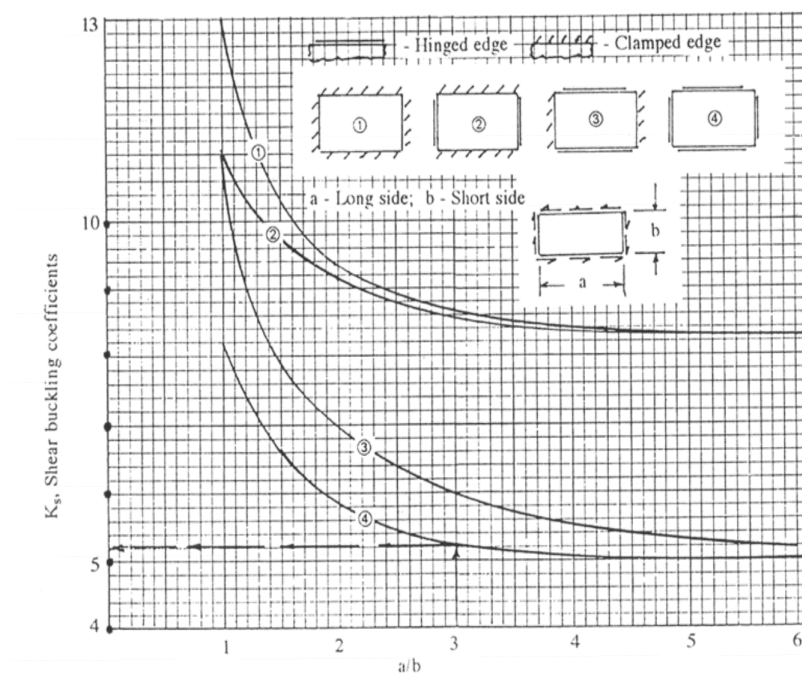


FIGURE 1 BUCKLING STRESS COEFFICIENTS FOR CURVED PLATES IN SHEAR ( $b/a \geq 1$ )

**Figure B.2:** Buckling stress Coefficient for curved plates in shear

## Appendix C

# Shear Buckling Coefficient



**Figure C.1:** Shear Buckling Coefficeint

## Appendix D

# Starting Plate Dimensions

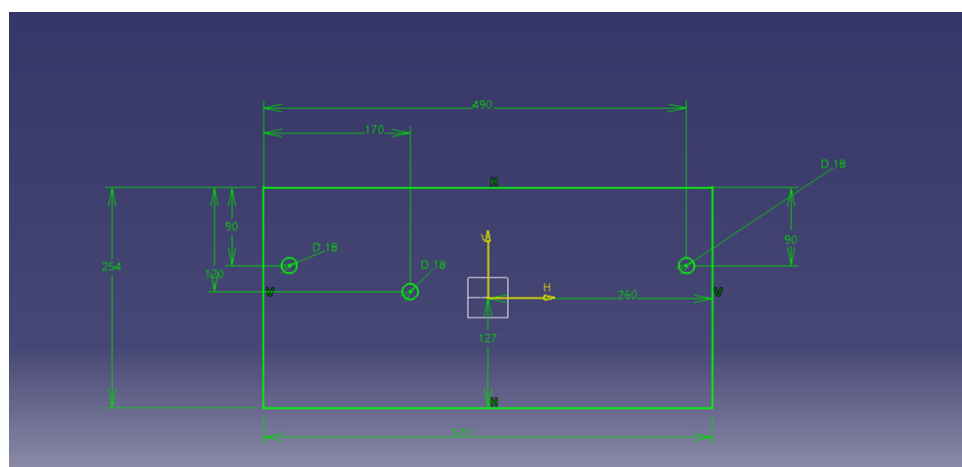
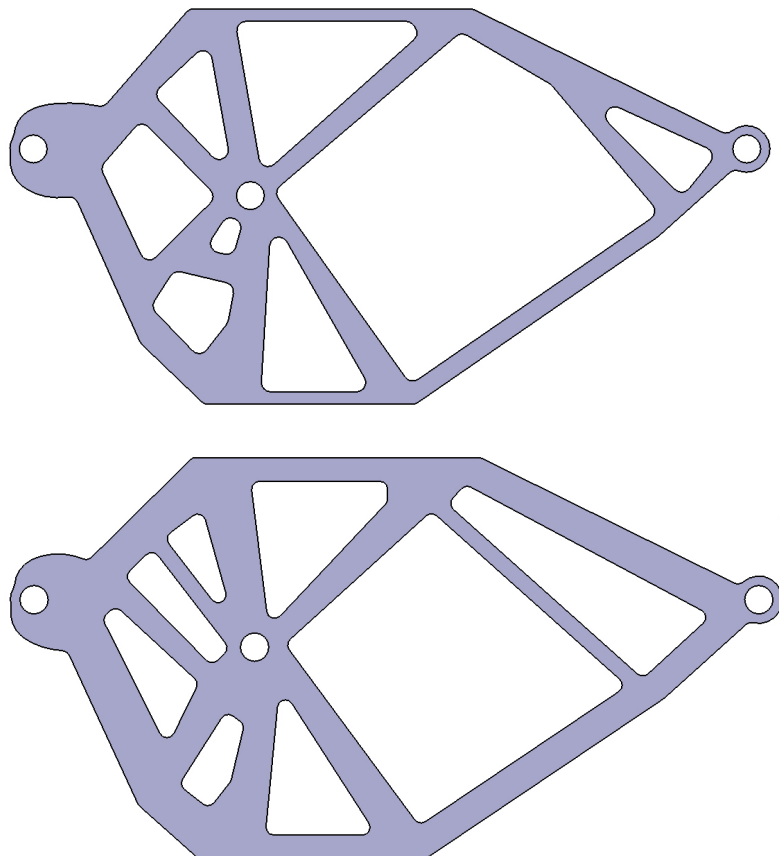


Figure D.1: Starting plate dimensions

## Appendix E

# Topology Optimisation Designs



**Figure E.1:** Part Build from previous geometries for  $V>15\%$  and  $V>20\%$

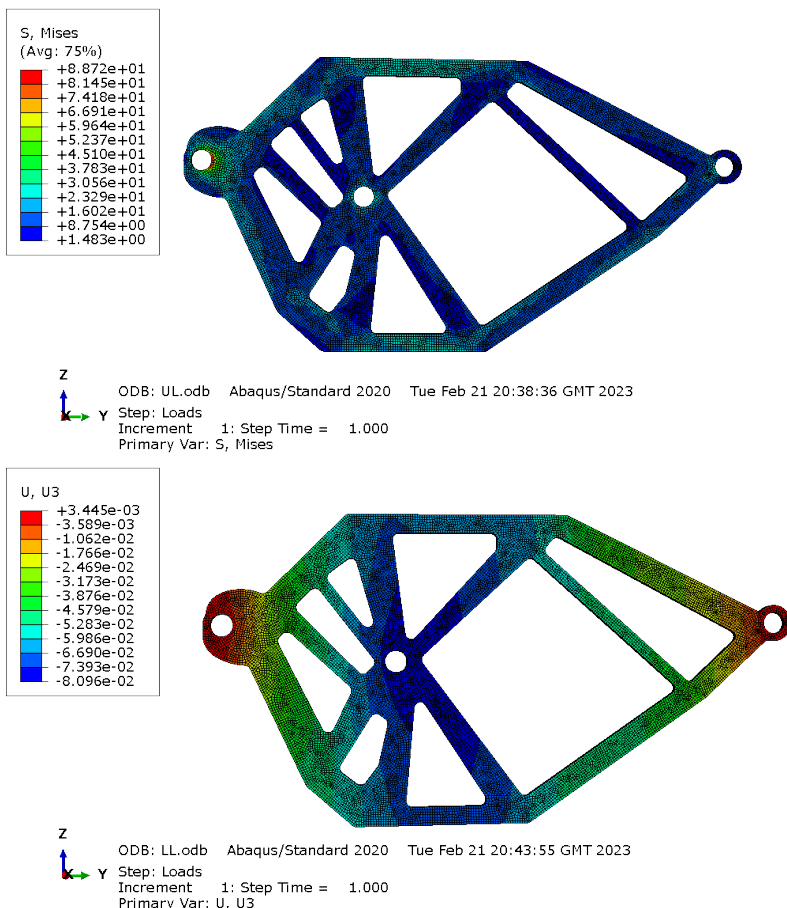
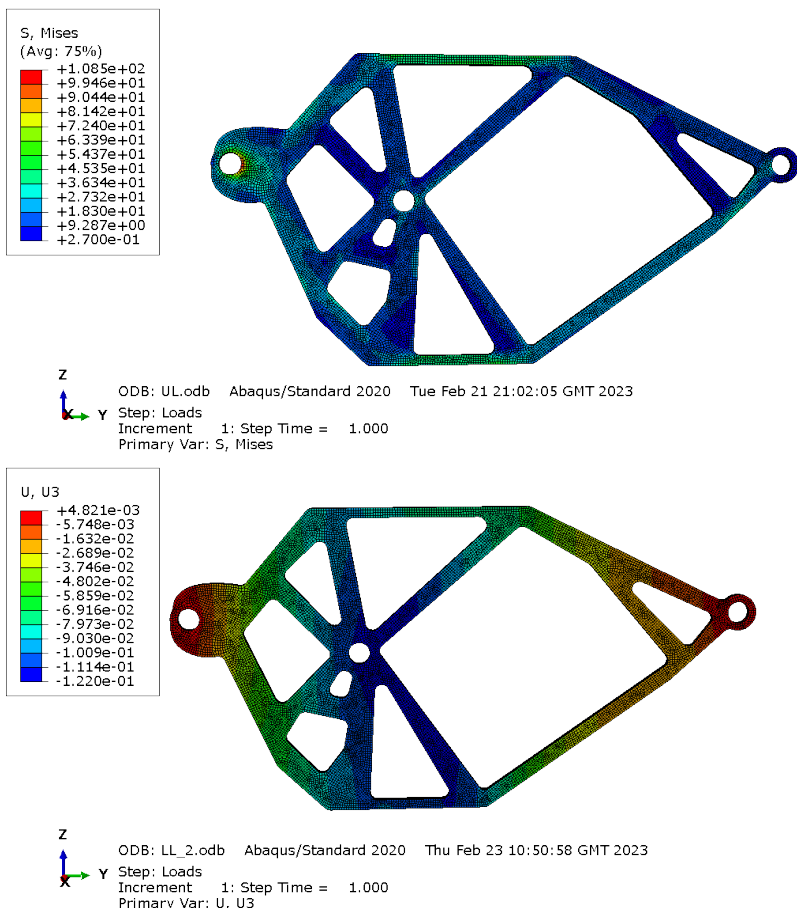


Figure E.2: V>20% : Stress (UL case) and Strain (LL case)



**Figure E.3:** V>15% : Stress (UL case) and Strain (LL case)

## Appendix F

# Final Design

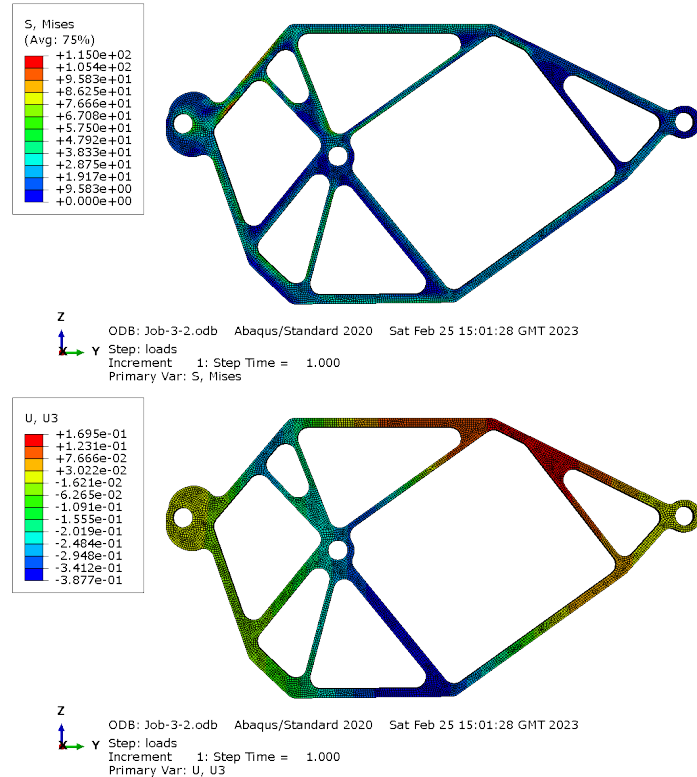


**Figure F.1:** Final Design : Stress and Strain | Limit Load

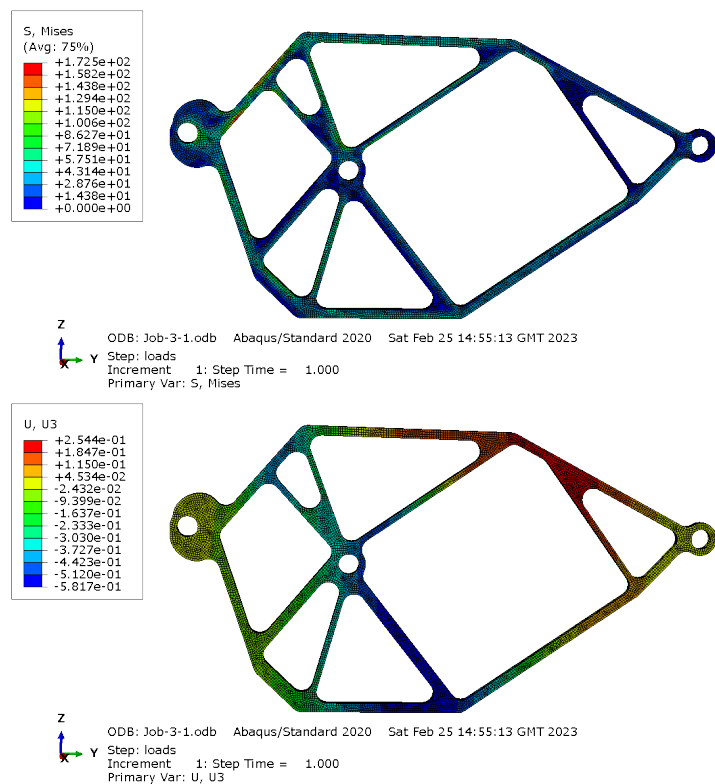
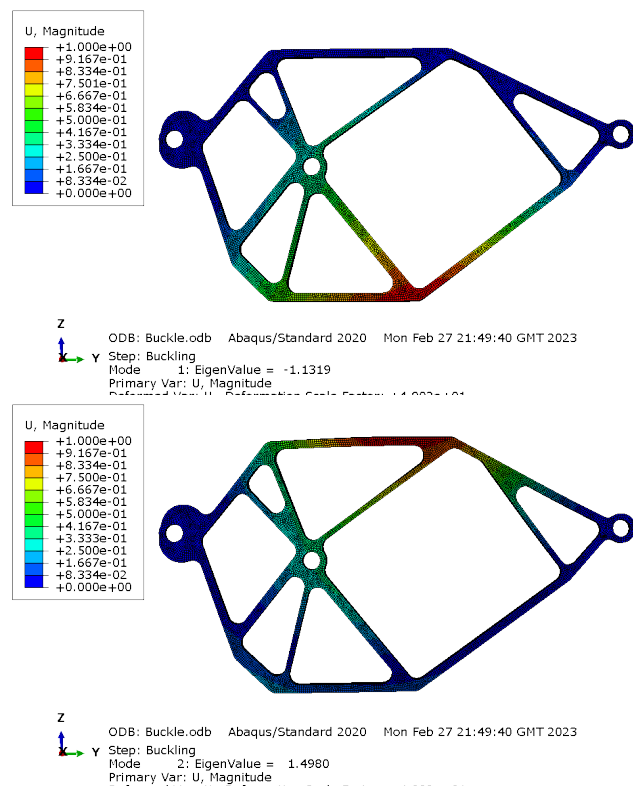


Figure F.2: Final Design : Stress and Strain | Ultimate Load

## Appendix G

# Final Design Buckling Analysis



**Figure G.1:** Buckling Mode 1 and 2

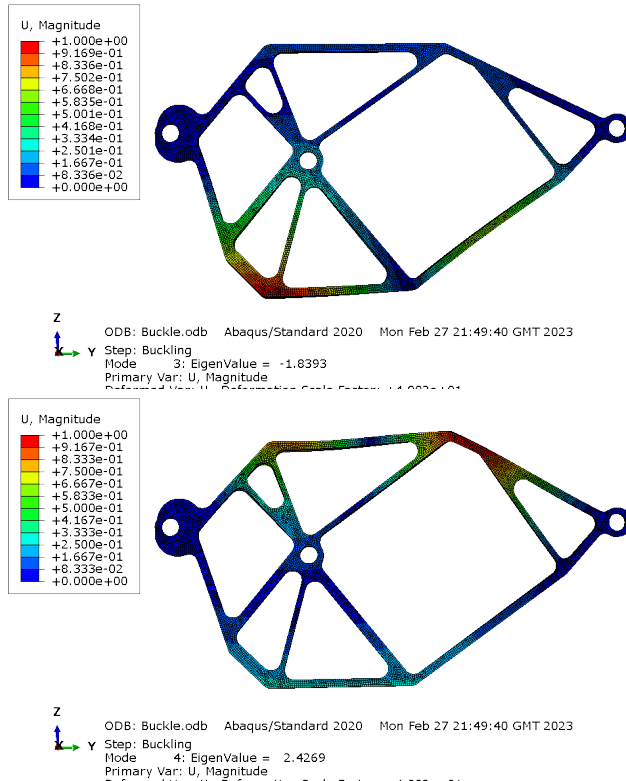


**Figure G.2:** Buckling Mode 3 and 4

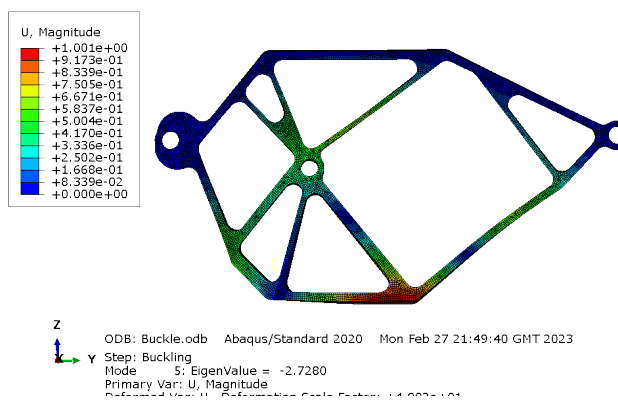


**Figure G.3:** Buckling Mode 5

## Appendix H

# Final Design Dimensions

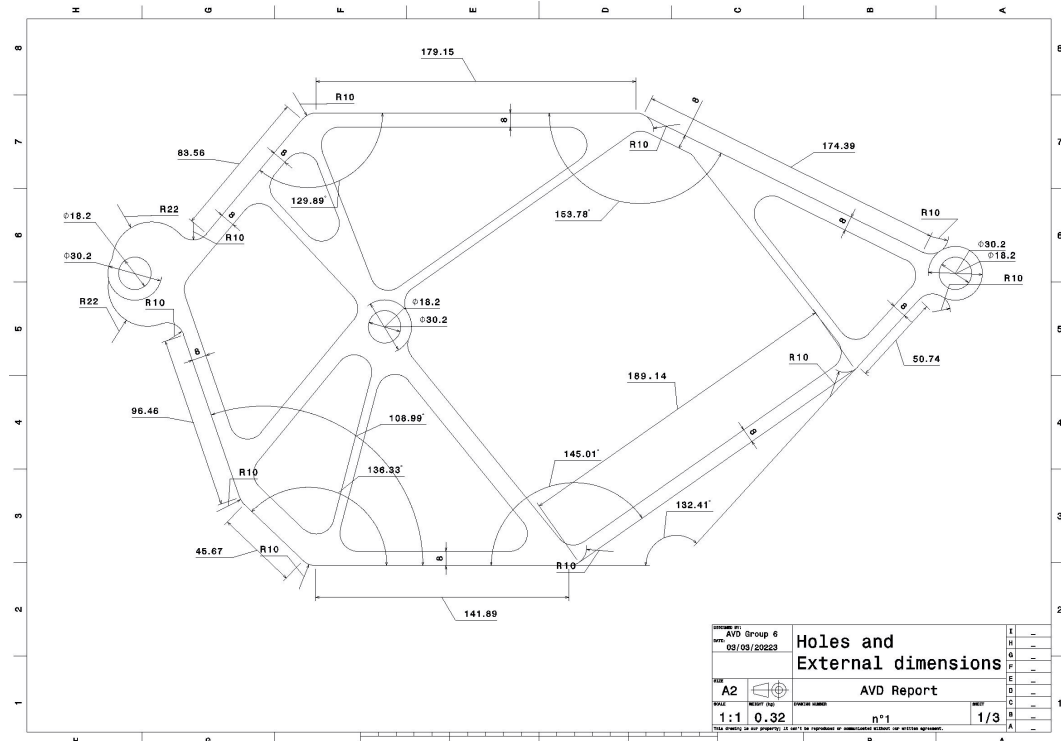
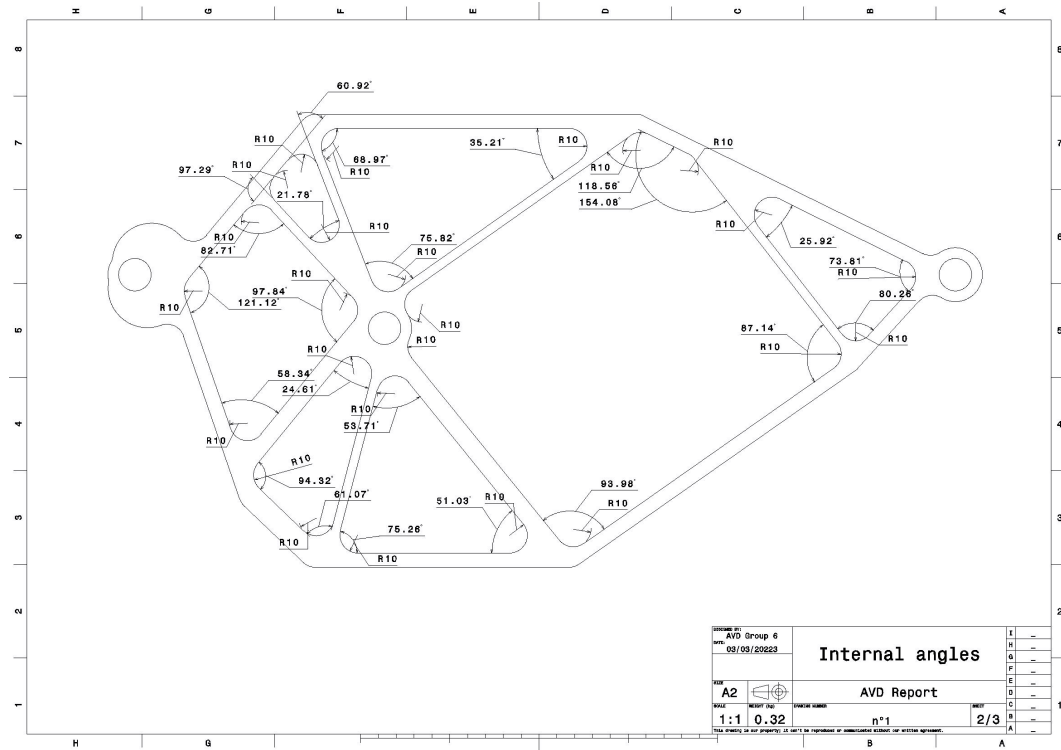
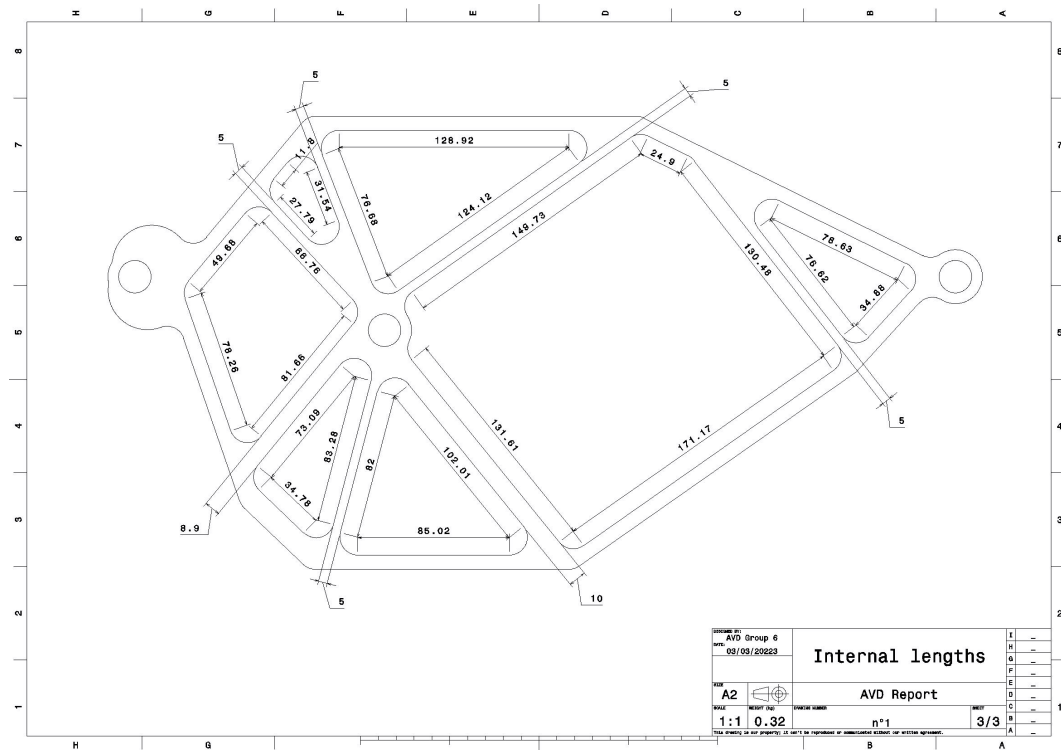


Figure H.1: Final Design External Dimensions



**Figure H.2:** Final Design Internal Angles



**Figure H.3:** Final Design Internal Lengths

## Appendix I

### Fuselage

Parameter	$15t^2(mm^2)$	$I_{y\text{skin}}mm^4$	$A_s(mm^2)$	$I_{y\text{stringer}}(mm^4)$	$\text{Total}I_y(mm^4)$	$\text{Maxstress}(MPa)$
Value	3.75	$2.79 \times 10^{-8}$	162	$1.21 \times 10^{10}$	$1.23 \times 10^{10}$	493.2

**Table I.1:** A Table Showing the initial Stringer and Skin Bending Geometries

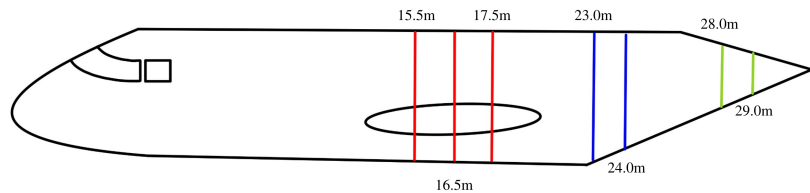


**Figure I.1:** Drawing of all heavy frames location.

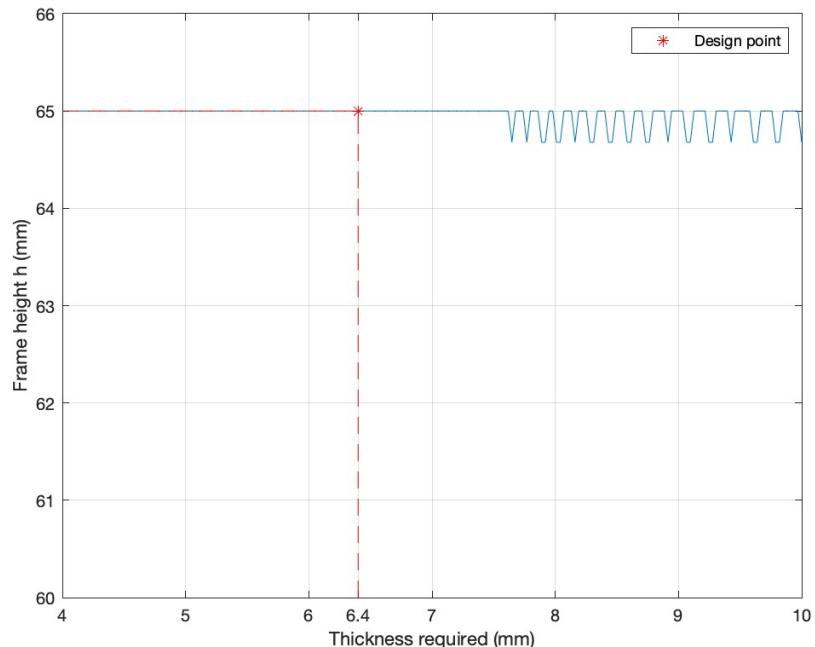


**Figure I.2:** Evolution of optimal height with required thickness for engines heavy frames.

Stringer Height(mm)	Stringer thickness (mm)	Flange Length(mm)	Stringer Area (mm <sup>2</sup> )	ts/t	A <sub>s</sub> /bt	F
32.5	1.2	22	88.92	0.387097	0.24577392	C
32.5	1.25	22	92.50	0.403226	0.255669	C
32.5	1.3	22	96.07	0.419355	0.26553644	C
32.5	2.55	22.5	184.62	0.822581	0.51028768	C
32.5	2.6	22.5	187.98	0.83871	0.51957468	C
32.5	2.65	22.5	191.33	0.854839	0.52883404	C
32.5	3.95	23	278.87	1.274194	0.77079365	C
32.5	4	23	282.00	1.290323	0.77944494	C
32.5	4.05	23	285.12	1.306452	0.78806859	C
31.5	1.55	22	112.22	0.5	0.31017486	C
31.5	1.6	22	115.68	0.516129	0.31973826	C
31.5	2.9	22.5	205.03	0.935484	0.5667007	C
31.5	2.95	22.5	208.27	0.951613	0.57565602	C
31.5	3	22.5	211.50	0.967742	0.58458371	C
31.5	4.35	23	299.28	1.403226	0.82720667	C
31.5	4.4	23	302.28	1.419355	0.83549864	C

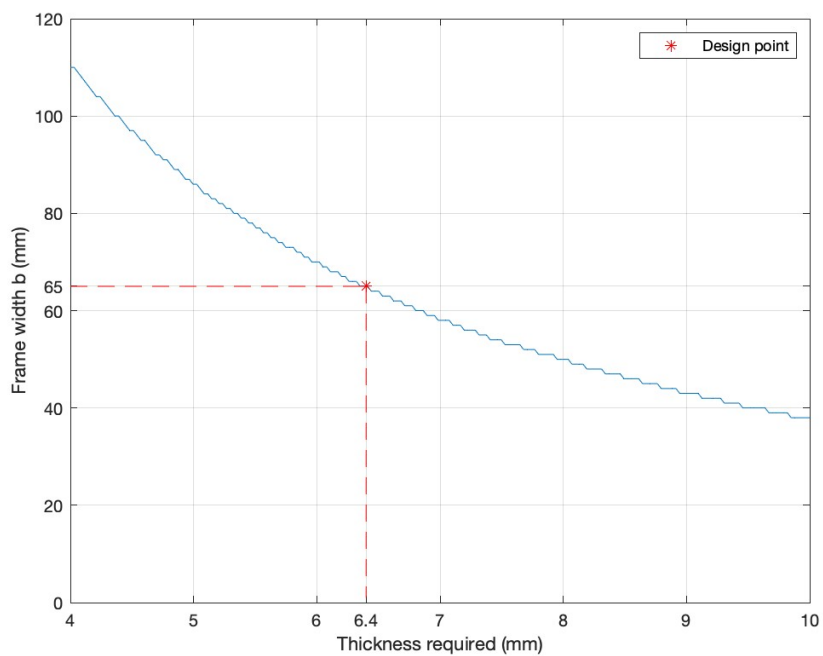


**Figure I.3:** Evolution of optimal width with required thickness for engines heavy frames.

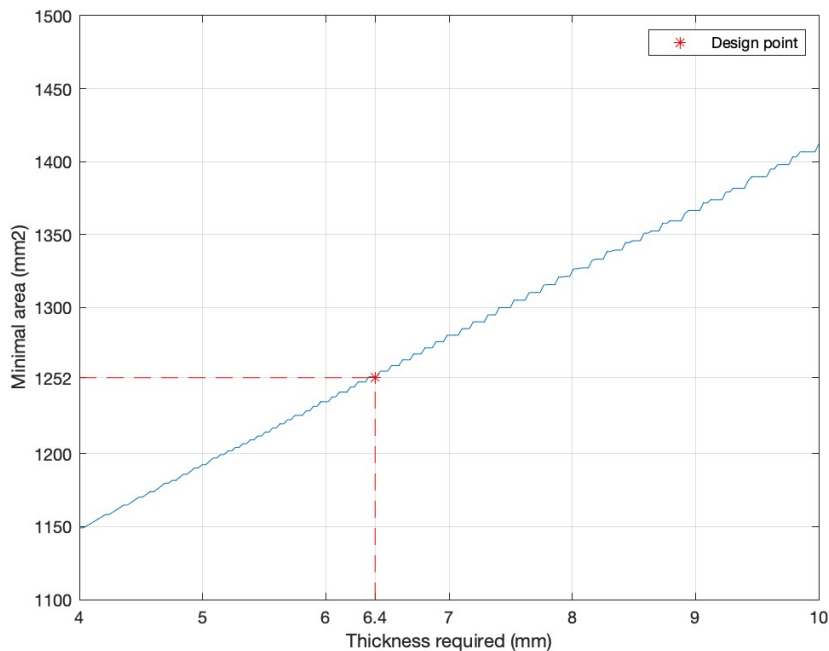


**Figure I.4:** Evolution of minimal area with required thickness for engines heavy frames.

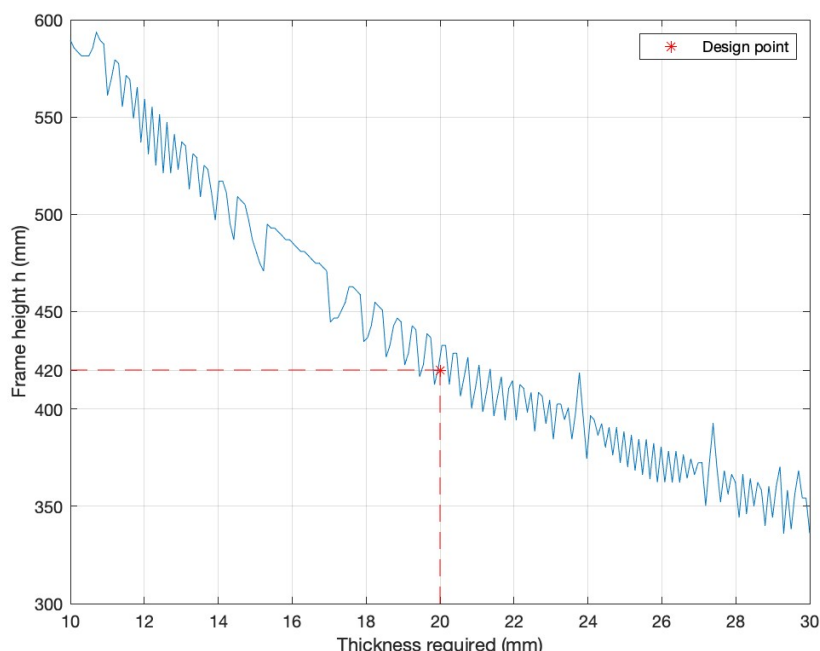


**Figure I.5:** Evolution of minimal area with required thickness for wings heavy frames.

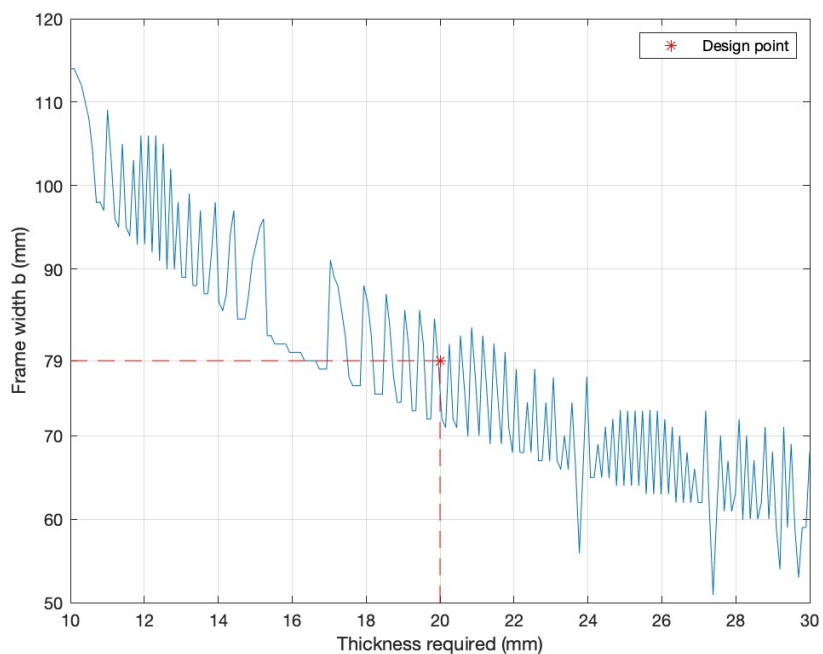


**Figure I.6:** Evolution of minimal area with required thickness for wings heavy frames.

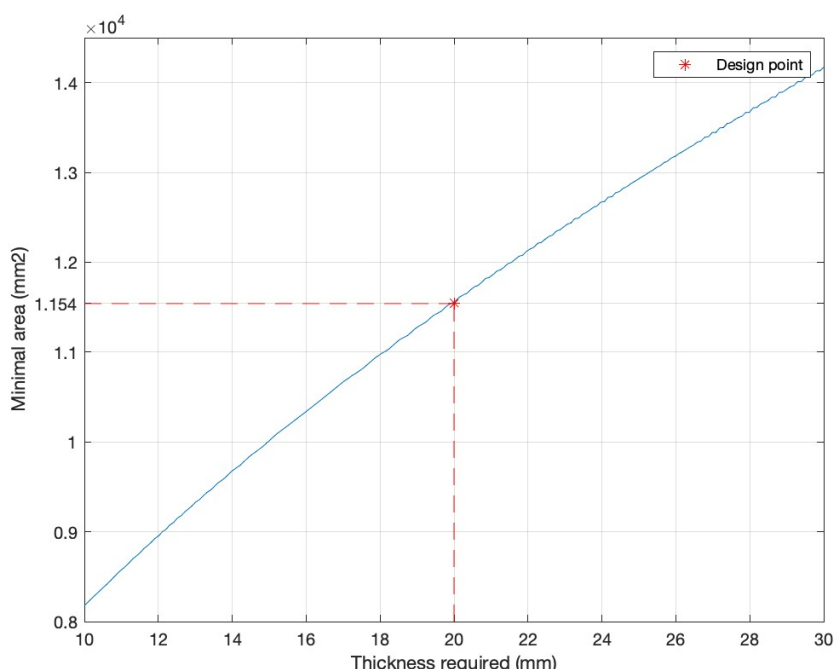


**Figure I.7:** Evolution of minimal area with required thickness for wings heavy frames.

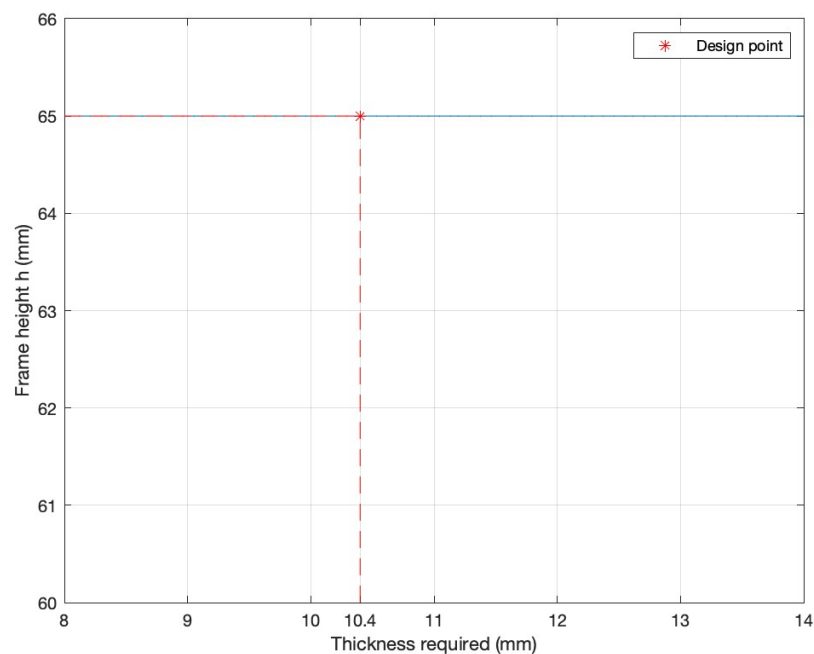


**Figure I.8:** Evolution of minimal area with required thickness for tail heavy frames.

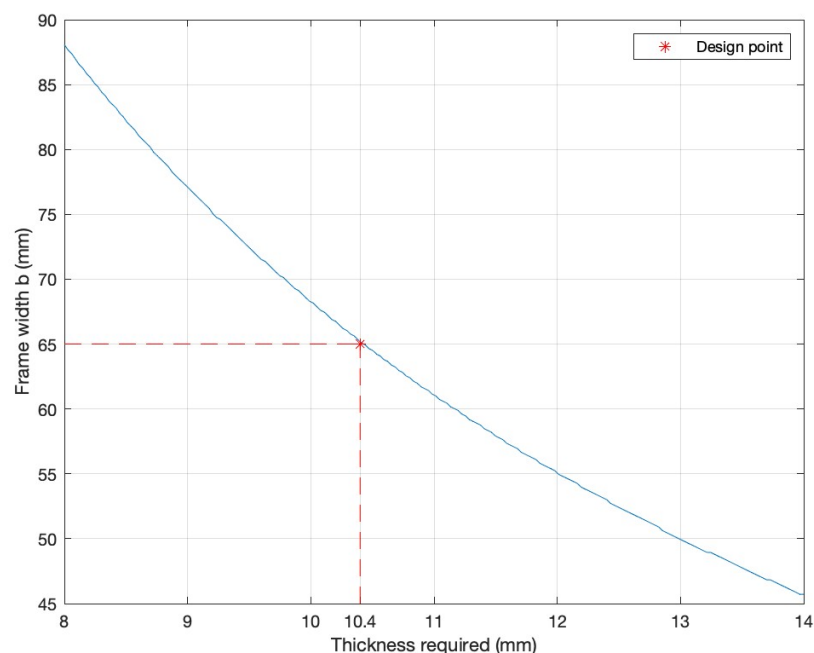


**Figure I.9:** Evolution of minimal area with required thickness for tail heavy frames.

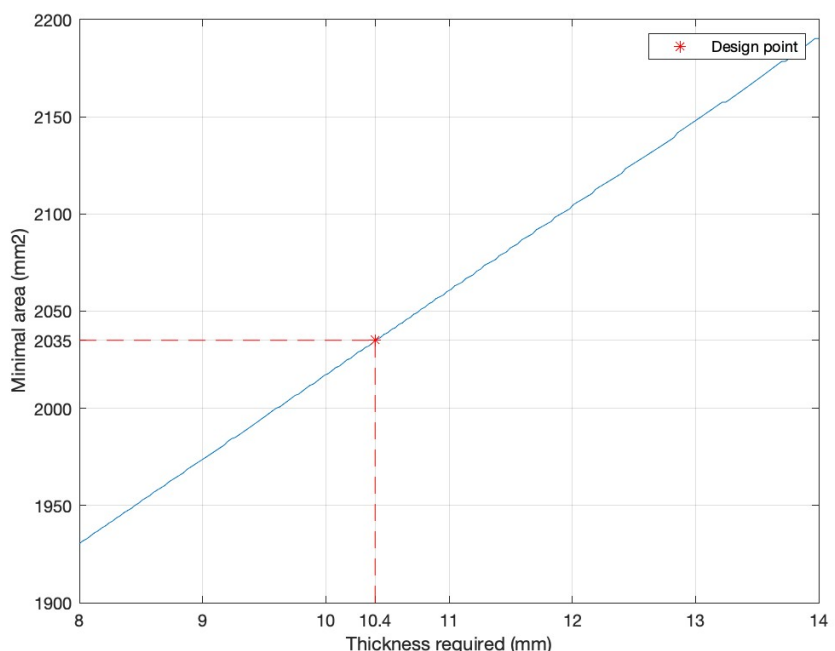


**Figure I.10:** Evolution of minimal area with required thickness for tail heavy frames.

## Appendix J

# Engine Mounts + Sizing Forces

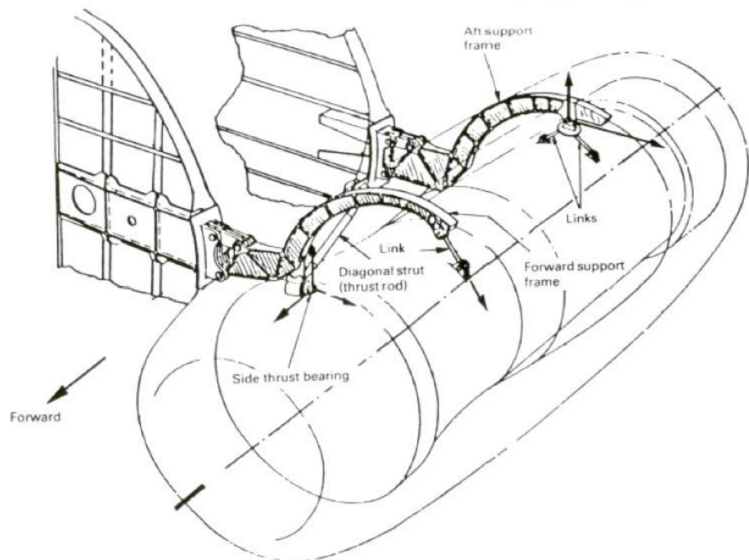


**Figure J.1:** Diagram of the planned engine mounting for a fuselage mounted engine. [32]

<b>Condition</b>	<b>Ultimate load factors (<math>n</math>)</b>
Vertical	6.5
	$6.5 + 1.5 T(C)$
	-3.5
	$-3.5 + T(C)$
Thrust	$3.0 T(\max) + 3.0$ vertical
	$3.0 T(\max) + 1.5$ vertical
	$3.0 T(R)$
Side	$3.0 T(R) + 3.0$ vertical
	$\pm 3.0$
Gyroscope	$\pm 2.25 \text{ rad/sec yaw} + 1.5 T(C)$
	$+ 1.5$ vertical
	$\pm 2.25 \text{ rad/sec pitch} + 1.5 T(C)$
Engine seizure	$+ 3.75$ vertical
	Torque equivalent to stopping mass in approximately 0.60 sec
Where:	$T(\max)$ = maximum take-off thrust at sea level
	$T(C)$ = cruise thrust (maximum or minimum, whichever is critical)
	$T(R)$ = reverse thrust

Figure J.2: Engine mount sizing forces during regular operation

- (i) Upward, 3.0g
- (ii) Forward, 9.0g
- (iii) Sideward, 3.0g on the airframe and 4.0g on the seats and their attachments
- (iv) Downward, 6.0g
- (v) Rearward, 1.5g (See AMC 25.561 (b) (3).)

Figure J.3: Engine mount sizing forces during emergency landing

## Appendix K

### Composite K Graphs

From the general fourth-order equation for the shear buckling of orthotropic panels the buckling load coefficient may be expressed as

$$k_s = \frac{b^2 N_{xy}}{\pi^2 \sqrt[4]{D_{11} D_{22}^3}}$$

This coefficient is a function of only two variables

$$\Theta = \frac{\sqrt{D_{11} D_{22}}}{D_3}$$

where

$$B = \frac{b}{a} \sqrt[4]{\frac{D_{11}}{D_{22}}}$$

and

$$D_3 = D_{12} + 2D_{66}$$

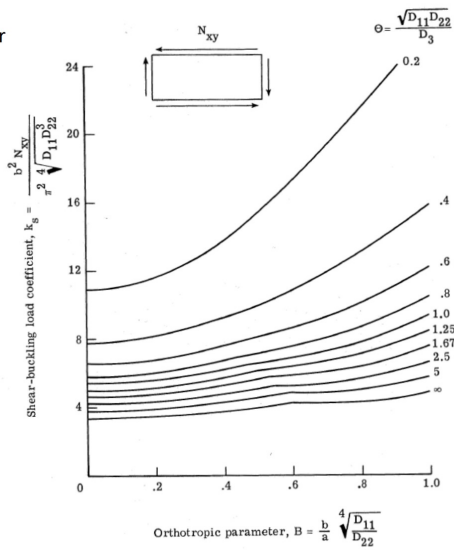


Figure K.1: Composite K Graph

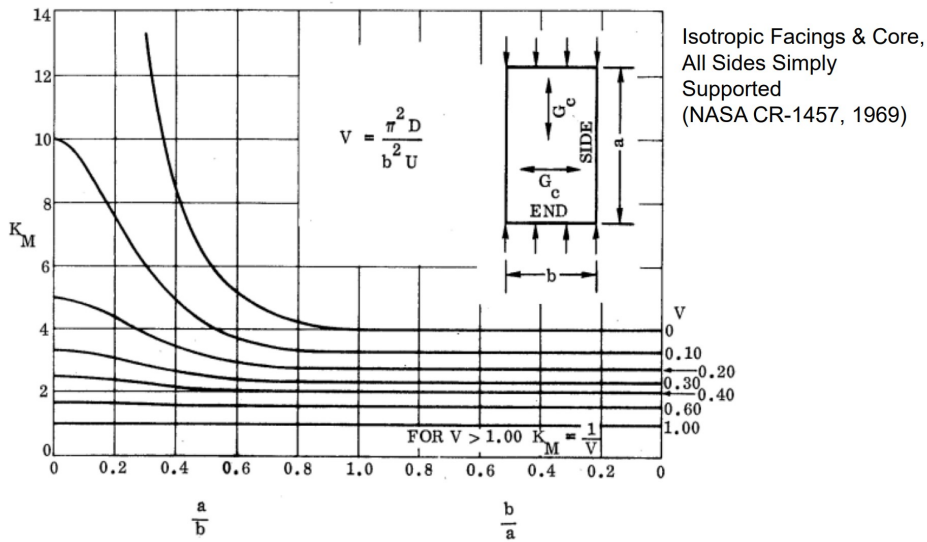


Figure K.2: Composite K Graph

## Appendix L

# Secondary Structures K Graphs

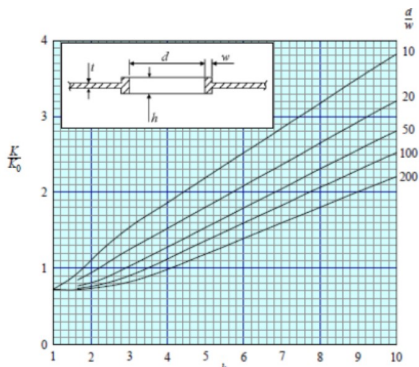


FIGURE 1  $\frac{d}{b} = \frac{1}{4}$

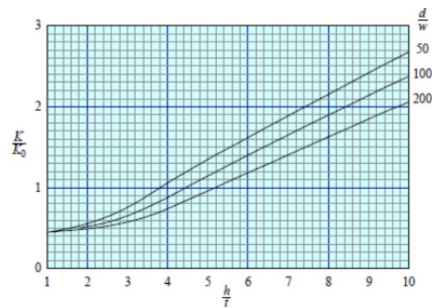


FIGURE 2  $\frac{d}{b} = \frac{1}{2}$

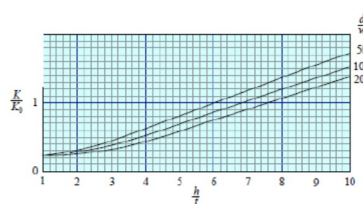
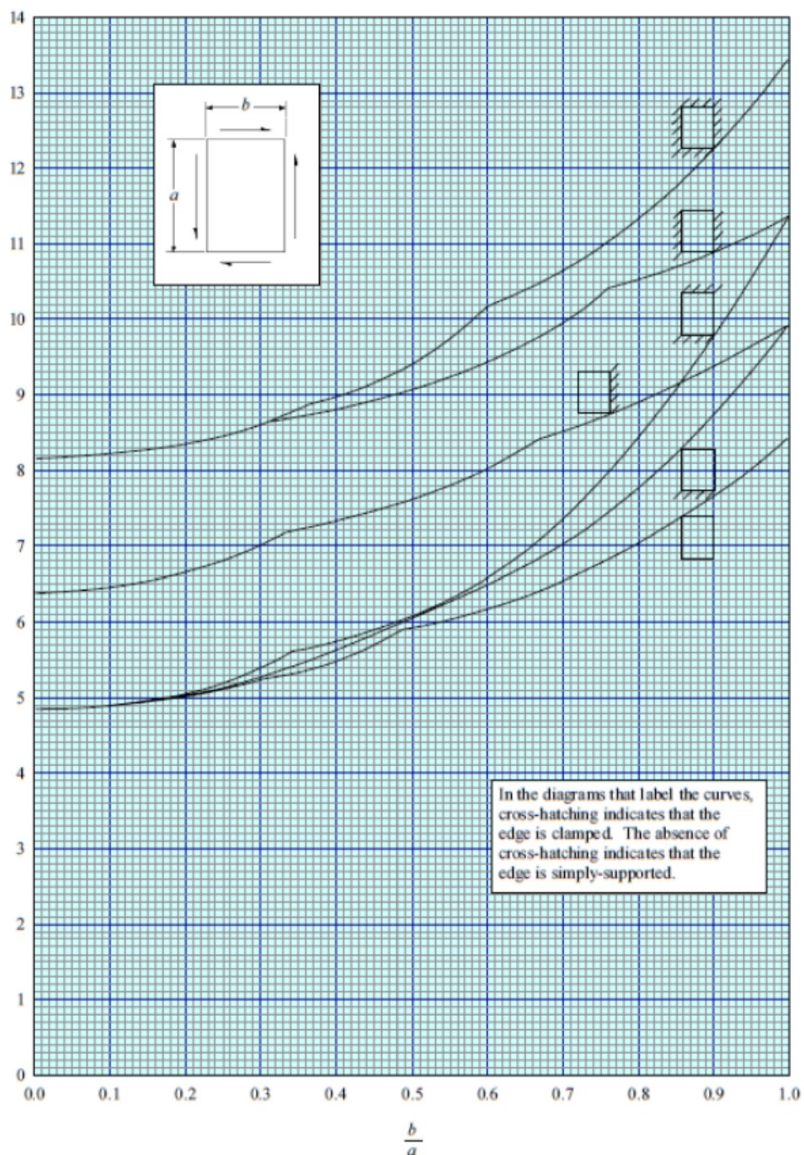


FIGURE 3  $\frac{d}{b} = \frac{3}{4}$

Figure L.1: Structure K graph



**Figure L.2:** Structure K Graph

## Appendix M

# Secondary Structures

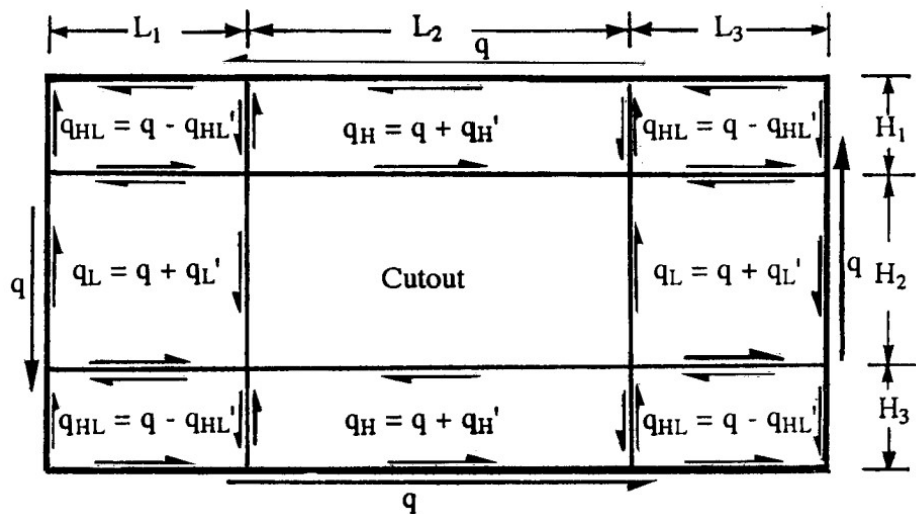


Figure M.1: Diagram showing shear flow in panels surrounding supported cutout

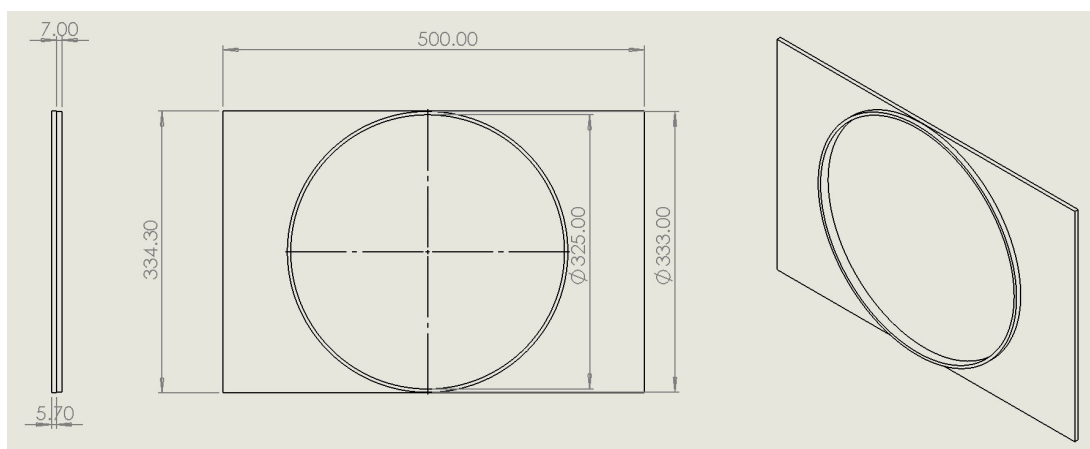


Figure M.2: Dimensions of one window panel and its required doubler

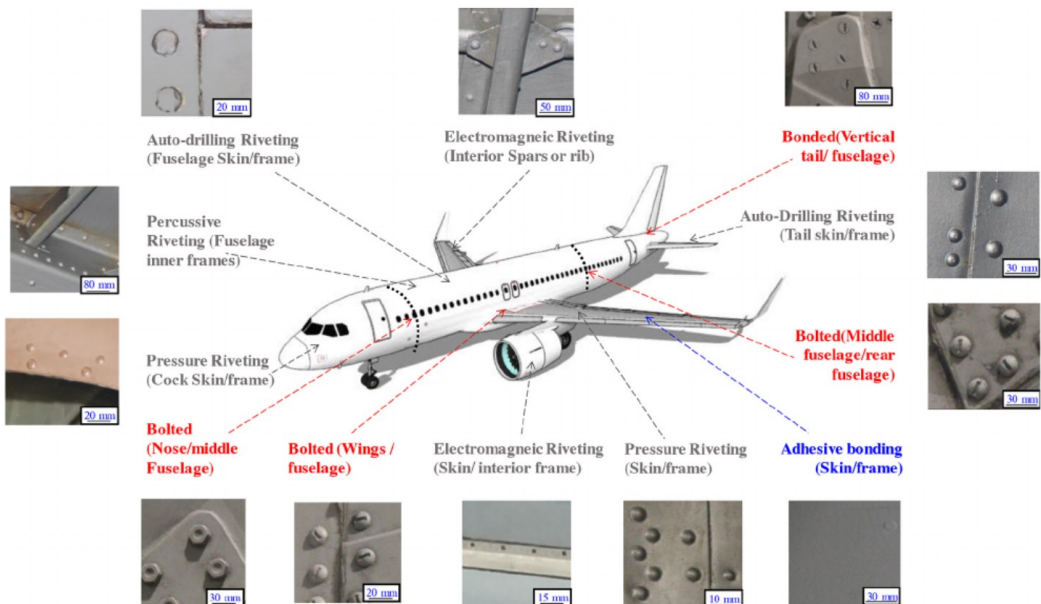


Figure M.3: Diagram showing most common aeroplane joints and fittings alternatives[14]

## Appendix N

### Skin Layup

1	2	3	4	5	6	7	8
90	45	-45	0	0	-45	45	90

Figure N.1: Skin Layup

## Appendix O

### Spar Ply Numbers along span

Front Spar	Span	0-0.12	0.12-0.36	0.36-1.20	1.20-2.51	2.51-5.98		
n0		2	2	2	2	2		
n90		2	2	2	2	2		
n45		10	8	6	4	2		
n-45		10	8	6	4	2		
nTotal		24	20	16	12	8		

Rear Spar	Span	0-0.12	0.12-0.24	0.24-0.48	0.48-0.84	0.84-1.55	1.55-3.11	3.11-5.98
n0		4	2	2	2	2	2	2
n90		4	2	2	2	2	2	2
n45		12	12	10	8	6	4	2
n-45		12	12	10	8	6	4	2
nTotal		32	28	24	20	16	12	8.00

Figure O.1: How number of plies changes along spar semi span